

Dissertation

submitted to the

Combined Faculties for the Natural Sciences and for Mathematics

of the Ruperto-Carola University of Heidelberg, Germany

for the degree of

Doctor of Natural Sciences

Put forward by

Stefan Dorsch, M.Sc.

Born in Würzburg, Germany

Oral examination: 05.02.2020

Measurement of isocenter accuracy and image distortion in magnetic resonance- guided radiotherapy

Referees:

Prof. Dr. Joao Seco

Prof. Dr. Christian Karger

Measurement of isocenter accuracy and image distortion in magnetic resonance-guided radiotherapy

Magnetic resonance (MR)-guided radiotherapy involves complex irradiation- and imaging devices (MR-Linacs), as well as complex treatment procedures. To assure accurate patient treatments, both have to be tested for proper functioning. Here, new methods to simultaneously measure the isocenter alignment accuracy and the geometric image distortions of clinical MR-Linacs were developed. A new phantom was designed, which includes a polymer dosimetry gel-container to visualize the beams from a star shot and to identify the radiation isocenter position in MR as well as a regular grid used to visualize the MR image distortions in 3D. It was found that the gel can be evaluated immediately after irradiation with a geometric accuracy comparable to that of radiochromic films. The method was applied on a clinical 0.35 T MR-Linac and the isocenter alignment accuracy in 3D was found to be (0.8 ± 0.9) mm. The spatial image distortions after machine-specific correction were (0.60 ± 0.28) mm and 99.82% of the 1330 evaluated control points within a 140 mm sphere had deviations below 1.5 mm. Finally, a 3D printing materials and printing technique, compatible with the polymer dosimetry gel, was identified for future designs of anthropomorphic phantoms to be used in end-to-end tests in MR-guided radiotherapy.

The thesis is presented in cumulative format and comprises four peer-reviewed publications.

Messung von Isozentrumsgenauigkeit und Bildverzerrung in der magnetresonanzengeführten Strahlentherapie

Die Magnetresonanz (MR)-geführte Strahlentherapie umfasst komplexe Bestrahlungs- und Bildgebungsgeräte (MR-Linacs) sowie komplexe Behandlungsverfahren. Um eine genaue Patientenbehandlung zu gewährleisten, müssen beide auf ihre einwandfreie Funktion getestet werden. In dieser Arbeit wurden neue Methoden zur simultanen Messung der Isozentrumsübereinstimmung und der geometrischen Bildverzerrungen von klinischen MR-Linacs entwickelt. Ein neues Phantom wurde entwickelt, das einen Polymer-Dosimetrie-Gel-Container zur Visualisierung der Strahlen aus einem Sternschuss zur Identifizierung des Strahlungsisozentrums im MR sowie ein reguläres Gitter zur Visualisierung der MRT-Bildverzerrungen in 3D beinhaltet. Es wurde festgestellt, dass das Gel unmittelbar nach der Bestrahlung mit einer geometrischen Genauigkeit ausgewertet werden kann, die mit der von radiochromen Filmen vergleichbar ist. Die Methode wurde an einen klinischen 0,35 T MR-Linac angewendet und die Isozentrumsübereinstimmung in 3D wurde zu $(0,8 \pm 0,9)$ mm ermittelt. Die räumlichen Bildverzerrungen nach maschinenspezifischer Korrektur betragen $(0,60 \pm 0,28)$ mm und 99,82% der 1330 ausgewerteten Kontrollpunkte innerhalb einer 140 mm Kugel hatten Abweichungen unter 1,5 mm. Abschließend wurde ein 3D-Druckmaterial und eine Drucktechnik identifiziert, die mit dem Polymer-Dosimetriegel kompatibel ist, um anthropomorphe Phantome zu entwickeln, die zukünftig in End-to-End-Tests in der MR-geführten Strahlentherapie verwendet werden sollen.

Die vorliegende Doktorarbeit wurde kumulativ angefertigt und umfasst vier von Experten begutachtete Veröffentlichungen

Contents

1	Introduction	1
1.1	Image-guided adaptive Radiotherapy	2
1.1.1	Conventional Imaging	3
1.1.2	Magnetic Resonance Imaging	4
1.1.3	Magnetic Resonance guided Radiotherapy	9
1.2	Dose deposition in magnetic fields	10
1.2.1	Point-like Dosimetry	10
1.2.2	2D and 3D Dosimetry	11
1.3	Quality assurance.....	11
1.3.1	Irradiation isocenter	12
1.3.2	Isocenter alignment at MR-Linacs.....	12
1.3.3	Geometric MR Image Distortion	13
1.3.4	Workflow verification	14
1.4	Aim of the thesis.....	14
2	Publications	15
2.1	Thematic overview.....	16
2.1.1	Irradiation-related accuracy.....	16
2.1.2	Imaging-related accuracy	17
2.1.3	Irradiation and Imaging alignment.....	17
2.1.4	Clinical validation at the MR-Linac.....	17
2.1.5	Development of phantoms for workflow verification.....	18
2.2	Publication I	19
2.3	Publication II.....	31
2.4	Publication III	39
2.5	Publication IV.....	53
3	Discussion.....	63
3.1	Machine-related geometric accuracy.....	63
3.1.1	Irradiation-related accuracy.....	63
3.1.2	Imaging-related uncertainties.....	65

3.1.3	Irradiation & Imaging alignment	66
3.1.4	Clinical validation at MR-Linac	68
3.2	Development of phantoms for workflow validation	69
4	Conclusion.....	71
	Appendix.....	73
A.1.	Fabrication instructions for the PAGAT dosimetry gel	73
	Bibliography.....	79
	Acknowledgments.....	95

List of abbreviations

<i>bSSFP</i>	<i>balanced steady-state-free-precession</i>
<i>CBCT</i>	<i>cone-beam CT</i>
<i>CT</i>	<i>computed tomography</i>
<i>CTV</i>	<i>clinical target volume</i>
<i>EPID</i>	<i>electronic portal imaging device</i>
<i>ERE</i>	<i>electron return effect</i>
<i>FID</i>	<i>free-induction decay</i>
<i>GRE</i>	<i>gradient echo</i>
<i>GTV</i>	<i>gross target volume</i>
<i>HU</i>	<i>Hounsfield units</i>
<i>IC</i>	<i>isocircle</i>
<i>IgART</i>	<i>image-guided adaptive radiotherapy</i>
<i>IgRT</i>	<i>image-guided radiotherapy</i>
<i>IMRT</i>	<i>intensity-modulated radiation therapy</i>
<i>ITV</i>	<i>internal target volume</i>
<i>Linac</i>	<i>linear accelerator</i>
MLC	<i>multi leaf collimator</i>
<i>MRgRT</i>	<i>magnetic resonance-guided radiotherapy</i>
<i>MRI</i>	<i>magnetic resonance imaging</i>
<i>MSE</i>	<i>multi spin-echo</i>
<i>NSA</i>	<i>number of signal averages</i>
<i>NTCP</i>	<i>normal tissue complication probability</i>
<i>OAR</i>	<i>organ at risks</i>
<i>PAGAT</i>	<i>polyacrylamide gelatin gel fabricated at atmospheric conditions</i>
<i>PD</i>	<i>proton density</i>
<i>PET</i>	<i>positron-emission-tomography</i>
<i>PG</i>	<i>polymer gel</i>
<i>PMMA</i>	<i>polymethylmethacrylat</i>
<i>PTV</i>	<i>planning target volume</i>
<i>QA</i>	<i>quality assurance</i>
<i>RF</i>	<i>radiofrequency</i>
<i>RT</i>	<i>radiotherapy</i>
<i>SE</i>	<i>spin echo</i>
<i>SNR</i>	<i>signal-to-noise ratio</i>
<i>SPECT</i>	<i>single photon emission tomography</i>
<i>TCP</i>	<i>tumor control probability</i>
<i>TE</i>	<i>echo time</i>
<i>TR</i>	<i>repetition time</i>
<i>TSE</i>	<i>turbo spin-echo</i>

1 Introduction

Cancer is one of the leading causes of death in industrialized countries around the world [1,2]. In Germany alone, 227,600 people died of cancer in 2017 [3]. Cancer is generally described as the uncontrolled proliferation of malignant tissue cells potentially accompanied by invasion into adjacent healthy tissue or even by the formation of distant metastasis in other body parts. Standard cancer treatments include surgery, radiation therapy and chemotherapy, which follow either a curative or palliative approach.

The aim of radiotherapy (RT) is to inactivate cancer cells by exposing them to a high dose (absorbed energy per mass, $D = \frac{dE}{dm}$ [Gy]) of ionizing radiation while sparing the surrounding normal tissue. A major advantage of external beam radiotherapy is its non-invasiveness. Although treatment with protons and heavy ions [4–7] (mostly carbon ions) has become increasingly popular in recent years, high energy photons produced from MeV electrons in medical linear accelerators (Linac), still make up the vast majority of treatments [4,8]. Considering the energy of the photons in the MV-range, the interaction with matter is dominated by Compton scattering, leading to a transfer of large fractions of the photon energy to secondary electrons. This leads to an ionization of atoms and molecules and subsequently to Coulomb interaction of the secondary electrons with other charged particles in the tissue resulting in a local dose deposition. This leads to further ionization processes, which may affect the structural integrity of important biomolecules like nucleic acids and proteins along its path [9]. Most importantly, this may lead to DNA damage (single or double strand breaks) in tissue-composing cells leading to cellular death [10,11].

Usually, high doses are required to successfully control the tumor, however, due to the physical interaction mechanisms of photons with matter, the normal tissue and organs at risk (OAR) along the beam path may also be exposed to radiation resulting in tissue damage, making the normal tissue a limiting factor for a successful treatment. However, healthy cells tend to have repair mechanisms for radiation damage, which are often compromised in tumor cells [12]. Using a fractionated irradiation scheme, which splits the total dose over a longer time period (typically 30 fractions delivered over six weeks), the healthy tissue is given the possibility to repair part of the radiation damage in the break between the individual treatments, which leads to an increased radiation tolerance. As a quantitative measure, so-called dose-response curves for the end-points (local) tumor control probability (TCP) and normal tissue complication probability (NTCP) are used (Figure 1). The location and slope of dose-response curves depend on biological properties of the tissue but also on physical parameters of the radiation treatment plan. If the area between tumor control and the side effect curves (the so-called “*therapeutic window*”) is increased, the probability for tumor control without complication also gets higher. This “opening” of the therapeutic window may be realized by shifting the complication curve to higher doses, e.g. by optimizing the irradiation plan parameters to avoid irradiation of radiosensitive OARs and to reduce the irradiated normal tissue volume. Estimations of tolerance doses of normal tissue can be found in literature [13–15], recommended tumor doses are defined in clinical protocols and limited by the maximum acceptable risk of side effects.

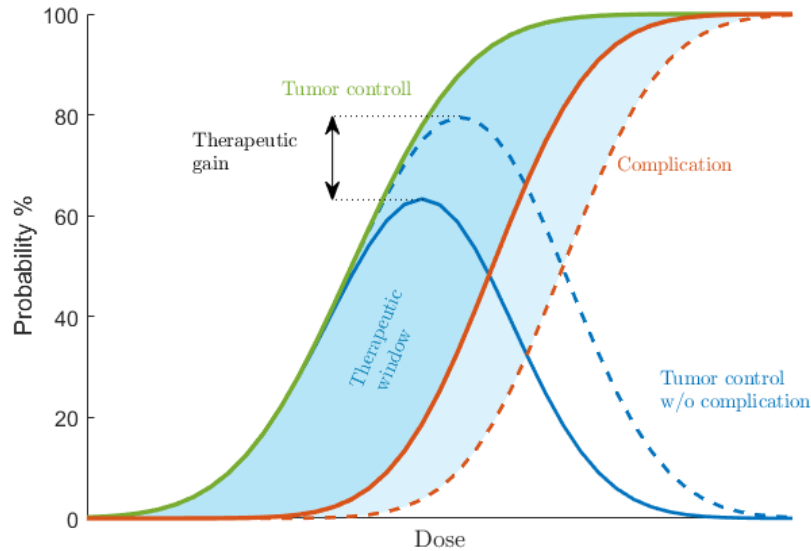


Figure 1. Dose-response curves describing the probability for tumor control (TCP) and normal tissue complication (NTCP). From these curves, the probability of tumor control without complications can be calculated. A shift of the NTCP-curve relative to the tumor control curve towards higher dose leads to a therapeutic gain, which may be used to increase the effectiveness in the tumor or to reduce the complication risk.

1.1 Image-guided adaptive Radiotherapy

The general goal of radiation therapy is to maximize the dose in the target volume while minimizing the exposure of the surrounding healthy tissue. This can be reached by i) choosing a suitable irradiation type, e.g. photons, protons or heavy ions (beam quality), ii) tailoring the beam laterally to the target volume and using multiple intersecting beams from different directions (dose conformation) and iii) fractionation. In addition, the radiation fluence may be modulated over the beam cross section to reduce the dose in OARs from one beam direction while the missing dose is then delivered by another beam. This technique is called intensity-modulated radiation therapy (IMRT) [16–19] and leads to additional sparing of normal tissues.

Besides accurate technical delivery of the radiation dose, the knowledge about the exact tumor position plays a crucial role for effective cancer treatments. Several imaging modalities can be used to localize the tumor within the patient, ideally offering a high spatial 3D-resolution and contrast between tumor and the adjacent normal tissues. Computed Tomography (CT) is the most common technique used today, as it provides information about electron density of the tissue required for the dose calculation. In addition, Magnetic Resonance Imaging (MRI) with its superior soft tissue contrast is also becoming increasingly important. The images are typically acquired prior to irradiation and are used to delineate the macroscopic part of the tumor, the so-called gross target volume (GTV). Subclinical, invisible microscopic extensions of the tumor can be accounted for by expanding the GTV to the clinical target volume (CTV) [20]. To compensate for additional geometric uncertainties resulting from internal physiological movement (intra- and interfractional motion) leading to variations in size, shape and position of the CTV, the internal target volume (ITV) is introduced. Finally, uncertainties arising from position errors of the patient and the radiation

delivery require the introduction of additional safety margins, leading to the planning target volume (PTV). The delineated volumes, including the OARs, are then used to optimize the treatment parameters to maximize the dose within the tumor and minimize the dose in the surrounding healthy tissues. Besides CT and MRI, Positron-Emission-Tomography (PET), Single Photon Emission Tomography (SPECT) and ultra sound may be used in addition to support tumor localization and differentiation from normal tissue as well as to provide additional functional information about the tissue.

Depending on the magnitude of inter- and intrafractional organ motion, the size of the ITV may increase the radiation exposure of healthy tissue significantly, leading to an increased risk of side effects [21]. By improving the accuracy of the tumor localization through image-guided radiotherapy (IgRT) prior and during the treatment fractions, inter- and intrafractional motion may be compensated: In the presence of interfractional organ motion, the treatment plan can be adapted to the given daily anatomy which allows safety margins and the size of the ITV to be reduced [22]. To account for intrafractional organ motion a gated irradiation may be performed [23–25]. Here the tumor is only irradiated, if it is located within a predefined window. The radiation exposure of the surrounding healthy tissues can be reduced by combining IgRT with an adaption of the treatment plan to the actual anatomical configuration. This approach is termed image-guided adaptive radiotherapy (IgART).

1.1.1 Conventional Imaging

Computed Tomography

To obtain information about the anatomical structure, the state-of-the-art is to acquire a CT before the actual treatment. In principle, CT uses a rotating X-ray tube to create absorption profiles of the object from many different directions to reconstruct 3D-images of the patient [26]. Even though CT usually uses X-rays with lower energy (usually 80 kV – 140 kV) than Linacs used for radiotherapy (6 MV - 18 MV), they share the same underlying physical principle of radiation attenuation. The attenuation of the intensity I can be expressed with the *Beer-Lambert law*:

$$I = I_0 \cdot e^{-\int \mu(x) dx} \quad (1.1)$$

Here, I_0 represents the radiation intensity emitted from the source and $\mu(x)$ the attenuation coefficient which varies within the scanned object. The resulting CT attenuation coefficients are expressed in Hounsfield units (HU) and can be converted in electron densities by means of a CT specific lookup table that is used for dose calculation during the treatment planning process. Although superior in terms of acquisition time and geometric accuracy, CT scans represent a further radiation exposure for the patient and provide only poor soft-tissue contrast. The equivalent dose expressed in units of mSv, indicating the associated radiation risk, may reach up to 20 mSv for whole body scans [27,28].

On-board imaging

The accurate positioning of the patient required for precise targeting of the tumor volume over the entire treatment period are decisive for accurate dose delivery and thus for the success of the

treatment. Therefore, nearly all conventional therapy devices nowadays are equipped with imaging devices to check patient setup and the location of the tumor at the irradiation device prior to each treatment session.

Using a flat panel detector mounted directly on the Linac, the MV treatment beam can be used to acquire MV transmission images. However, this so-called portal imaging has a very poor soft tissue contrast due to the high photon energy [29,30]. Therefore, many modern Linacs are additionally equipped with an on-board kV-imaging system, with a kV-source mounted perpendicular to the treatment beam and a second flat panel detector on the opposite side [31]. By this, either planar images (2D) or even CT-like (3D) images can be generated, when the gantry is rotating around the patient. As this setup uses a cone beam instead of a fan beam geometry, like diagnostic CT devices, this technique is known as (kV) cone-beam CT (CBCT). Due to the lower energy of the kV photons, the soft tissue contrast is higher than for MV-CBCTs, however, the general image quality is significantly lower than in diagnostic CTs due to the larger impact of scattered radiation [29,31]. Since bony structures can be easily recognized, CBCTs are well suited to match these structures with the pre-treatment reference images to derive setup corrections. Since bony structures may not always be representative for the tumor position, additional imaging techniques with better soft tissue contrast can significantly improve tumor localization.

1.1.2 *Magnetic Resonance Imaging*

Compared to CT, MRI shows a superior soft tissue contrast, which facilitates the differentiation between tumor and OAR and, accordingly, the delineation of the target volume [32,33]. Furthermore, MRI uses non-ionizing radiation for image acquisition, and therefore does not represent an additional exposure for the patient. MRI utilizes strong magnetic fields, magnetic field gradients, and radio frequency waves to manipulate the orientation of the magnetic moment (and hence the spins) of the protons within the body to generate images. The following section will give a short introduction to the basic principles of MRI. For a more detailed explanation, the reader is referred to the relevant literature [12,32,34,35].

Basic Principle

Nuclei with an odd number of nucleons have a spin and a magnetic moment different from zero, which means that they have a magnetic moment. This holds for several nuclei (e.g. ^1H , ^3He , ^{19}F and ^{23}Na) and of these, the hydrogen atom (^1H) is the most frequently used for MRI due to its high natural abundance in human tissue (particularly leading to a significantly larger MRI signal than other nuclei). Therefore, the following description focusses on hydrogen nuclei.

Without external magnetic field, the nuclear spins are in thermal equilibrium and thus randomly distributed. In the presence of an external static magnetic field B_0 , however, the spins align parallel or anti-parallel to B_0 , usually defined as z-direction, due to their connection to the magnetic moment. As the orientation parallel to the magnetic field is energetically slightly favored according to the Boltzmann statistics, a macroscopic net magnetization M_z in the order of ppm is generated [32]. The individual spins precess around the direction of the B_0 -field with the Larmor frequency ω_0 given by

$$\omega_0 = \gamma B_0 \quad (1.2)$$

with the gyromagnetic ratio $\gamma = 42.58 \text{ MHz/T}$, which is specific for protons. Under this condition, the net magnetization in z-direction is static. By applying a radiofrequency (RF) pulse B_1 perpendicular to B_0 with a frequency at the Larmor frequency ω_0 , the orientation of the net magnetization M_z is rotated from the z-direction (longitudinal) towards the xy-plane (transversal). This effect is known as magnetic resonance and the flip angle α can be calculated by the duration of the RF pulse t_p as follows:

$$\alpha = \gamma B_1 t_p \quad (1.3)$$

As a result, the net magnetization starts precessing around the magnetic field B_0 inducing a oscillating electric voltage in a receiver coil according to *Faraday's Law* [36]. The amplitude of this voltage is proportional to the transverse magnetization.

Relaxation process

When the RF-pulse is switched off, the magnetization immediately starts propagating back towards its equilibrium state leading to an exponential decay of the transverse magnetization, which is termed *free-induction decay* (FID). This relaxation process is caused by interactions of the spins with the molecular environment and can be divided into three processes: The spin-lattice-interaction (also called *T₁-relaxation*) describes the longitudinal transition of the magnetization towards its equilibrium state, caused by energy dissipation of the spins to their environment. The relaxation process of the full amplitude in z-direction $M_{z,0}$ can be described with the tissue-specific relaxation time T_1 :

$$M_z(t) = M_{z,0} (1 - e^{-t/T_1}) \quad (1.4)$$

The spin-spin-interaction (or *T₂-relaxation*) describes a dephasing process of the spins, resulting in a reduction of transverse magnetization M_{xy} . This can be described by an exponential decay and is characterized by the tissue-specific relaxation time T_2 .

$$M_{xy}(t) = M_{xy,0} e^{-t/T_2} \quad (1.5)$$

Additional dephasing of the spins due to local machine-related magnetic field inhomogeneity is described by the modified relaxation time T_2^* . The relaxation times T_1 , T_2 and T_2^* (Figure 2) depend on the chemical and physical environment in which the nucleus is located. Therefore different tissue types can be characterized by specific relaxation times leading to different tissue contrast. Proton density and material specific relaxation times are the main factors that influence the tissue contrasts.

Spatial encoding/ Image acquisition

To acquire MR-images, the following main components are required: a magnet producing a strong, constant magnetic field to align the magnetic moments in z-direction, a magnetic field gradient

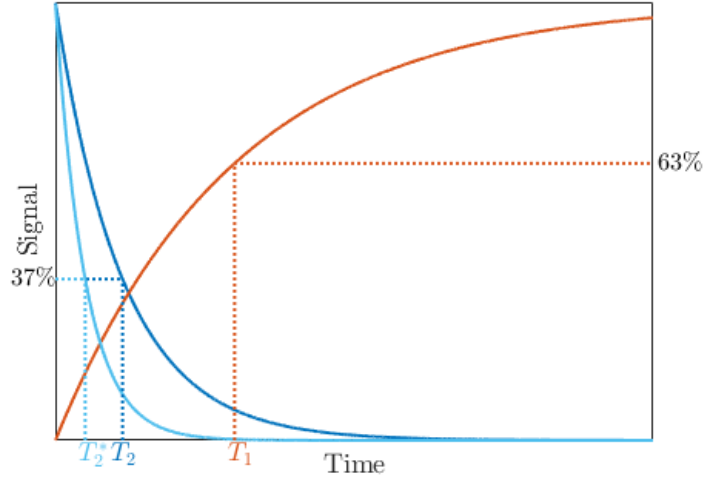


Figure 2. Characteristic signal profile of T_1 and T_2 relaxation as described with equation (1.4) and (1.5). While the T_2 and T_2^* time is determined by the time after the signal has decreased to 37% of its initial value, T_1 is defined as the time after the longitudinal magnetization has recovered to 63% of the equilibrium value.

system, which generates locally varying Larmor frequencies used to encode the spatial information and the RF system with transmitter and receiver coils which excite and detect the MR signals. To create an image, a slice selection in the transversal plane is performed using a slice selective magnetic gradient (G_{SS}). In conventional MR imaging, this allows the excitation of the spins only in this pre-defined slice. The spatial information within this slice can then be obtained by imprinting a phase- (G_{PE}) and frequency-encoding (G_{FE}) gradient. The individual signals of repeated excitations and recordings with varying phase-encoding (active during readout) are entered into a matrix (in the so-called “*k-space*” [37]) and a two-dimensional Fourier transformation allows separating the contribution of individual frequencies to the signal strength of each voxel resulting in a 2D image in real space. This procedure is then repeated with different slice selective gradients to acquire a full 3D dataset.

Spin- and Gradient-Echo sequences

While the magnetization is continuously decaying towards the equilibrium state, the resulting FID signal can be manipulated to restore parts of the signal originating from the transversal dephasing of the spins originating from field inhomogeneities to form a so-called *echo*. There are basically two different techniques to form such an echo: (i) by applying special RF pulses (leading to so-called *spin echos* (SE), see Figure 3, left) or (ii) additional de- and rephasing gradients (leading to so-called *gradient echo* (GRE), see Figure 4). The *echo time* (TE) represents the time from the center of the first RF pulse to the center of the echo. The *repetition time* (TR) describes the time interval between two consecutive RF pulses, flipping the magnetization from the longitudinal to the transverse direction.

In case of a SE-sequence, the 90° excitation pulse which rotates the longitudinal magnetization into the transversal plane is followed by a 180° refocusing pulse after half of the echo time TE as described in Figure 3. Phase differences caused by static machine-related field inhomogeneities up to this time are reversed and canceled out after TE [38]. Applying a set of n consecutive 180°

pulses leads to a generation of n echoes, each located at $n \cdot TE$. Such sequences are termed *multi spin-echo* (MSE) sequences and allow for quantitative determination of the T_2 -relaxation time by fitting an exponential function to the signal intensity of the sequence of measured n echoes [39,40]. To minimize any influence by the T_1 -related decaying process, the repetition time TR needs to be chosen sufficiently high ($TR \geq 3T_1$).

Related to the MSE sequence is the so-called *fast* or *turbo spin-echo* (TSE) sequence, which also uses several consecutive 180° pulses [41]. In contrast to a MSE, additional varying phase gradients are applied between each 180° pulse allowing for a faster k-space filling. For regular SE and MSE sequences, the phase-encoding gradient is constant during each TR interval. As a result of changing the phase-encoding gradient for each 180° -pulse, multiple phase-encoding steps (lines of k-space) can be acquired within a given repetition time. Therefore the imaging time may be reduced significantly. In general, the signal intensity of a SE sequence, determined by the proton density (PD) of the tissue and both a T_1 and T_2 factor of a voxel can be described as:

$$S = \text{PD} \underbrace{(1 - e^{-TR/T_1})}_{T_1 \text{ factor}} \underbrace{(e^{-TE/T_2})}_{T_2 \text{ factor}} \quad (1.6)$$

Depending on the parameters TR and TE, the T_1 and T_2 factor contribute differently to the contrast between neighboring tissues leading either to T_1 -weighted, T_2 -weighted images or proton density weighted images (Figure 3, right).

As the 90° RF-pulse rotates the entire longitudinal magnetization into the transversal plane, the time to the next excitation pulse (TR) has to be long enough that at least parts of the longitudinal

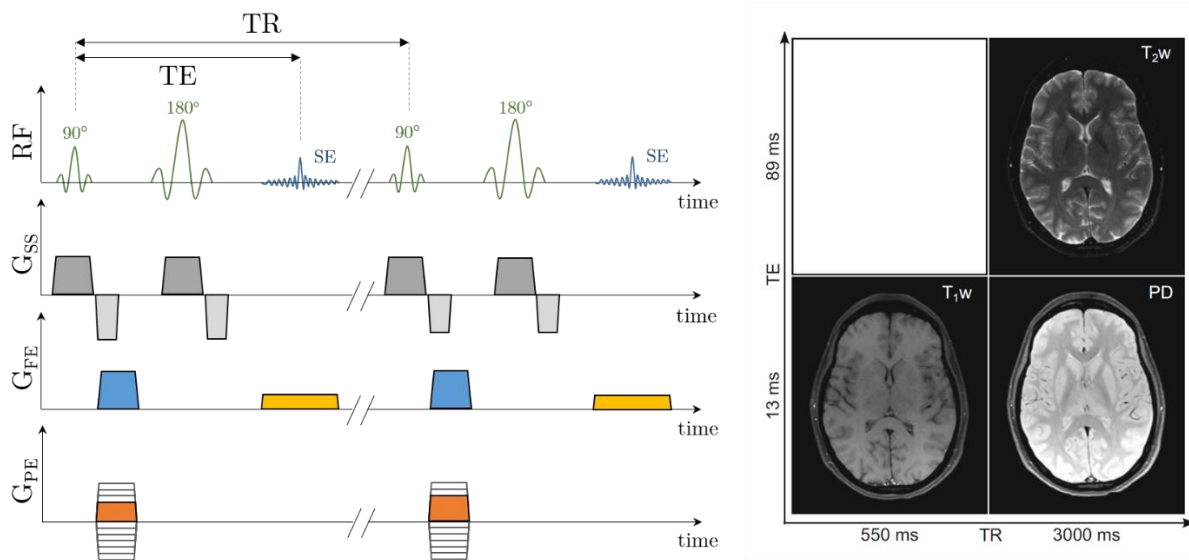


Figure 3. Left: Pulse sequence of a spin-echo sequence. The dephasing of the spins is reversed by a 180° pulse and leads to a spin echo after the time TE. The 180° rephasing pulse compensates for all machine-related field inhomogeneities and therefore the signal of the echo has a T_2 rather than T_2^* -dependence. Right: Contrast behavior of a SE sequence for different TR and TE (adapted from Schlegel et al. [12]).

1 Introduction

magnetization have recovered by T_1 -relaxation. This results in long scan times for SE sequences. As gradient echo sequences use flip angles $\alpha \leq 90^\circ$, significantly shorter scan times can therefore be achieved. The gradient echo formation in a GRE sequence is achieved by applying a dephasing gradient (Figure 4, blue) before the (rephrasing) frequency-encoding or readout gradient (yellow), often followed by a spoiler gradient that destroys the transversal magnetization. For a short TR ($< T_1$), the longitudinal magnetization does not fully recover to its equilibrium value $M_{z,0}$ before the next RF-pulse is applied, leading to a new so-called steady-state magnetization M_z^{SS} . As the 180° RF rephasing pulses that compensate the dephasing of spins due to static magnetic field inhomogeneities is missing, the contrast of gradient echo sequences is usually determined by T_2^* -relaxation. A special form of gradient echo sequences is the (*balanced*) *steady-state-free-precession* (bSSFP) sequence [42–44]. While other gradient-echo sequences only use the described steady state of longitudinal magnetization and use spoiler gradients to destroy the transverse magnetization, the bSSFP sequences also include transverse coherences to create a dynamic equilibrium: for short TR ($< T_2$), the transverse magnetization does not fully decay to zero before next RF-pulse is applied, leading to a non-zero steady-state transverse magnetization after a few pulses. Instead of destroying the remaining transverse magnetization by spoiler gradients, refocusing gradient pulses are introduced in slice-selection direction as well as in the direction of frequency and phase encoding (Reiser 2008). This leads to partial refocusing of the transverse magnetization, contributing to the signal. Therefore, a very strong image signal can be produced using very short TR, TE and a large flip angle leading to a T_1/T_2 -contrast. By resetting the phases along all axes within a TR interval, the fbSSFP sequence is particularly prone to magnetic field inhomogeneities [12].

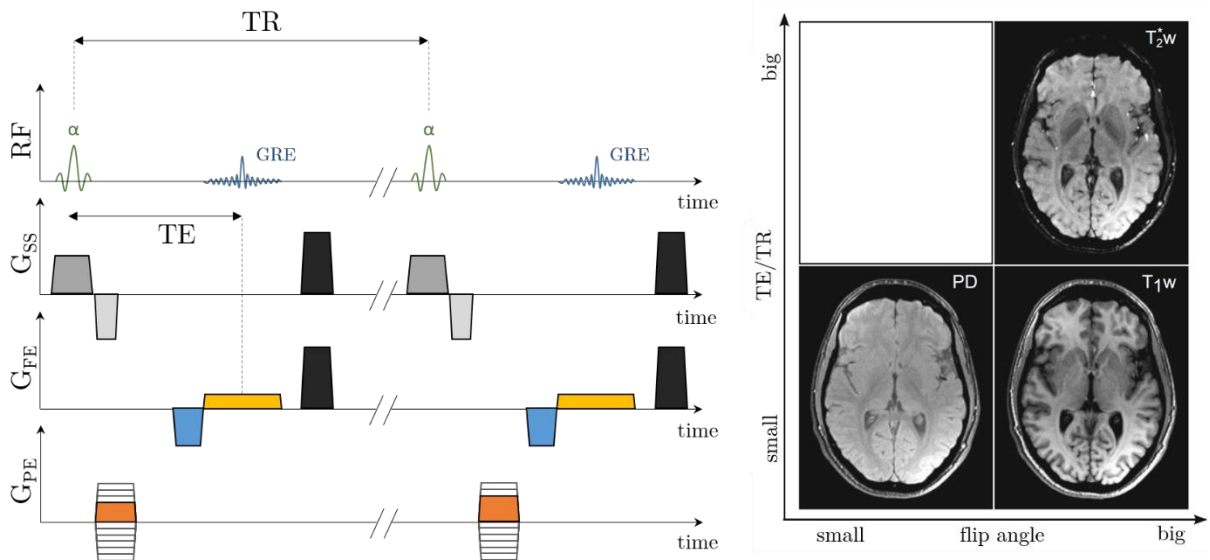


Figure 4. Left: Pulse sequence of a gradient-echo sequence. The gradient echo formation results from applying a dephasing gradient (blue) before the frequency-encoding (or readout gradient) (yellow) followed by the spoiler gradients (black). As machine-related field inhomogeneities are not compensated the image contrast is therefore only determined by T_2^* -relaxation. Right: Contrast behavior of a GRE sequence for different TE/TR-ratios and flip angle (adapted from Schlegel et al. [12]).

1.1.3 Magnetic Resonance guided Radiotherapy

The properties described above make MRI an excellent imaging modality to distinguish soft tissues. This feature is of high interest also for image-guidance in radiotherapy. Just recently, the MRI-technology has been integrated in irradiation devices leading to a new type of hybrid imaging and irradiation devices for the so-called *magnetic resonance-guided radiotherapy* (MRgRT). MRgRT can be realized by suitable shuttle systems transporting the patient between MRI scanner and the treatment couch of the Linac [45,46]. In this setting (offline-MRgRT), both devices may be located in different rooms and no or only few technical modifications are necessary. However, the transport of the patient may potentially introduce anatomical changes and organ movements during the treatment (intrafractional) are not detectable. Also MR systems mounted on rails are subject of research [47].

More challenging, is the direct integration of a linear accelerator into an MRI-device. As proper functioning of Linacs requires a magnetic field-free area, the realization of such hybrid devices is therefore technically demanding. However, different realizations of such hybrid device, so called *MR-Linacs*, have been developed and are in clinical use [48–51]. A distinction can be made between systems which have their magnetic field aligned either perpendicular [50,51] or parallel (in-line) [48,49] to the direction of the beam. The latter are still under development and not yet employed clinically. Presently, there are two commercial MR-Linac systems employing a beam perpendicular to the magnetic field. These are the 1.5 T “Unity” (Elekta AB, Stockholm, Sweden) and the 0.35 T “MRIdian” MR-Linac (ViewRay, Inc., Oakwood Village, OH, USA), which was employed in this work. The MRIdian system (Figure 5) consists of a two axially aligned superconducting 0.35 T magnets separated by a gap (double donut) forming the MRI and a 6 MV Linac mounted on a ring gantry, which is installed in this gap [52]. The Linac itself as well as the electronics is installed in a metal bucket and is shielded from the magnetic field and the RF-radiation.

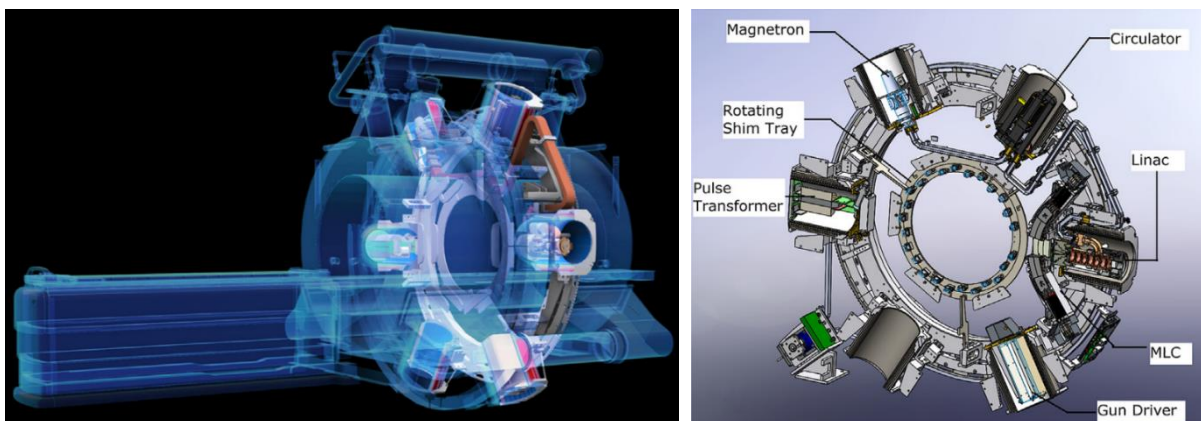


Figure 5. Schematic drawing of the ViewRay system. Left: Complete view with double donut magnet, Linac gantry and patient couch and ring gantry. Right: Detailed sketch of the ring gantry with Linac component, *multi leaf collimator* (MLC) and electronics. (Adapted from [52], Image courtesy of ViewRay Inc.)

1.2 Dose deposition in magnetic fields

In the presence of a magnetic field not only the correct functioning of the Linac is a challenging task, but also the dose distribution is affected. The uncharged photons emitted by the Linac do not interact with the magnetic field, however, due to their interaction mechanism with matter, they will produce a cascade of secondary electrons having ranges in the order of 1.5 cm [12]. The trajectory of the electrons will be affected by the magnetic field due to the *Lorentz force*. As the local dose distribution depends on the electron tracks, the dose distribution and the associated biological effect may change in presence of magnetic fields [53–58]. Accordingly, the influence of the magnetic field is most dominant for long-ranging electrons occurring especially in low-density materials.

Also the orientation of the magnetic field with respect to the direction of the photon beam plays a crucial role: While a magnetic field parallel to the beams leads to a longitudinal focusing of the radiation dose but also to an increased surface dose due to air-borne electrons [59,60], the Lorentz force is maximized when the beam is perpendicularly oriented to the beam. This is most noticeable at interfaces between tissue and air cavities, where electrons may experience a “full turn” and return to the tissue, leading to an additional dose deposition (“hot spots”) at the entrance- and missing dose (“cold-spots”) on the exit side of the cavity. The impact of this so-called *electron return effect* (ERE) [54,61–63] depends on the orientation and strength of the magnetic field. The ERE may also affect the response of ionization chambers used for dose measurements (see 1.2.1). As the dose distribution is altered by the magnetic field, the evaluation of the absolute dose as well as the relative dose distribution in 3D is of special importance in MRgRT. For this, different point-like, two- and three-dimensional measurement techniques are available.

1.2.1 Point-like Dosimetry

For point-like dose measurements, air-filled calibrated ionization chambers are most frequently used [12,64]. They have the great advantage of being traceable to primary standards realized by calorimetric measurements in national primary standard laboratories [65,66]. As the response of air-filled ionization chambers may be altered in the presence of magnetic fields [67], an additional correction factor is required. For reference dosimetry, a number of investigations have been performed [67–70] and as a result these factors are quite well-known. Generally, the size of the correction decreases with decreasing volume of the ionization chamber. Under non-reference conditions, especially for small fields, these investigations are ongoing [71]. Besides absolute dosimetry, ionization chambers as well as other point-like detectors such as semiconductor diodes or diamond detectors may be used for measurements of relative dose profiles when employed in a motorized water phantom.

While ionization chambers allow for accurate dose measurements, the general disadvantage is that the information on the spatial dose distributions is very sparse. Alternatively, arrays (1D or 2D) of individual ionization chambers may be used. A general limitation is the relatively poor spatial resolution, which complicated dose measurements in steep dose gradients.

1.2.2 2D and 3D Dosimetry

Besides 2D arrays of ionization chambers, radiochromic films may be used to measure dose distributions in 2D. These day-light insensitive films consist of an active layer sandwiched embedded in layers of polyester. The active layer consists of a marker dye and incorporates the lithium salt of pentacosanoic acid (LiPAD) as active component which polymerizes when exposed to ionizing radiation changing the net optical density of the film [72–75]. After irradiation, the film is typically scanned with a standard flatbed scanner to quantify the optical density. To perform absolute film dosimetry, a calibration for each batch of films against known doses (measured e.g. by ionization chambers) has to be performed. However, this process requires a highly standardized evaluation procedure, which is the reason why film dosimetry is mostly performed in a relative way. Due to their high spatial resolution, films are mostly used for characterization of radiation fields, which include steep dose gradients as well as for *quality assurance* (QA) measurements, which often includes geometrical aspects of the radiation field. This makes radiochromic films a gold standard for many QA-applications in clinical practice.

For dosimetry in radiotherapy, it is important to get information of the full 3D-dose distribution. With films, this can only be obtained by using stacks of films, which is very cumbersome. As an alternative, radiochromic plastics (e.g. PRESAGE® [76–78]) or *polymer gel* (PG) [79–86]) dosimeters may be used. Radiochromic plastics show optical radiation-induced density changes similar to films, which can be read-out by optical-CT scanners. Polymer gels consist of radiation sensitive monomers embedded in a gelatin matrix and are thus water-equivalent [80]. In the PG, the radiation-induced formation of radicals initiates the polymerization of monomers, which changes the mass density as well as the material specific transversal relaxation time T_2 of the magnetization in MRI as a function of the absorbed dose. Therefore, PG may be evaluated either by CT [80,87,88] or by MRI [80,89]. The MRI evaluation is usually performed with a MSE sequence allowing quantitative measurement of the T_2 relaxation time (equation (1.5)). As for films, a proper calibration measurement of the same batch of polymer gel has to be performed for absolute dosimetry.

There are several pitfalls in PG dosimetry, which may introduce uncertainties in the dose measurement. These include interactions of the PG with oxygen or other chemicals (e.g. with the material of the storage container), temperature-dependence of the signal response in MRI, different histories of the calibration and measurement container as well as B_0 -inhomogeneities during MRI evaluation [85,90,91]. This requires a highly standardized protocol in PG dosimetry. If these protocols are met, PG offer the possibility to measure 3D-dose distributions in conventional radiotherapy as well as in MRgRT [92] or to verify motion compensation concepts in photon radiotherapy [90]. In addition, PG may especially be applied for QA-tests, where geometric information in 3D is of high interest as shown in this thesis.

1.3 Quality assurance

Due to the high complexity of modern clinical irradiation devices as well as that of the entire treatment process, it is necessary to routinely check all aspects for their proper functioning to guarantee accurate patient treatments. Besides measurement of the dosimetric performance (1.2.1 and 1.2.2), field size and the measurement of machine-related geometric parameters like isocenter

accuracy are of utmost importance. Also for MR devices, special QA-measurements for the *signal-to-noise ratio* (SNR), slice thickness or geometric distortions [93,94] are recommended, however, they are not mandatory for diagnostic devices. As radiation therapy uses images to position the patient and to create and adapt the treatment plan, the accurate geometrical representation of the patient anatomy is essential. Consequently, continuous quality assurance is indispensable for both the irradiation and imaging components. As there is a large number of general QA tests, only those with specific for MRgRT will be presented here.

1.3.1 Irradiation isocenter

The isocenter is a fixed point in space that is used as reference for the alignment of the patient as well as of all technical components. At conventional Linacs, the isocenter denotes the intersection point of the Gantry, couch and collimator-axes. As there will always be some alignment errors, the isocenter is practically defined as the center of the smallest sphere that still includes the axes under all angular settings of the gantry, couch and collimator [95,96]. The isocenter is typically defined with an accuracy better than 1 mm and is visualized by line-lasers mounted at the room walls.

For Linac-based radiosurgery, the isocenter accuracy may be checked by the so-called *Winston-Lutz test* or by simple star shot measurements on radiographic or radiochromic films [95,97,98]. These QA-tests use several beams which are irradiated from different gantry angles and use film dosimeters to visualize the beams. The reconstruction of the respective central beam axes on film allows determining the smallest circle (in 2D) or sphere (in 3D) touching or intersecting all beam axes, the so-called *isocircle (IC)* (or *Isosphere in 3D*). According to the definition of the isocenter, the center of this IC is referred to as *radiation isocenter*, and at conventional Linacs, the in-room lasers are adjusted to intersect at this point. One additional important parameter is the radius of this circle (IC_r), which measures the beam alignment and therefore the machine-related accuracy of the treatment. IC_r as well as the distance between the actual and the laser-marked IC position (IC_d) must be below a certain tolerance level to ensure accurate targeting of the tumor. If these thresholds are exceeded, the gantry or the in-room laser may have to be readjusted. When performing star shots in an MR-Linac, the presence of a magnetic field will deflect the secondary electrons (see 1.2) and as a consequence, asymmetric lateral dose profiles and thus altered test results for star shot measurements are expected. The IC_r is expected to increase in MR-Linacs, which in contrast to application in conventional radiotherapy can be attributed to the magnetic field rather than mechanical machine inaccuracies. Therefore existing test have to be reanalyzed and revised in the presence of the magnetic field. One possible method to compensate for this effect was recently introduced by the Utrecht group [99]. For their 1.5T MR-Linac System (Elekta Unity) they attached high density material directly to radiochromic films to reduce the range of the secondary electrons. By this, they were able to reduce the influence of the magnetic field to a minimum. However, this method does not offer the possibility to display the irradiation isocenter directly in 3D.

1.3.2 Isocenter alignment at MR-Linacs

While MRgRT-devices may still be equipped with lasers their accurate alignment with the irradiation isocenter is less critical in clinical practice, as the patient is finally setup by means of the

acquired MR-images. An additional reference point within the MR images, termed as *image isocenter*, is used to determine patient misalignments. In principle, the imaging isocenter is defined by the center of the magnet, and by design the magnetic field is most homogeneous and the magnetic field gradients are most linear at the isocenter. Ideally the imaging isocenter should not move in space and should coincide with the irradiation isocenter. For mechanical reasons, however, this alignment might not be fully realized leading to small deviations between radiation and imaging isocenter. The alignment of irradiation and imaging isocenter is also of great relevance for other image guided radiotherapy devices such as Linacs with x-ray CBCT or Tomotherapy devices [100,101].

The manufacturer's recommended workflow to check this alignment for the MRIdian relies on the correct alignment of the laser and several phantom measurements and is cumbersome: first, the laser/radiation isocenter coincidence has to be established by separately checking the isocenter position in the xy- and xz-plane by a film or ionization chamber array measurements using a star shot (as described in 1.3.1). Then, the lasers have to be adjusted to the measured irradiation isocenter as good as possible, and finally an MR scan of a cylindrical phantom positioned exactly by means of the lasers has to be performed. The image is then registered to a reference image of the phantom. The shifts identified during the registration process indicate the shift between the lasers and the MRI isocenter and from this shift, the displacement between the MRI and radiation isocenters can be deduced. The shift between both isocenters should be less than 1 mm [102].

The Elekta Unity system uses a different solution based on the integrated *electronic portal imaging device* (EPID [103,104]) to check the imaging and irradiation alignment [105]. This method offers a high accuracy, however, due to the lack of an EPID-device, it is not applicable at the MRIdian system used in this work.

1.3.3 Geometric MR Image Distortion

Even with perfectly aligned irradiation and imaging isocenters, additional uncertainties may arise due to image distortions leading to an inaccurate representation of the patient's anatomy in the MR image. MR image distortions result from machine-related sources like inhomogeneities of the static magnetic field, gradient non-linearities as well as eddy currents associated with the switching of the gradient coils [106–113]: The reconstruction of MR images requires linear gradients and a homogeneous magnetic field. In case of deviations from these prerequisites, the phases and frequencies of k-space are assigned to the wrong positions in real space. As a consequence, this results in a “wrong” and distorted representation of the patient geometry in the image. Since the magnetic field at the isocenter is most homogeneous and the homogeneity decreases towards the outer areas, the distortions also increase with increasing distance from the imaging isocenter. While this is less critical for purely diagnostic MRI-applications, these distortions may have significant impact on the delivered radiation dose in MRgRT [114] and are thus required not to exceed specific tolerance levels. To measure geometric distortions in MRI, objects with known dimensions, so-called *phantoms*, can be used to acquire an MR image and to compare this image with a ground truth, either a technical drawing or a distortion free CT-scan of the phantom. Modern MRI scanners use intrinsic distortion correction algorithms to display the images with minimal distortions. However, these algorithms must be checked for correctness and constancy of the entire system has to be assured.

The manufacturer's recommended workflow for this uses a 2D Phantom with a time consuming scanning routine. This phantom contains a single polymethylmethacrylat (PMMA) slab with contrast agent-filled bores. A detailed description of this phantom and the related measurement method can be found elsewhere [115,116]. This 2D phantom has to be scanned in 7 different orientations at different distances from the isocenter and does not provide full information of 3D image distortions.

1.3.4 *Workflow verification*

Besides machine-related QA-checks (as described in 1.3.1 – 1.3.3) the complete treatment chain has to be validated to establish new and complex treatment methods. This includes imaging for treatment planning and positioning, the treatment plan adaption or gating process as well as the dose delivery. For these workflow-specific QA procedures, so called end-to-end tests can be performed. By these tests, the overall uncertainty of the treatment process can be evaluated [117]. For this, special phantoms are required. Currently, however, dedicated phantoms exist only for conventional radiotherapy [118], and these cannot easily be transferred to MRgRT as they are not MR compatible. Recently, several dynamic MRI compatible phantoms for MR-Linac systems have been presented to perform end-to-end tests for intra-fractional motion (e.g. breathing) [119–121]. However, phantoms for the simulation of interfractional organ movements are not yet available, but are urgently needed to assess the geometric and dosimetric accuracy. Suitable phantoms need to be deformable in a reproducible way, MRI-compatible and need to have anthropomorphic image contrast. It is also of high interest to perform 3D measurements of the dose distribution. However, there are only a few materials that are well compatible with PGs, and those that are suitable cannot easily be used to produce complex shapes. Therefore, the need for a PG compatible and customizable container-material is high.

1.4 Aim of the thesis

Clinical implementation of MR-guided radiotherapy using MR-Linacs require new machine QA-measurements to assure accurate geometrical alignment and dose delivery. This thesis investigated the use of PG to measure the isocenter accuracy at the 0.35 T MRIdian MR-Linac in 3D. In addition, image distortion in 3D were investigated for a representative volume around the imaging isocenter. Both was realized by developing a dedicated phantom and performing validation measurements at the MRIdian MR-Linac. Furthermore, different 3D-printing materials and printing techniques were investigated for their compatibility with PG. The identified material and printing technique may be used in the future to construct complex phantoms that can be used for end-to-end-test in MRgRT.

2 Publications

This thesis is written in a cumulative format in accordance with the regulations of the Department of Physics and Astronomy of Heidelberg University. The thesis comprises three manuscripts published in international peer-reviewed journals and one additional manuscript published as a peer-reviewed conference paper. The manuscripts will be referred to by roman numerals. The author of this thesis is first and main author of publications I, II & III. In the case of publication IV, which was written by Alina Elter, he is the second author.

None of the publications have been used in other dissertations and have been reproduced with kind permission of PMB (IOPScience) (publications I, III & IV) and the Journal of Physics: Conference Series (IOPScience) (publication II).

List of publications

Publication I

Dorsch S, Mann P, Lang C, Haering P, Runz A and Karger, C P 2018 Feasibility of polymer gel-based measurements of radiation isocenter accuracy in magnetic fields *Phys. Med. Biol.* **63** 11NT02

Publication II

Dorsch S, Mann P, Elter A, Runz A, Klüter S and Karger C P 2019 Polymer gel-based measurements of the isocenter accuracy in an MR-LINAC *J. Phys. Conf. Ser.* **1305** 012007

Publication III

Dorsch, S., Mann, P, Elter A, Runz A, Spindeldreier C K, Klüter S and Karger C P 2019 Measurement of isocenter alignment accuracy and image distortion of a 0.35 T MR-Linac System *Phys. Med. Biol.* **64** 205011

Publication IV

Elter A, **Dorsch S**, Mann P, Runz A, Johnen W and Karger C P 2019 Compatibility of 3D printing materials and printing techniques with PAGAT gel dosimetry *Phys. Med. Biol.* **64** 04NT02

2.1 Thematic overview

The purpose of this work was the development of methods and phantoms for new QA-methods in MRgRT. In particular, machine-related QA, such as checking the alignment of irradiation and imaging isocenter and the measurement of MRI-related distortions were key elements of the development. In addition, new methods for the design of phantoms for workflow verification in the presence of interfractional organ movements were investigated. A thematic overview of the respective investigations and developments with the corresponding publications is displayed in Figure 6.

2.1.1 Irradiation-related accuracy

The accurate alignment between the mechanical components of the Linac and the irradiation isocenter as defined by the laser system is a central requirement of radiation therapy devices. In conventional radiotherapy, the achieved accuracy is usually determined by films with simple star shot measurements [95,97]. At MR-Linacs, however, accurate patient positioning is performed based on MR images rather than lasers. To ensure accurate irradiation imaging isocenter has to coincide with the radiation isocenter. For the validation of the alignment between irradiation and imaging isocenter, it is desirable to use an MR-visible radiation detector as this allows a direct evaluation without further image registration procedures.

MR-evaluated polymer-gel is a candidate for such a detector, however, it has to be evaluated, whether the PG-results agree with the gold standard film in terms of geometric accuracy. This was systematically investigated in publication I. After performing star-shot measurements with

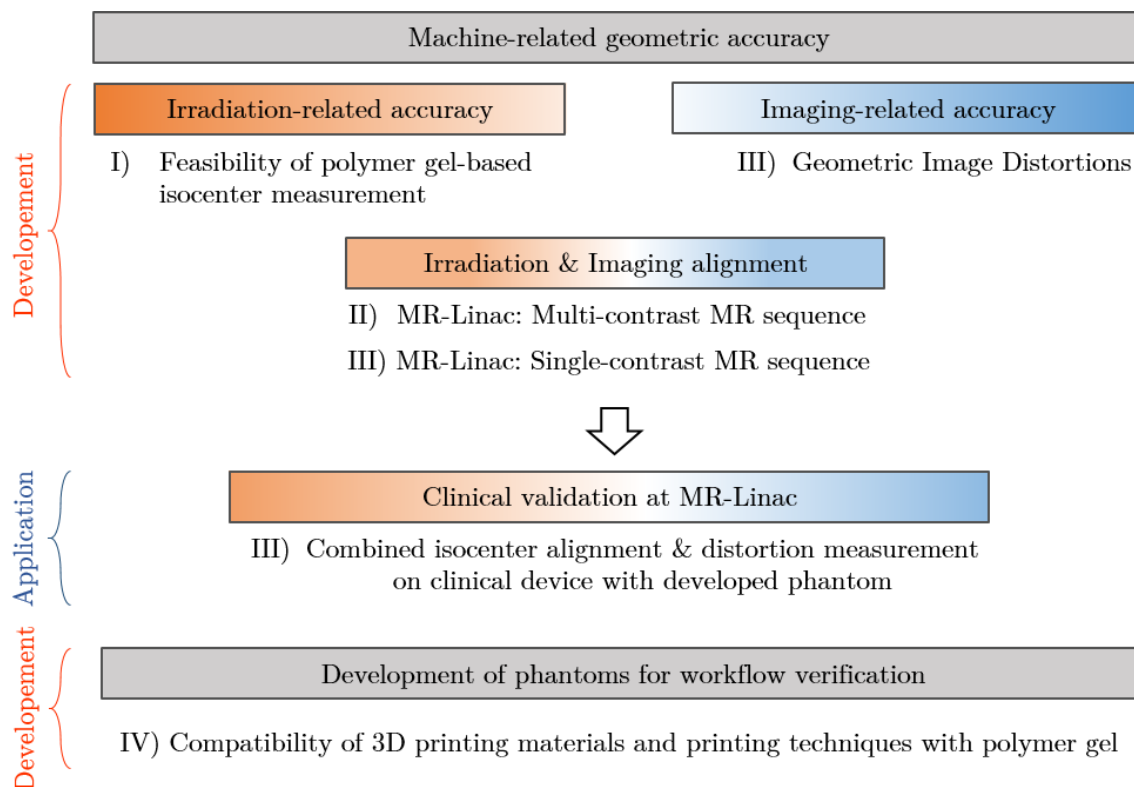


Figure 6. Thematic overview of the four publications (I-IV)

PG and films, the irradiated PG was MR scanned immediately, 1, 2 and 9 days after irradiation and no significant difference as compared to film measurements in terms of geometric accuracy was found.

Additionally the influence of a magnetic field on films and PG was investigated. As an MR-Linac was not yet available at the University Hospital Heidelberg, the magnetic field was generated by an experimental electro magnet. Also in these experiments, no significant differences between PG and film measurements were found. Thus geometric aspects of radiation fields in magnetic fields can be measured by polymer gels and evaluated by MRI immediately after irradiation.

2.1.2 *Imaging-related accuracy*

To quantify image-related uncertainties, publication III presents a new phantom to measure the machine-related image distortions resulting from inhomogeneities of the static magnetic field or gradient non-linearities, in 3D. The phantom consists of a water-filled PMMA-cylinder with 8 uniformly spaced regular plastic grids. The grid intersections define a total of 1330 control points with known ground truth positions obtained from CT. The measurements were compared to measurements of a commercial 2D phantom provided by the vendor of the MR-Linac device. The obtained accuracy fulfilled the requirements of MR-guided radiotherapy.

2.1.3 *Irradiation and Imaging alignment*

A major advantage of polymer dosimetry gels over film measurements is their 3D visibility in MRI, allowing for direct evaluation of the irradiation isocenter on the MR-unit of the MR-Linac.

Due to restricted availability of enhanced MR sequences shortly after the inauguration of the 0.35 T low-field MR-Linac at the University Hospital Heidelberg, the evaluation of the first irradiations of the PAGAT PG (publication II), were performed with two consecutively double spin-echo sequences with different echo times, applied immediately after irradiation and the images were used to generate T_2 -maps. To generate sufficient signal for evaluation, this multi-contrast measurement was limited to a slice thickness of 20 mm, which made a full 3D isocenter alignment analysis impossible. However, as for conventional star-shot measurements using films, the in-plane alignment of irradiation and imaging isocenter could be evaluated and the results were confirmed by separate measurements on a high field (3 T) MRI.

In contrast to the publications I & II, where multi-contrast MRI measurements were performed to generate quantitative T_2 -Maps, publication III used a single-contrast measurements with a turbo spin-echo sequence. These measurements revealed comparable results for the in-plane alignment of imaging and irradiation isocenter. This advanced sequence additionally offered the possibility to reduce the slice thickness as well as the signal amplification, leading to an isotropic spatial resolution of 1 mm.

2.1.4 *Clinical validation at the MR-Linac*

With the developed phantom, the isocenter alignment accuracy and image distortion were measured using the methods presented in 2.1.1 – 2.1.3. With this measurement, the first ever polymer-

gel based determination of irradiation and imaging isocenter alignment in 3D at a clinical MR-Linac was performed and is presented in publication III. The measurements were performed for different *number of signal averages* (NSA) and revealed a comparable isocenter accuracy of (0.6 ± 0.9) mm, (0.9 ± 0.9) mm and (0.8 ± 0.9) mm for 12, 24 and 32 NSA, respectively. Furthermore, the MRI sequences used for positioning and for the gel evaluation were analyzed for their geometric distortions. Both results meet the requirements of MR-guided radiotherapy.

2.1.5 *Development of phantoms for workflow verification*

As part of the development of a static deformable MRI-compatible phantom that also allows 3D dose validation measurements, various 3D printing materials and printing techniques were tested for their compatibility with the dosimetric PG. This was necessary as the previously used BAREXTM-containers lack the possibility to form complex shapes while the use of the 3D printing technique offers the possibility to produce a large variety of different container shapes. This is an important step towards the design of phantoms with different organ-like shaped 3D-printed PG containers, which can be used to simulate inter-fractional organ movements in patients while still being able to measure the dose in 3D.

2.2 Publication I

FEASIBILITY OF POLYMER GEL-BASED MEASUREMENTS OF RADIATION ISOCENTER ACCURACY IN MAGNETIC FIELDS

Authors: Dorsch S, Mann P, Lang C, Haering P, Runz A and Karger C P

Journal reference: *Physics in Medicine & Biology*, **63** (2018) 11NT02 (9pp)

DOI: 10.1088/1361-6560/aac228

Copyright notice: Open access, CC BY license which permits reuse for any purposes

Authors' contribution: This work investigates the feasibility of PG-based measurements of radiation isocenter accuracy in magnetic fields immediately after irradiation. A first production and evaluation workflow of the used PAGAT PG aiming at absolute dosimetry measurements was established by Philipp Mann in his PhD thesis in 2017. Aiming at evaluation the geometric accuracy of the PG only, I investigated and adapted this established workflow to evaluate the possibility of performing relative dosimetry immediately after irradiation rather than 48 hours after irradiation as it is necessary for absolute dosimetry due to the required stabilization time of the gel. In addition, I searched for suitable containers for the PG to perform irradiations within an electro magnet to investigate the influence of a magnetic field on the geometric properties of the PG and I performed the data analysis as well as the simulations. Finally, I wrote the manuscript, prepared all graphics and revised the manuscript in accordance with the reviewer's comments with support from Dr. Philipp Mann and Prof. Dr. Christian P Karger.

OPEN ACCESS



NOTE

Feasibility of polymer gel-based measurements of radiation isocenter accuracy in magnetic fields

RECEIVED
10 October 2017REVISED
30 April 2018ACCEPTED FOR PUBLICATION
3 May 2018PUBLISHED
29 May 2018

Original content from this work may be used under the terms of the [Creative Commons Attribution 3.0 licence](https://creativecommons.org/licenses/by/3.0/).

Any further distribution of this work must maintain attribution to the author(s) and the title of the work, journal citation and DOI.

S Dorsch^{1,2,3}, P Mann^{1,3}, C Lang^{1,3}, P Haering^{1,3}, A Runz^{1,3} and C P Karger^{1,3}¹ Department of Medical Physics in Radiation Oncology, German Cancer Research Center (DKFZ), INF 280, 69120 Heidelberg, Germany² Faculty of Physics and Astronomy, University of Heidelberg, Heidelberg, Germany³ National Center for Radiation Research in Oncology (NCRO), Heidelberg Institute for Radiation Oncology (HIRO), Heidelberg, GermanyE-mail: s.dorsch@dkfz.de**Keywords:** radiotherapy, quality assurance, star shot, gel dosimetry, magnetic resonance (MR) guided radiotherapy, isocenter accuracy**Abstract**

For conventional irradiation devices, the radiation isocenter accuracy is determined by star shot measurements on films. In magnetic resonance (MR)-guided radiotherapy devices, the results of this test may be altered by the magnetic field and the need to align the radiation and imaging isocenter may require a modification of measurement procedures. Polymer dosimetry gels (PG) may offer a way to perform both, the radiation and imaging isocenter test, however, first it has to be shown that PG reveal results comparable to the conventionally applied films. Therefore, star shot measurements were performed at a linear accelerator using PG as well as radiochromic films. PG were evaluated using MR imaging and the isocircle radius and the distance between the isocircle center and the room isocenter were determined. Two different types of experiments were performed: i) a standard star-shot isocenter test and (ii) a star shot, where the detectors were placed between the pole shoes of an experimental electro magnet operated either at 0 T or 1 T. For the standard star shot, PG evaluation was independent of the time delay after irradiation (1 h, 24 h, 48 h and 216 h) and the results were comparable to those of film measurements. Within the electro magnet, the isocircle radius increased from 0.39 ± 0.01 mm to 1.37 ± 0.01 mm for the film and from 0.44 ± 0.02 mm to 0.97 ± 0.02 mm for the PG-measurements, respectively. The isocenter distance was essentially dependent on the alignment of the magnet to the isocenter and was between 0.12 ± 0.02 mm and 0.82 ± 0.02 mm. The study demonstrates that evaluation of the PG directly after irradiation is feasible, if only geometrical parameters are of interest. This allows using PG for star shot measurements to evaluate the radiation isocenter accuracy with comparable accuracy as with radiochromic films.

1. Introduction

The integration of magnetic resonance imaging (MRI) into radiation devices such as linear accelerators (linac) or ⁶⁰Co-based systems, for MR-guided radiotherapy (MRgRT) (Lagendijk *et al* 2008, Fallone *et al* 2009, Keall *et al* 2014, Mutic 2014) is expected to allow for a better adaption of the dose distribution to anatomical changes due to the excellent soft-tissue contrast of MR images (Reiser *et al* 2008) as compared to image-guided procedures with x-rays in conventional radiotherapy. In contrast to x-rays, MRI does not involve exposure to ionizing radiation (Dirix *et al* 2014) and therefore allows repeated use, e.g. for online gating of moving targets (Heerkens *et al* 2014) or real time plan adaption (Kontaxis *et al* 2017). On the other hand, the static magnetic field will affect the trajectory of secondary electrons, which will result in a change of the dose distribution relative to that without magnetic field (Reiffel *et al* 2000, Raaijmakers *et al* 2004, Raaijmakers *et al* 2007a, 2007b, Kirkby *et al* 2008, Oborn *et al* 2009). In addition, the response of dose measuring devices, such as ionization chambers, is affected by the magnetic field as demonstrated by several studies (Meijsing *et al* 2009, Reynolds *et al* 2013, Smit *et al* 2013, Spindeldreier *et al* 2017). As a consequence, additional quality assurance measures have to be developed for these new devices.

As for many other high-precision radiotherapy techniques, the accuracy of the radiation isocenter is of central importance. For linac-based radiosurgery, the Winston–Lutz test (Lutz *et al* 1988) or simple star shot measurements (Treuer *et al* 2000) on radiographic or radiochromic films have been used for this purpose (Depuydt *et al* 2012). In MRgRT-devices, however, the deflection of secondary electrons by the magnetic field may lead to an asymmetric beam profile (Raaijmakers *et al* 2008). As a consequence, altered test results are expected, which in contrast to application in radiosurgery, cannot be attributed to solely mechanical machine inaccuracies. Thus the interpretation of the test results also has to be reconsidered. To compensate for the effect of the magnetic field, attaching high density material directly to the radiochromic films to reduce the range of the secondary electrons has been suggested (van Zijp *et al* 2016). As treatment plans in MRgRT are intended to be adapted based on MR-images, it is important to check not only the radiation, but also the imaging isocenter. This requirement is similar to that of combined imaging devices like positron emission and MR tomography (PET-MR), where the alignment of both imaging isocenters is always assumed (Judenhofer *et al* 2007, 2008). In MRgRT-devices, the radiation and imaging isocenter should ideally be checked simultaneously in a single measurement. For this purpose, polymer dosimetry gel (PG) could be used in the future as it can also be visualized in MRI.

After irradiation, PG polymerizes locally and alters the relaxation rate R_2 of the transverse magnetization in MRI depending on the locally absorbed radiation dose (Baldock *et al* 2010). Recently, it has been shown, that 3D-polymer gel dosimeters are a useful tool to verify motion compensation concepts in photon radiotherapy (Mann *et al* 2017) and to capture and resolve steep dose gradients in MRgRT (Roed *et al* 2017). Also other types of 3D gels were recently investigated in magnetic fields (Lee *et al* 2017a, 2018, Mein *et al* 2017) and only minimal B_0 -field effects were found (Lee *et al* 2017b). Up to now, however, the possibility of measuring the accuracy of the radiation and imaging isocenter has not been investigated.

As a first step into this direction, this study investigates whether PG can be used to determine the radiation isocenter via star shot measurements. Feasibility of such measurements is not evident as the handling of dosimetry gels encounters several difficulties: the sensitivity of the response to oxygen contaminations (De Deene *et al* 2006), temperature and evaluation time after irradiation, which is usually 48 h (Mann *et al* 2017). Without this time delay, it is especially impossible to perform absolute dose measurements due to large variations of the dose versus the R_2 calibration curve (Vandecasteele and De Deene 2013a). In this study, we therefore focus on geometrical aspects rather than quantitative dose evaluation and investigate whether the MR-evaluation can be performed directly after irradiation. In addition, we investigate whether PG and film measurements provide comparable results.

2. Material and methods

2.1. Experimental setup

In this study, the geometrical information on radiation isocenter accuracy obtained from PG measurements was compared with that obtained by radiochromic films (EBT3, ISP, Wayne, USA). For this, two types of experiments were performed: (i) to test the feasibility of PG for star shot measurements, the gel was poured into spherical flasks composed of borosilicate glass (outer diameter = 8.5 cm, volume = 250 ml, wall thickness = 1 mm). (ii) To compare the results of star shot measurements with and without external magnetic field, petri dishes composed of soda-lime glass (outer diameter = 10 cm, height = 2 cm, volume = 100 ml, wall thickness = 1 mm) were used as a gel container. The small height was necessary as the employed portable experimental electro magnet (AGEM 5520⁴, Schwarzbeck Mess-Elektronik, Schönau, Germany, output of the power supply: 250V/20A) allowed only for pole shoe distances of up to 3.5 cm, if a maximum magnetic field strength of 1 T is to be obtained. All irradiations were performed with a clinical linac (Artiste, Siemens Healthineers, Erlangen, Germany).

2.1.1. Polymer gel

Polymer gel measurements were performed using the PAGAT (PolyAcrylamide Gelatin gel fabricated at ATmospheric conditions) polymer gel. The gel consists of two different monomers (3% w/w acrylamide and 3% w/w N,N'-methylene-bis-acrylamide) as active components embedded within a gelatin matrix (6% w/w Gelatin, 300 bloom, SIGMA Aldrich). To minimize the influence of dissolved oxygen, 5 mM bis[tetrakis(hydroxymethyl) phosphonium] chloride (THPC) was added as an antioxidant. To further reduce the amount of dissolved oxygen, the gel was additionally flushed with nitrogen for 3 min directly before adding the antioxidant (De Deene *et al* 2002). A detailed description of the production procedure of the PG can be found elsewhere (De Deene 2006). After also flushing the containers with nitrogen, they were filled with PG. The containers were then enwrapped in aluminum foil and placed in a desiccator, which was entirely flushed with nitrogen, and stored in a refrigerator at 4 °C for 20–24 h. The gels were removed from the refrigerator 4 h before irradiation and stored at room temperature.

⁴<http://schwarzbeck.de/Datenblatt/k5520.pdf> last checked: 30 April 2018.

2.2. Measurements

2.2.1. Feasibility of polymer gel for star shot measurements

At our institution, the standard protocol for checking the isocenter accuracy for gantry rotations is a star shot measurement using a $40 \times 0.4 \text{ cm}^2$ field. This field is irradiated under nine equidistant gantry angles (20° , 60° , 100° , 140° , 180° , 220° , 260° , 300° and 340°) using 300 MU/angle and a dose rate of 300 MU min^{-1} . Gafchromic EBT3 films (size $11 \times 10 \text{ cm}^2$) were irradiated between two 1 cm slabs of water-equivalent material (RW3, PTW Freiburg, Germany) after marking the isocenter as defined by the in-room laser system (LAP GmbH Laser Applikationen, Lüneburg, Germany). For PG measurements, the spherical flask was positioned at the isocenter by means of three MR-visible markers (Beekly Medical, Bristol, USA) on the surface of the container. The same irradiation procedure as used for films was performed.

2.2.2. Star shot measurements with and without magnetic field

To investigate the isocenter accuracy for gantry rotations, the center of the electromagnet (figure 1(a)) was positioned at the isocenter with the magnetic field oriented parallel to the gantry axis (Yf according to (IEC 2011)) as shown in (figure 1(c)). Due to its weight (120 kg), the magnet had to be positioned by means of a special lifting cart (SPS/SPF, Hanse Lifter, Bremen, Germany), which limited the position accuracy to $\sim 0.5 \text{ mm}$. To allow for accurate and reproducible positioning of the petri dishes and the films inside the magnet a dedicated holder was 3D printed using the VeroClear material (RDG810, Stratasys, Eden Prairie, USA, density: $1.18\text{--}1.19 \text{ g cm}^{-3}$) and this holder was clamped between the pole shoes of the magnet (figures 1(a) and (b)). PMMA-plates for films and a printed mounting ring for the gel containers (figure 1(d)) can then be inserted into the holder. In this way, the PG and the film had a fixed spatial relation relative to the magnet. The positions of the room lasers were marked on both the film and the PG container using a MR-visible marker in the latter case. The star shot experiment was then performed either with or without a magnetic field of 1 T for both the PG and film resulting in a total of four measurements.

Due to the experimental setup, a slightly different irradiation protocol was followed as compared to the standard star shot procedure (section 2.2.1): (i) to avoid scattering caused by the magnet coils, a 5 mm circular collimator was used instead of a slit-field. (ii) The star shot was performed with five rather than nine beams (gantry angle (0° , 72° , 144° , 216° , 288°)). As a result, the overlap of the beams at the isocenter is reduced allowing for a better investigation of the deformed beam profile in the presence of high magnetic fields. (iii) Due to the lifting cart the gantry rotation was limited to angles between 260° and 80° . To obtain a comparable beam arrangement as for the standard star shot measurements without the electro magnet (section 2.2.1), the irradiation was performed in two steps: after irradiating the upper hemisphere (gantry angles of 288° , 0° and 72°), the gel containers and films were rotated by 180° around the axis of the magnet to mimic an irradiation from the lower hemisphere (corresponding to gantry angles 216° and 144°). This procedure resulted in a complete star shot with equidistant beams with angular distances of 72° between two adjacent beams. Inaccuracies which may have been introduced by this procedure are discussed below. (iv) To avoid overheating the magnet (a field strength of 1 T requires a coil current of 12 A), the operation time was kept to a minimum by using the flattening filter free mode of the linac at a dose rate of 2000 MU min^{-1} with a total of 500 MU/beam.

2.3. Evaluation

All films were scanned in the same orientation with an Epson 1000XL flatbed scanner (Epson Seiko Corporation, Nagano, Japan) with a resolution of 150 dpi. The laser isocenter was reconstructed by means of the marks on the film.

The PG containers were scanned on a 3 T Biograph mMR (Siemens Healthineers, Erlangen, Germany) inside a 16-channel head/neck coil using a multi-spin-echo sequence as implemented by the vendor with 32 equidistant echoes and a bandwidth (BW) of 130 Hz/pixel. For the standard star shot without the electro magnet (section 2.2.1), the irradiated gel container was scanned 1 h, 24 h, 48 h and 216 h after the irradiation using the following imaging parameters: Repetition time $TR = 5000 \text{ ms}$, echo time $TE = 30.0\text{--}960.0 \text{ ms}$ with an equidistant echo spacing of 30 ms, resolution = $0.5 \times 0.5 \text{ mm}^2$, employing a single slice with a thickness of 5 mm and a total acquisition time of 21 min 20 s. To assure reproducible measurements, the MR slice was positioned by means of MR-visible markers, which were attached to the PG container directly after irradiation using the room lasers.

For the measurement within the electromagnet (section 2.2.2), the irradiated gel container was scanned 48 h after the irradiation using the same imaging parameters. In both types of experiment, the isocenter was reconstructed using the MR-visible markers using a sequence with high spatial resolution ($0.5 \times 0.5 \times 0.5 \text{ mm}^3$ with $TR = 6.5 \text{ ms}$, $TE = 3.3 \text{ ms}$, number of averages = 2 and a flip angle of 50°).

The acquired data was transferred to a personal computer and processed by an in-house developed Matlab (The Mathworks Inc., Natick, USA)-based PG evaluation tool to generate T_2 -maps. A detailed description of the evaluation process has been described previously (Mann *et al* 2017).

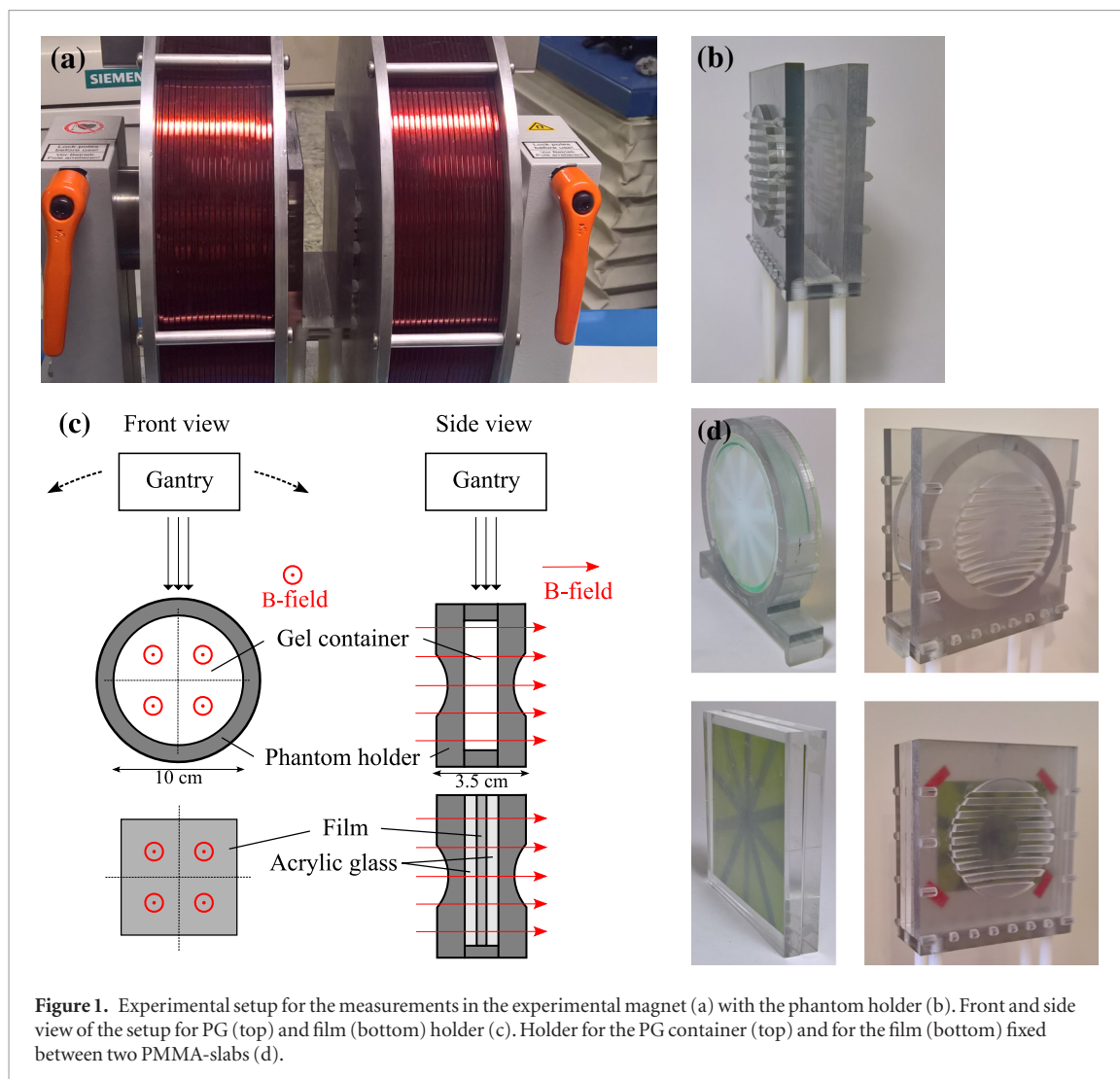


Figure 1. Experimental setup for the measurements in the experimental magnet (a) with the phantom holder (b). Front and side view of the setup for PG (top) and film (bottom) holder (c). Holder for the PG container (top) and for the film (bottom) fixed between two PMMA-slabs (d).

Afterwards, both film and gel images were evaluated with the commercial software Mephisto (Version mcc 1.8, PTW, Freiburg, Germany). This software tracks the individual beams in the image by a regression to the maximum positions of the lateral profiles along the individual beams. The smallest circle touching or intersecting all beam axes, the so-called isocircle (IC) is automatically determined. In conventional linacs, the radius of this circle (IC_r) is a measure of the beam alignment for different beam angles. A second important parameter is the distance (IC_d) of the IC center to the isocenter as defined by the laser system, indicating the alignment of the machine rotation center to the room isocenter. To determine the mean and standard deviation of the two parameters, each parameter was determined by six repeated evaluations in Mephisto reflecting the reproducibility of the film evaluation.

In addition, the profile of each individual beam was determined as the average over nine profiles located at a radial distance of 21 mm–23 mm from the isocenter with a spacing of 0.25 mm (figure 2(a)). The maximum position of the profile was determined as the average of the maximum positions of the individual profiles.

3. Results

3.1. Feasibility of polymer gel for star shot measurements

The evaluation of film and PG revealed comparable results for both IC_r and IC_d measurements (table 1). Furthermore, no significant changes over time were found for both parameters.

3.2. Star shot measurements with and without magnetic field

Figure 2 displays the film and PG scans performed in the experimental electromagnet for 0 T and 1 T, respectively. The corresponding results are given in table 2. While IC_r is well comparable for film and PG without magnetic field, IC_d shows a difference of 0.3 mm. At 1 T, the IC_r is increased markedly for film as well as for PG, while IC_d still exhibited small values for both measurement methods.

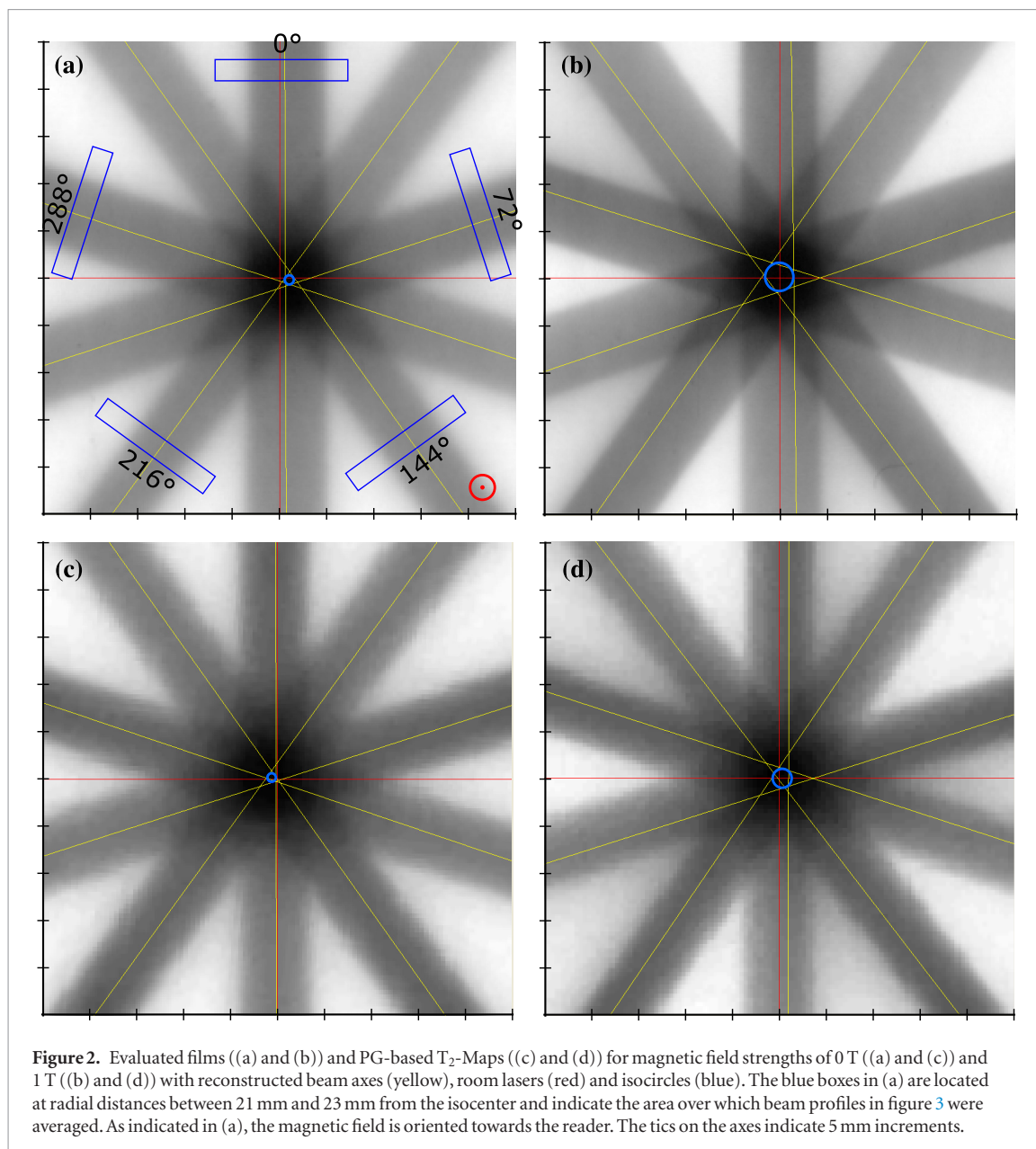


Table 1. Comparison of isocircle radii (IC_r) and isocircle distance to the isocenter (IC_d) for EDR3-film- and gel measurements (mean \pm 1 SD). Uncertainty was determined by repeated evaluation with the Mephisto software.

	Film [mm]	PG (1 h) [mm]	PG (24 h) [mm]	PG (48 h) [mm]	PG (216 h) [mm]
IC_r	0.26 ± 0.02	0.27 ± 0.02	0.27 ± 0.03	0.26 ± 0.04	0.26 ± 0.04
IC_d	0.70 ± 0.02	0.44 ± 0.03	0.40 ± 0.05	0.54 ± 0.05	0.38 ± 0.05

Table 2. Comparison of isocircle radii (IC_r) and isocircle distance (IC_d) to the isocenter for EBT3-film and PG measurements (mean \pm 1 SD) with and without magnetic field. Uncertainty was determined by repeated evaluation with the Mephisto software.

Magnetic field strength		Film [mm]	PG [mm]
0 T	IC_r	0.39 ± 0.01	0.44 ± 0.02
	IC_d	0.82 ± 0.02	0.52 ± 0.03
1 T	IC_r	1.37 ± 0.01	0.97 ± 0.02
	IC_d	0.12 ± 0.02	0.35 ± 0.07

Figure 3 displays the averaged relative lateral profiles as well as the maximum position for the five beam angles with and without magnetic field. The maximum positions determined by film and PG agree within the indicated uncertainty.

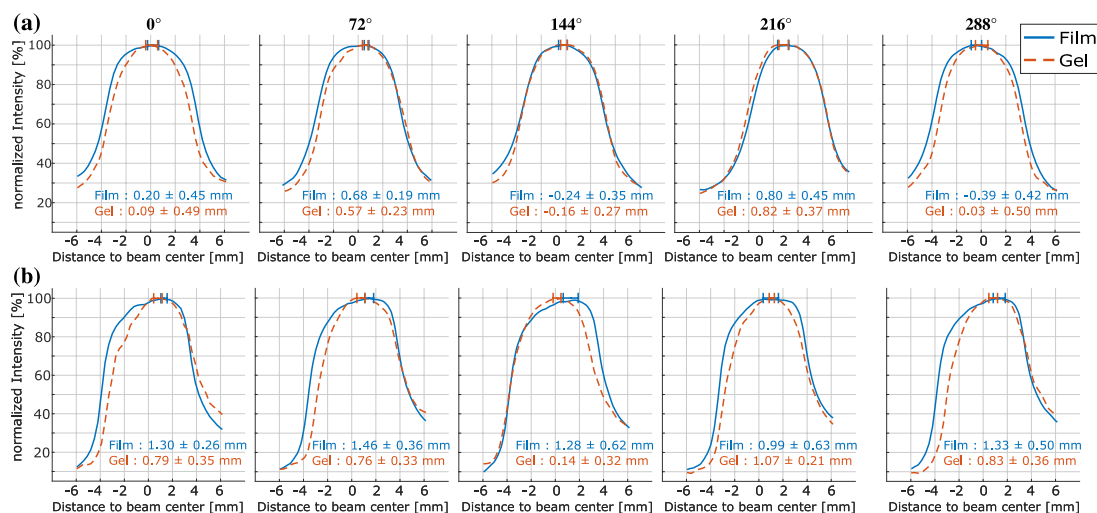


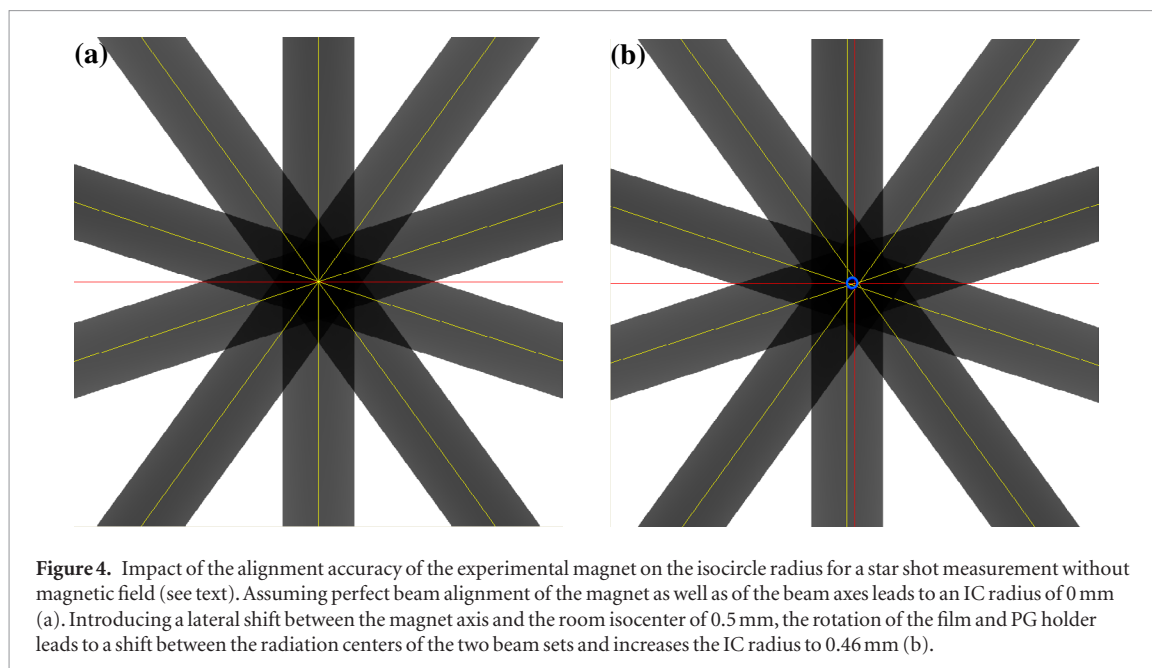
Figure 3. Comparison of the averaged relative lateral profiles ($n = 9$, optical density (OD) for film and T_2 -values for PG) measured by film- (blue) and PG (dashed red) for the different beam angles at 0 T (a) and 1 T (b). The area over which the averaging was performed is indicated by the blue boxes in figure 2. In addition, the mean \pm 1 SD of the maximum positions is displayed numerically and as horizontal error bars for both dosimeters.

4. Discussion

In this work, it has been shown that the PAGAT polymer gel is a versatile tool for measuring the radiation isocenter accuracy by means of a star shot in the same way as it is standard for films. Both methods exhibit comparable results in terms of geometric parameters and although the absolute T_2 -values of the PG without magnetic field decrease from 460 ms (after 1 h) to 420 ms (after 2 d) in the intersection area of the nine beams, the resulting geometric parameters (IC_r and IC_d) only have a negligible dependence on the time point of the evaluation. Furthermore, the tolerance level for a star shot measurement of 0.5 mm (IC_r), as recommended by the Task Group 142 report (Klein *et al* 2009), was always met. This means that the chemical effects of polymerization within 48 h post-irradiation do not play a major role, if only geometric parameters such as IC_r and IC_d are to be determined. This is a very important finding as it allows the evaluation of PG without any delay directly after irradiation. This is especially interesting for QA procedures for clinical MRgRT-devices.

Isocenter measurements using an electromagnet (section 2.2.2) without magnetic field revealed a slightly larger IC-radius for film and gel as compared to the standard star shot procedure (section 2.2.1), but still do not exceed the accepted limit of 0.5 mm. This increase can be explained by the rather complex experimental realization of the star shot in the presence of the magnet: due to the limitations in the accessible gantry angles, film and gel phantoms had to be rotated by 180° after irradiation of the first three beams to imitate a full gantry rotation. As this rotation is performed exactly around the axis of the magnet by construction of the film and PG holder, it may increase the isocircle radius due to a misalignment between the center of the magnet and the room isocenter. To get an idea of how this positioning uncertainty of the magnet affects the isocircle radius, we performed a simple geometrical simulation, in which we used the open-source software Inkscape together with the lateral beam profiles in absence of the magnetic field to synthetically generate the gray-scale distribution of the five beams. Then beam set 2 (144° and 216°) was shifted against beam set 1 (0°, 72°, 288°) by the assumed positioning uncertainty and the evaluation was repeated for this new beam arrangement (figure 4). Since this procedure does not account for the effects of a magnetic field, it gives only a rough estimation of the expected increase of the isocircle radius. While a standard star shot with perfectly aligned beam axes performed outside the experimental magnet would exhibit an isocircle radius of 0 mm in this simulation, a shift of 0.5 mm between the center of the magnet and the room isocenter would increase the IC-radius to 0.46 mm.

In the presence of a magnetic field, the profiles are always deformed towards the same direction relative to the beam orientation due to the Lorentz force acting on the secondary electrons and the reconstructed maximum lines of the beams are displaced accordingly. As a result, the IC-radius is further increased. With this in mind, it has to be noted that the IC-radius is solely a measure of mechanical alignment in conventional linacs while there are two components in MRgRT-devices: (i) the unknown mechanical alignment uncertainty and (ii) the deformation of the beam profiles. While the first is the relevant parameter, the latter does not contribute to the overall uncertainty in a clinical setting as the deformation of the beam profile is considered in the beam model used for treatment planning and is compensated by the inverse dose optimization. Thus the interpretation of an increased IC-radius is complicated and its relevance has to be reassessed.



To circumvent this problem, van Zijp *et al* (2016) attached copper rings to the film to reduce the range of the secondary electrons and as a result, the isocircle radius at a 1.5 T-MR-Linac device was reduced from 2.35 ± 0.35 mm to 0.22 ± 0.03 mm. To apply this approach in combination with PG, the interaction of a copper ring with the polymer gel has to be investigated. Another way to compensate for the deformation of the lateral profiles could be the use of opposing fields for the star shot measurements, which would lead to symmetric profiles. Finally, comparison with Monte Carlo simulations could be done to separate the effect of the magnetic field from that of mechanical uncertainties.

With respect to the determination of the beam axis via the maximum positions of the lateral beam profiles, we would like to point out that although the profiles are not given in terms of absorbed dose, both films and PG result in well comparable maximum positions (figure 3). Remaining differences may be attributed to the necessary rotation of the detectors in our experimental setting. This additionally supports the finding that both methods yield comparable isocenter radii with and without magnetic fields.

The second parameter is the distance between the isocircle center and the room isocenter, IC_d . For this parameter, the largest deviation was found for the film measurement without magnetic field (0.82 ± 0.02 mm), while all other measurements showed acceptable deviations of 0.5 mm or less. The variation of IC_d is most likely caused by difficulties in aligning the magnet center accurately to the room isocenter and introduced inaccuracies when marking the laser lines on the film. It is expected that the parameter IC_d is largely independent of the presence of the magnetic field as the beam directions are arranged symmetrically and as the deformation of the lateral dose distribution is always oriented towards the same side of the beam. In addition, as the results of film and PG measurements refer to independent measurements, a perfect agreement between both is also not expected.

Besides the positioning uncertainties of the magnet, one further source of error has to be mentioned: as the diameter of the pole shoes is only 7.5 cm, the magnetic field is rather inhomogeneous and the field strength drops to 50% at a distance of 5 cm from the center. The shift of the maximum of the beam profiles is therefore not constant along the beam axis, which may lead to somewhat different quantitative values of IC_r as in case of a measurement in a clinical MR-Linac device.

Although star shot measurements with films and PG yield comparable results, a disadvantage of PG measurements is the high logistic effort due the production, oxygen sensitivity and the MRI-based evaluation of the PG. On the other hand, however, our findings may allow the design of phantoms to check not only the radiation but also the imaging isocenter as the polymer gel is visible in MRI. Employing this finding in our study; that the PG can be evaluated directly after irradiation, future studies may investigate the use of PG to check the accuracy and coincidence of imaging and radiation isocenter of MRgRT-devices in a single measurement shortly after irradiation.

5. Conclusion

This study demonstrates that evaluation of the polymer gel directly after irradiation is feasible, if only geometrical parameters are of interest. This allows using polymer gels for star shot measurements to evaluate the radiation isocenter accuracy with comparable accuracy as with radiochromic films.

Acknowledgments

This work has received funding from the EMPIR programme co-financed by the Participating States and from the European Union's Horizon 2020 research and innovation programme. Additionally the authors would like to thank Professor Dr K Kopka for providing the lab space for the production of the polymer gel.

ORCID iDs

S Dorsch  <https://orcid.org/0000-0002-8185-8644>

References

- Baldock C, De Deene Y, Doran S, Ibbott G, Jirasek A, Lepage M, McAuley K B, Oldham M and Schreiner L J 2010 Polymer gel dosimetry *Phys. Med. Biol.* **55** R1–63
- De Deene Y, Hurley C, Venning A, Vergote K, Mather M, Healy B J and Baldock C 2002 A basic study of some normoxic polymer gel dosimeters *Phys. Med. Biol.* **47** 3441–63
- De Deene Y, Vergote K, Claeys C and De Wagter C 2006 The fundamental radiation properties of normoxic polymer gel dosimeters: a comparison between a methacrylic acid based gel and acrylamide based gels *Phys. Med. Biol.* **51** 653–73
- Depuydt T et al 2012 Computer-aided analysis of star shot films for high-accuracy radiation therapy treatment units *Phys. Med. Biol.* **57** 2997–3011
- Dirix P, Haustermans K and Vandecaveye V 2014 The value of magnetic resonance imaging for radiotherapy planning *Semin. Radiat. Oncol.* **24** 151–9
- Fallone B G, Murray B, Rathee S, Stanescu T, Steciw S, Vidakovic S, Blosser E and Tymofichuk D 2009 First MR images obtained during megavoltage photon irradiation from a prototype integrated linac-MR system *Med. Phys.* **36** 2084–8
- Heerkens H D, Van Vulpen M, Van Den Berg C A T, Tjissen R H N, Crijs S P M, Molenaar I Q, Van Santvoort H C, Reerink O and Meijer G J 2014 MRI-based tumor motion characterization and gating schemes for radiation therapy of pancreatic cancer *Radiother. Oncol.* **111** 252–7
- IEC 61217 2011 *Radiotherapy equipment—Coordinates, Movements and Scales* (Geneva: International Electrotechnical Commission) Document Number IEC 61217 Ed. 2.0 b:2011
- Judenhofer M S et al 2008 Simultaneous PET-MRI: A new approach for functional and morphological imaging *Nat. Med.* **14** 459–65
- Judenhofer M S, Catana C, Swann B K, Siegel S B, Jung W-I, Nutt R E, Cherry S R, Claussen C D and Pichler B J 2007 PET/MR images acquired with a compact MR-compatible PET detector in a 7 T magnet *Radiology* **244** 807–14
- Keall P J, Barton M and Crozier S 2014 The Australian magnetic resonance imaging-linac program *Semin. Radiat. Oncol.* **24** 203–6
- Kirkby C, Stanescu T, Rathee S, Carlone M, Murray B and Fallone B G 2008 Patient dosimetry for hybrid MRI-radiotherapy systems *Med. Phys.* **35** 1019–27
- Klein E E et al 2009 Task Group 142 report: quality assurance of medical accelerators *Med. Phys.* **36** 4197–212
- Kontaxis C, Bol G H, Stenkens B, Glitzner M, Prins F M, Kerkmeijer L G W, Lagendijk J J W and Raaymakers B W 2017 Towards fast online intrafraction replanning for free-breathing stereotactic body radiation therapy with the MR-linac *Phys. Med. Biol.* **62** 7233–48
- Lagendijk J J W, Raaymakers B W, Raaijmakers A J E, Overweg J, Brown K J, Kerkhof E M, van der Put R W, Hårdemark B, van Vulpen M and van der Heide U A 2008 MRI/linac integration *Radiother. Oncol.* **86** 25–9
- Lee H J, Choi G W, Alqathami M, Kadbi M and Ibbott G 2017a Using 3D dosimetry to quantify the electron return effect (ERE) for MR-image-guided radiation therapy (MR-IGRT) applications *J. Phys.: Conf. Ser.* **847** 12057
- Lee H J, Kadbi M, Bosco G and Ibbott G S 2018 Real-time volumetric relative dosimetry for magnetic resonance—image-guided radiation therapy (MR-IGRT) *Phys. Med. Biol.* **63** 045021
- Lee H J, Roed Y, Venkataraman S, Carroll M and Ibbott G S 2017b Investigation of magnetic field effects on the dose—response of 3D dosimeters for magnetic resonance—image guided radiation therapy applications *Radiother. Oncol.* **125** 426–32
- Lutz W, Winston K R and Maleki N 1988 A system for stereotactic radiosurgery with a linear accelerator *Int. J. Radiat. Oncol. Biol. Phys.* **14** 373–81
- Mann P, Witte M, Moser T, Lang C, Runz A, Johnen W, Berger M, Biederer J and Karger C P 2017 3D dosimetric validation of motion compensation concepts in radiotherapy using an anthropomorphic dynamic lung phantom *Phys. Med. Biol.* **62** 573–95
- Meijsing I, Raaymakers B W, Raaijmakers A J E, Kok J G M, Hogeweg L, Liu B and Lagendijk J J W 2009 Dosimetry for the MRI accelerator: the impact of a magnetic field on the response of a Farmer NE2571 ionization chamber *Phys. Med. Biol.* **54** 2993–3002
- Mein S, Rankine L, Adamovics J, Li H and Oldham M 2017 Development of a 3D remote dosimetry protocol compatible with MRgIMRT *Med. Phys.* **44** 6018–28
- Mutic S and Dempsey J F 2014 The viewray system: magnetic resonance-guided and controlled radiotherapy *Semin. Radiat. Oncol.* **24** 196–9
- Oborn B M, Metcalfe P E, Butson M J and Rosenfeld A B 2009 High resolution entry and exit Monte Carlo dose calculations from a linear accelerator 6 MV beam under the influence of transverse magnetic fields *Med. Phys.* **36** 3549–59
- Raaijmakers A J E, Raaymakers B W and Lagendijk J J W 2007a Experimental verification of magnetic field dose effects for the MRI-accelerator *Phys. Med. Biol.* **52** 4283–91
- Raaijmakers A J E, Raaymakers B W and Lagendijk J J W 2007b Integrating a MRI scanner with a 6MV radiotherapy accelerator: impact of the surface orientation on the entrance and exit dose due to the transverse magnetic field *Phys. Med. Biol.* **50** 1363–76
- Raaijmakers A J E, Raaymakers B W and Lagendijk J J W 2008 Magnetic-field-induced dose effects in MR-guided radiotherapy systems: dependence on the magnetic field strength *Phys. Med. Biol.* **53** 909–23
- Raaymakers B W, Raaijmakers A J E and Lagendijk J J W 2004 Integrating a MRI scanner with a 6 MV radiotherapy accelerator: dose deposition in a transverse magnetic field *Phys. Med. Biol.* **49** 4109–18
- Reiffel L, Li A, Chu J, Wheatley R W, Naqvi S, Pillsbury R and Saxena A 2000 Control of photon beam dose profiles by localized transverse magnetic fields *Phys. Med. Biol.* **45** N177–82
- Reiser M F, Semmler W and Hricak H 2008 *Magnetic Resonance Tomography* (Berlin: Springer) (<https://doi.org/10.1007/978-3-540-29355-2>)

- Reynolds M, Fallone B G and Rathee S 2013 Dose response of selected ion chambers in applied homogeneous transverse and longitudinal magnetic fields *Med. Phys.* **40** 42102
- Roed Y, Ding Y, Wen Z, Wang J, Pinsky L and Ibbott G 2017 The potential of polymer gel dosimeters for 3D MR-IGRT quality assurance *J. Phys.: Conf. Ser.* **847** 12059
- Smit K, van Asselen B, Kok J G M, Aalbers A H L, Lagendijk J J W and Raaymakers B W 2013 Towards reference dosimetry for the MR-linac: magnetic field correction of the ionization chamber reading *Phys. Med. Biol.* **58** 5945–57
- Spindeldreier C K, Schrenk O, Bakenecker K, Kawrakow I, Burigo L, Karger C P, Greilich S and Pfaffenberger A 2017 Radiation dosimetry in magnetic fields with Farmer-type ionization chambers: determination of magnetic field correction factors for different magnetic field strengths and field orientations *Phys. Med. Biol.* **62** 6708–28
- Treuer H, Hoevens M, Luyken K, Gierich A, Kocher M, Muller R-P and Sturm V 2000 On isocentre adjustment and quality control in linear accelerator based radiosurgery with circular collimators and room lasers *Phys. Med. Biol.* **45** 2331–42
- van Zijp H M, van Asselen B, Wolthaus J W H, Kok J M G, de Vries J H W, Ishakoglu K, Beld E, Lagendijk J J W and Raaymakers B W 2016 Minimizing the magnetic field effect in MR-linac specific QA-tests: the use of electron dense materials *Phys. Med. Biol.* **61** N50–9
- Vandecasteele J and De Deene Y 2013 On the validity of 3D polymer gel dosimetry: I. Reproducibility study *Phys. Med. Biol.* **58** 19–42

2.3 Publication II

POLYMER GEL-BASED MEASUREMENTS OF THE ISOCENTER ACCURACY IN AN MR-LINAC

Authors: Dorsch S, Mann P, Elter A, Runz A, Klüter S and Karger C P

Journal reference: *Journal of Physics: Conference Series*

DOI: 10.1088/1742-6596/1305/1/012007

Copyright notice: Open access, CC BY license which permits reuse for any purposes

Authors' contribution: This work presents a first irradiation of the PAGAT PG within a low field (0.35 T) MR-Linac for an isocenter alignment test in 2D with image acquisition immediately after irradiation. The limited possibility to access further developed MR sequences with improved image contrast made it necessary to use two consecutive dual spin-echo sequences to generate T₂-maps. Therefore the previously investigated process had to be adapted: I had to optimize the MR sequences with regard to noise and artefact reduction. Furthermore, I had to adjust the evaluation. As a result, an image with high slice thickness to increase signal intensity could be taken, however, it was therefore not possible to perform isocenter alignment measurements in 3D at that time. Additionally, I performed comparison measurement on a high field MRI. Finally, I wrote the manuscript, prepared all graphics and revised the manuscript in accordance with the reviewer's comments with support from Prof. Dr. Christian P Karger.

Polymer gel-based measurements of the isocenter accuracy in an MR-LINAC

S Dorsch^{1,2,4}, P Mann^{1,4}, A Elter^{1,2,4}, A Runz^{1,4}, S Klüter^{3,4} and C P Karger^{1,4}

¹Department of Medical Physics in Radiation Oncology, German Cancer Research Center (DKFZ), INF 280, 69120 Heidelberg, Germany

²Faculty of Physics and Astronomy, University of Heidelberg, Heidelberg, Germany

³Department of Radiation Oncology, University Hospital Heidelberg, INF 400, 69120 Heidelberg, Germany

⁴National Center for Radiation Research in Oncology (NCRO), Heidelberg Institute for Radiation Oncology (HIRO), Heidelberg, Germany

Email: s.dorsch@dkfz.de

Abstract. As magnetic resonance-guided radiotherapy (MRgRT) is becoming increasingly important in clinical applications, the development of new quality assurance (QA) methods is needed. One important aspect is the alignment of the radiation and imaging isocenter. MR-visible polymer gels offer a way to perform such measurements online and additionally may allow for 3-dimensional (3D) evaluation. We present a star shot measurement irradiated and scanned with a 0.35 T MR-LINAC device evaluating the polyacrylamide gelatin (PAGAT) gel dosimeter immediately and 48 h after irradiation. The gel was additionally scanned at a 3 T MR device 5 h and 52 h after irradiation. The evaluation revealed an isocircle radius of 0.5 mm for both imaging devices and all image resolutions and time points after irradiation. The distance between radiation and imaging isocenter varied between 0.25 mm and 1.30 mm depending on the applied image resolution. This demonstrates that evaluation of a star shot measurement in a 0.35 T MR-LINAC is feasible, even immediately after irradiation.

1. Introduction

Integrating magnetic resonance imaging (MRI) into radiation devices, such as linear accelerators (LINACs) or ⁶⁰Co-based systems [1-4], allows for image-guided radiation therapy (IGRT) improving the accuracy of dose delivery by acquisition of real-time images with excellent soft tissue contrast and without additional exposure of the patient. However, due to the static magnetic (B) field and the Lorentz force acting on the secondary electrons, the electrons will be deflected resulting in an altered dose distribution as compared to the case without magnetic field [5]. Therefore, the magnetic field changes not only the response of ionization chambers [6,7] but generates also asymmetric beam profiles [8], which may complicate geometrical quality assurance (QA) tests [9]: Most prominently, the isocircle radius, which is the smallest circle containing the central axis of all intersecting beams of a star shot measurement [10] - a well-established method for isocenter QA on conventional LINACs - will increase with increasing magnetic field strength. As a consequence, an increased isocircle radius cannot be attributed solely to mechanical machine misalignments. Therefore the interpretation of such tests also has to be reconsidered. To compensate for the effect of the magnetic field the use of high density material has been suggested [9].



Star shot measurements at conventional LINACs are usually performed with films. Using polymer gel (PG) instead, could offer a possibility to check the alignment between the irradiation and imaging isocenter [11] of MR-LINAC devices in 3D. Polymer gels [12] have revealed the same radiation isocenter accuracy as radiochromic films and can be evaluated immediately after irradiation, if only geometrical parameters are of interest [13]. In this paper we present the first irradiation of a star shot in PG within a 0.35 T MR-LINAC as well as the image-evaluation in the same device immediately and 48 h after irradiation. Additionally the PG was scanned with a 3 T MR device 5 h and 52 h after irradiation.

2. Material & Methods

2.1. Polymer gel

As PG the PAGAT (PolyAcrylamide Gelatin gel fabricated at ATmospheric conditions) [14] polymer gel was used (Table 1). A spherical flask composed of borosilicate glass was used as gel container (outer diameter = 8.5 cm, volume = 250 ml, wall thickness = 1 mm). The spherical flask was placed in the center of a cylindrical phantom (outer diameter = 23 cm) filled with a 3.6 g/l NaCl- and 1.25 g/l CuSO₄-solution.

Table 1. Composition of the used PAGAT polymer gel in weight percent and mmol.

Ingredient	amount
Water	89%
Gelatine	6%
Acrylamid	2.5%
N,N'-methylene-bis-acrylamide	2.5%
bis[tetrakis(hydroxymethyl)phosphonium] chloride (THPC)	5mM

2.2. Irradiation

The phantom was first aligned with a clinical 0.35 T MR-LINAC (MRIdian, ViewRAY, Oakwood Village, OH, USA) by means of dedicated fiducials on the gel-filled flask using the laser-system of the device. In a second step, MR-images were acquired and an image-based correction was performed to position the phantom exactly at the image isocenter of the device. The irradiation was performed with five beams (0°, 72°, 144°, 216° and 288°), a field size of 0.4 x 2.49 cm² and 3 Gy per beam at the isocenter.

2.3. Evaluation

Immediately after irradiation, the phantom was scanned on the MR-LINAC using two consecutive single slice double spin echo sequence with the following imaging parameters: TR = 2000 ms, TE_{1,1} = 200 ms, TE_{1,2} = 600 ms, TE_{2,1} = 400 ms, TE_{2,2} = 800 ms, slice thickness = 20 mm, resolution = 0.5 x 0.5 mm² and 4 averages with a total acquisition time of 1 h 15 min each. Imaging was repeated 48 h after irradiation when the polymerization of the PG was known to be completed. At this time point, another measurement with a better signal to noise ratio (SNR) was acquired using TR = 4000 ms, TE₁ = 200 ms, TE₂ = 600 ms, slice thickness = 20 mm, three averages and resolution = 1.0 x 1.0 mm².

In addition, a measurement on a 3 T Biograph mMR (Siemens Healthineers, Erlangen, Germany) was performed 5 h after irradiation using a single slice multi spin echo with 32 equidistant echoes with the following imaging parameters: TR= 4000 ms, TE = 30 – 960 ms, slice thickness = 20 mm and a resolution of 0.5 x 0.5 mm² with a total acquisition time of 29 min 10 s. This measurement was also repeated 52 h after irradiation and additionally with a better SNR using a resolution of 1.0 x 1.0 mm².

The acquired images were processed by an in-house developed Matlab (The Mathworks Inc., Natick, USA)-based PG evaluation tool [15] to generate T2-maps. The images prepared in this way were evaluated with the commercial software Mephisto (Version mcc 1.8, PTW, Freiburg, Germany). Each

beam was selected manually in the software and the isocircle was determined; this procedure was repeated 6 times to determine the standard deviation (SD) of the Mephisto evaluation.

3. Results

Figure 1 displays the evaluated T_2 -Maps for the different imaging devices and resolutions. The corresponding isocircle radii (IC_r) consistently revealed values of 0.5 mm independent of the applied imaging device and image resolution (Table 2). Reproducibility as indicated by the standard deviation (SD) was better by a factor of two for the 3T MR-device. The distance (IC_d) of the radiation isocenter, defined by the center of the isocircle, to the imaging isocenter, defined by the fiducials on the phantom, revealed values of up to 0.65 mm for the high- and up to 1.30 mm for the low-resolution images (Table 2).

Table 2. Isocircle radii (IC_r) and distance (IC_d) for the different imaging devices and resolutions (mean \pm 1 SD).

resolution [mm ²]	0.35 T MR-LINAC			3 T Biograph mMR		
	time point [h]	IC_r [mm]	IC_d [mm]	time point [h]	IC_r [mm]	IC_d [mm]
0.5 x 0.5	0	0.51 \pm 0.11	0.25 \pm 0.11	5	0.51 \pm 0.05	0.61 \pm 0.09
0.5 x 0.5	48	0.48 \pm 0.06	0.65 \pm 0.17	52	0.49 \pm 0.03	0.44 \pm 0.08
1.0 x 1.0	49	0.55 \pm 0.06	1.30 \pm 0.09	52	0.48 \pm 0.03	1.03 \pm 0.10

4. Discussion

This is the first study demonstrating the feasibility of star shot measurements in an MR-LINAC using PG. Although the images acquired with the 0.35 T MR-device of the MR-LINAC had a higher noise content than those of the 3 T device, well-comparable isocircle radii with clinically acceptable accuracy were obtained.

Since the 0.35 T MR-LINAC images with high resolution (0.5 x 0.5 mm² pixel size) showed a low SNR (Figure 1 (a) and (c)), an additional image with a resolution of 1.0 x 1.0 mm² was obtained 48 h after irradiation to analyze the effect of an improved SNR (Figure 1 (e)). As a result, the same isocircle radius was obtained indicating that the lower SNR of the high resolution images are still good enough for a quantitative evaluation. In contrast, the SNR of the images of the 3 T MR-device is much better even for the higher resolution (Figure 1 b,d,f), which however, did not lead to differences in the isocircle radii. It is thus feasible to determine geometric parameters like the isocircle radius even in images with very low SNR.

Additionally, it should also be mentioned that the automatic beam-fitting-algorithm of Mephisto was yet significantly less error prone using the MR-LINAC images with 1.0 x 1.0 pixel size in contrast to the 0.5 x 0.5 mm² pixel size.

The values determined for the isocircle distance are within the recommended tolerance limits for conventional LINACS (< 1 mm distance between the laser and the irradiation isocenter [16]) for measurements with 0.5 x 0.5 mm pixel size, for both images with 1x1 mm voxel size the values slightly exceed this recommended value. This is most likely due to the pixel size of 1 mm, which leads to an increased uncertainty in the determination of the fiducial position in the image. Since these fiducials represent the imaging isocenter, IC_d may be increased.

Furthermore, it should be noted that the T_2 -map of the images recorded on the MR LINAC was determined using only 4 echoes ($R^2 = 0.90-0.94$), so that it can be assumed that the fit over all echoes is not as stable as in the case with 32 echoes (3 T mMR $R^2 > 0.98$). Unfortunately, there is no multi-spin-echo sequences available on the MR-LINAC device, yet, but it is expected to be implemented soon. Since we intend to use the presented measurement technique in the future to measure the alignment accuracy of irradiation and imaging isocenter in 3D with an uncertainty of below 1mm in axial direction, it is essential to reduce the slice thickness from 20 mm to at least 1 mm. For this, the signal

intensity is expected to drop significantly ($\text{SNR} \sim \text{slice thickness}$), which would further decrease the signal to noise ratio. This may be compensated by using more numbers of signal averages/acquisitions (NSA) ($\text{SNR} \sim \sqrt{\text{NSA}}$), which however, will increase the measurement time. Nevertheless, we expect that the combination of extended measurement time and the use of a multi-spin-echo sequence with 32 echoes will significantly enhance the signal of the images, so that even images with a significantly reduced slice thickness may provide sufficient information to perform irradiation and imaging isocenter measurements.

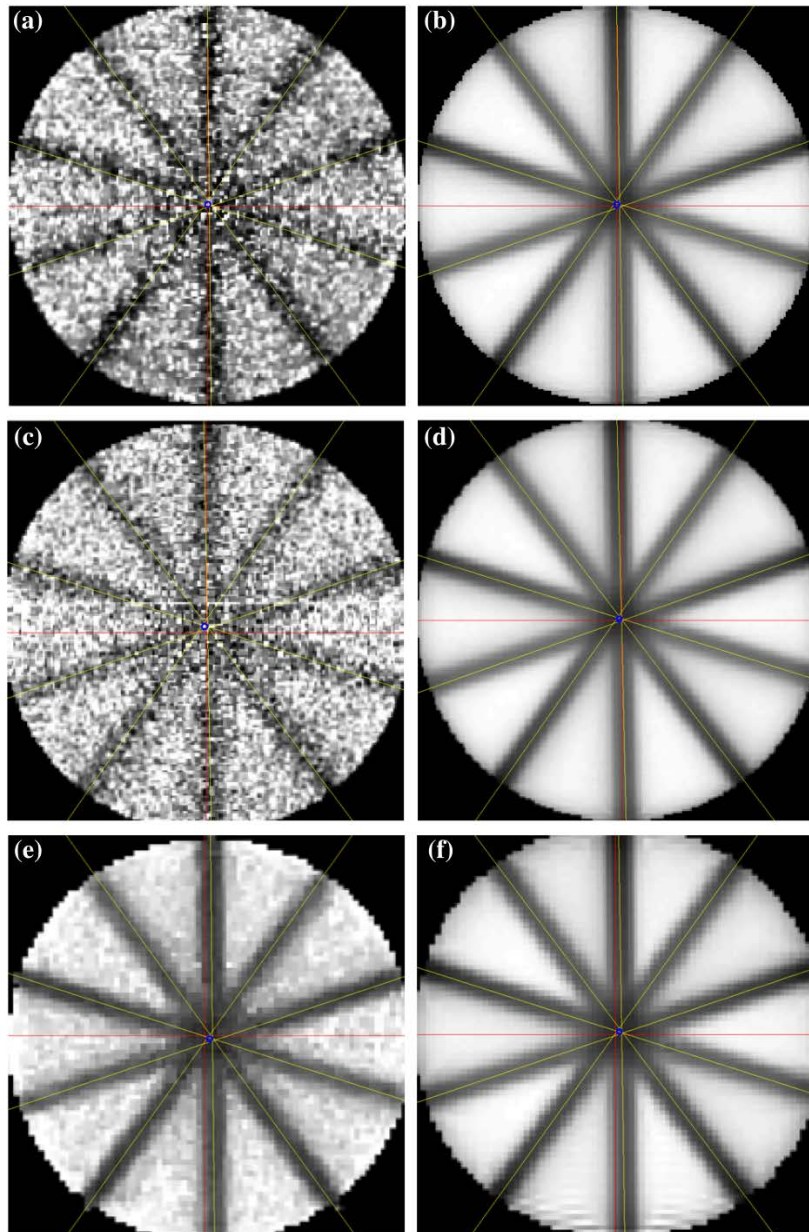


Figure 1. PG-based T_2 -Maps acquired with a 0.35 T MR-LINAC (a,c,e) and a 3 T MR device (b,d,f) at different time points after irradiation: immediately (a), 5 h (b), 48 h (c), 49 h (e) and 52 h (d,f) after irradiation. The magnetic field is orientated towards the reader. Resolution is $0.5 \times 0.5 \text{ mm}^2$ (a-d) and $1.0 \times 1.0 \text{ mm}^2$ (e,f). The isocircle is delineated in blue.

5. Conclusion

The evaluation of a star shot measurement in a 0.35 T MR-LINAC is feasible, even immediately after irradiation. Although the SNR was significantly worse than that of the 3 T device, well-comparable isocircle radii and isocenter distances were obtained for an image resolution of $0.5 \times 0.5 \text{ mm}^2$. With this low magnetic field strength, however, significantly longer acquisition times are needed.

6. Acknowledgments

This work has received funding from the EMPIR programme co-financed by the Participating States and from the European Union's Horizon 2020 research and innovation programme. Additionally the authors would like to thank Professor Dr. K. Kopka for providing the lab space for the production of the polymer gel.

7. References

- [1] Lagendijk J J W *et al* 2008 *Radiother. Oncol.* **86** 25-9
- [2] Fallone B G *et al.* 2009 *Med. Phys.* **36** 2084-8
- [3] Keall P J *et al* 2014 *Semin. Radiat. Oncol.* **24** 203-6
- [4] Mutic S *et al* 2014 *Semin. Radiat. Oncol.* **24** 196-9
- [5] Raaymakers B W *et al* 2004 *Phys. Med. Biol.* **50** 1363-76
- [6] Meijssing I *et al* 2009 *Phys. Med. Biol.* **54** 2993-3002
- [7] Smit K *et al* 2013 *Phys. Med. Biol.* **58** 5945-57
- [8] Raaijmakers J E *et al* 2008 *Phys. Med. Biol.* **53** 909-23
- [9] van Zijp H M *et al* 2016 *Phys. Med. Biol.* **61** N50-9
- [10] Treuer H *et al* 2000 *Phys. Med. Biol.* **45** 2331-42
- [11] Rankine L J *et al* 2013 *Phys. Med. Biol.* **58** 7791-801
- [12] Baldock C *et al* 2010 *Phys. Med. Biol.* **55** R1-63
- [13] Dorsch S *et al* 2018 *Phys. Med. Biol.* **63** 11NT02
- [14] De Deene Y *et al* 2002 *Phys. Med. Biol.* **47** 3441-63
- [15] Mann P *et al* 2017 *Phys. Med. Biol.* **62** 573-95
- [16] Klein E E *et al* 2009 *Med. Phys.* **36** 4197-212

2.4 Publication III

MEASUREMENT OF ISOCENTER ALIGNMENT ACCURACY AND IMAGE DISTORTION OF A 0.35 T MR-LINAC SYSTEM

Authors: Dorsch S, Mann P, Elter A, Runz A, Spindeldreier C K, Klüter S and Karger C P

Journal reference: *Physics in Medicine & Biology*, **64** (2019) 205011 (12pp)

DOI: 10.1088/1361-6560/ab4540

Copyright notice: Open access, CC BY license which permits reuse for any purposes

Authors' contribution: This study presents a new phantom to investigate MR-Linacs in terms of i) isocentricity of the irradiation and ii) alignment of the irradiation and imaging isocenter relative to each other using polymer dosimetry gel as well as iii) geometric MR image distortions in 3D. I was responsible for the development of the phantom, with Armin Runz supporting me from the engineering side (materials selection, technical drawings and coordination with the precision mechanics workshop). Furthermore, together with Philipp Mann, I optimized the MR sequences in terms of spatial resolution, signal enhancement and artifact reduction. I also developed and performed the evaluation as well for the PG-based measurement of the imaging and irradiation isocenter alignment as well as of the geometrical distortions. Dr. Philipp Mann, Dr. Kathrin Spindeldreier, Dr. Sebastian Klüter and Prof. Dr. Christian Karger supported me by advising me in different aspects. I wrote the manuscript, prepared all graphics and revised the manuscript in accordance with the reviewer's comments with support from Prof. Dr. Christian P Karger.

OPEN ACCESS






PAPER

Measurement of isocenter alignment accuracy and image distortion of an 0.35 T MR-Linac system

RECEIVED
6 May 2019REVISED
9 September 2019ACCEPTED FOR PUBLICATION
17 September 2019PUBLISHED
16 October 2019

Original content from this work may be used under the terms of the [Creative Commons Attribution 3.0 licence](https://creativecommons.org/licenses/by/4.0/).

Any further distribution of this work must maintain attribution to the author(s) and the title of the work, journal citation and DOI.

S Dorsch^{1,2,4,6}, P Mann^{1,4,5}, A Elter^{1,2,4}, A Runz^{1,4}, C K Spindeldreier^{3,4}, S Klüter^{3,4} and C P Karger^{1,4}¹ Department of Medical Physics in Radiation Oncology, German Cancer Research Center (DKFZ), INF 280, 69120 Heidelberg, Germany² Faculty of Physics and Astronomy, University of Heidelberg, Heidelberg, Germany³ Department of Radiation Oncology, University Hospital Heidelberg, INF 400, 69120 Heidelberg, Germany⁴ National Center for Radiation Research in Oncology (NCRO), Heidelberg Institute for Radiation Oncology (HIRO), Heidelberg, Germany⁵ HQ-Imaging GmbH, Heidelberg, Germany⁶ Author to whom correspondence should be addressed.E-mail: s.dorsch@dkfz.de**Keywords:** magnetic resonance (MR) guided radiotherapy (MRgRT), isocenter alignment, gel dosimetry, geometric distortions, quality assurance**Abstract**

For hybrid devices combining magnetic resonance (MR) imaging and a linac for radiation treatment, the isocenter accuracy as well as image distortions have to be checked. This study presents a new phantom to investigate MR-Linacs in a single measurement in terms of (i) isocentricity of the irradiation and (ii) alignment of the irradiation and imaging isocenter relative to each other using polymer dosimetry gel as well as (iii) 3-dimensional (3D) geometric MR image distortions. The evaluation of the irradiated gel was performed immediately after irradiation with the imaging component of the 0.35 T MR-Linac using a T2-weighted turbo spin-echo sequence. Eight plastic grid sheets within the phantom allow for measurement of geometric distortions in 3D by comparing the positions of the grid intersections (control points) within the MR-image with their nominal position obtained from a CT-scan. The distance of irradiation and imaging isocenter in 3D was found to be (0.8 ± 0.9) mm for measurements with 32 image acquisitions. The mean distortion over the whole phantom was (0.60 ± 0.28) mm and 99.8% of the evaluated control points had distortions below 1.5 mm. These geometrical uncertainties have to be considered by additional safety margins.

1. Introduction

Image-guidance is a key element of modern radiotherapy. Independent of the method, image-guidance may assist in patient setup, detection of anatomical changes during treatment or real-time motion management, e.g. by plan adaptations (Martinez *et al* 2001, Kontaxis *et al* 2017), gated or tracked treatments (Kubo *et al* 1996, Heerkens *et al* 2014). While most modern linear accelerators are equipped with on-board imaging systems to acquire images of the patient anatomy by kilo voltage Cone Beam Computed Tomography (kV-CBCT) (Jaffray *et al* 2002), hybrid devices for magnetic resonance (MR)-guided radiotherapy (MRgRT) have recently attracted much attention and became increasingly important (Lagendijk *et al* 2008, Fallone *et al* 2009, Keall *et al* 2014, Mutic and Dempsey 2014). In contrast to x-ray imaging, MR-imaging (MRI) is not linked to additional dose to the patient and provides superior soft tissue contrast (Reiser *et al* 2008). All radiotherapy machines require tests to assure accurate alignment of the irradiation isocenter to a certain point in space.

Determination of the irradiation isocenter is usually performed with films by simple star shot measurements (Treuer *et al* 2000) or the so-called Winston–Lutz test (Lutz *et al* 1988). These well-known quality assurance (QA) tests compare the measured irradiation isocenter position with a reference point in space that was formerly marked by accurately aligned room lasers. While MRgRT-devices may still be equipped with lasers their accurate alignment is less critical as the final setup is based on the acquired MR-images in which the isocenter is defined at a certain position (termed as imaging isocenter, which is identical to the nominal irradiation isocenter). The alignment of imaging and the actual irradiation isocenter is of great relevance across all devices dedicated to image-guided radiotherapy and is not restricted to MRgRT-devices.

The measurement of the isocenter-alignment in MRgRT-devices involves several requirements and problems regarding the phantom design as well as the evaluation procedure: (i) to allow for image- rather than laser-based positioning in the MRgRT-device, at least part of the phantom has to be visible in the MR-images. (ii) To visualize the irradiation isocenter, a 2D or 3D radiation detector is needed. (iii) To evaluate the isocenter alignment, the position of the imaging isocenter has to be either transferred to the detector or the measured position of the irradiation isocenter has to be transferred to the MR-image. While requirement (i) prevents solid state phantoms without any liquid structures, (ii) is usually realized by films. However, as the irradiation of films or radiochromic 3D dosimeters like PRESAGE[®] (Adamovics and Maryanski 2006, Brown *et al* 2008, Thomas *et al* 2013, Costa *et al* 2018) are not visible in the MR-images, the imaging isocenter has to be transferred to the resulting image of the dosimeter. As an alternative, polymer gel (PG) dosimeters (De Deene *et al* 1998) may be used. Irradiation of PG leads to local changes in mass density and relaxation rate due to polymerization of monomers (Baldock *et al* 2010), making unirradiated and irradiated parts distinguishable in CT (Hilts *et al* 2000) but also in MRI (Venning *et al* 2005). 3D Polymer gel dosimeters are a useful tool to verify motion compensation concepts in photon radiotherapy (Mann *et al* 2017) and their radiation response is only minimally influenced by magnetic fields (Lee *et al* 2017). In measurements of the isocenter accuracy, a significant advantage of PG is that it can be evaluated by the MRI unit of the MRgRT-device immediately after irradiation, if only geometric rather than dosimetric aspects are of interest. It has been shown previously, that results of geometrical measurements are well comparable to those of radiochromic films (Dorsch *et al* 2018).

A recent study demonstrated the coincidence of radiation and imaging isocenter in 3D for a conventional Linac with an onboard kV-CBCT (Adamson *et al* 2019). A first isocenter alignment measurement at a 0.35 T MR-Linac-System was presented by Dorsch *et al* (2019), however, this study used a suboptimal MR sequence with a slice thickness of 20 mm to generate a sufficiently high signal at this low field strength. The 2D image had a low signal-to-noise ratio and did not allow for isocenter alignment measurements in 3D. In the present study, we investigate the alignment accuracy of irradiation and imaging isocenter of a MR-Linac system in 3D using an isotropic spatial image resolution of 1 mm.

The intention of MRgRT, however, is not only to perform accurate image-based setup corrections, but also to detect anatomical changes and motion within the patients and to adapt the treatment plan as well as the delivery accordingly. Besides accurate isocenter alignment, this also requires distortion-minimized images, which is more difficult to achieve for MR- than for x-ray images. MRI distortions result from inhomogeneities of the static magnetic field, susceptibility effects originating from the scanned object as well as gradient non-linearities (Schad *et al* 1992, Janke *et al* 2004, Wang *et al* 2004b, 2004b, Doran *et al* 2005, Reinsberg *et al* 2005, Baldwin *et al* 2007, Tadic *et al* 2014) and increase with increasing distance from the center of the magnet. While this is less critical for purely diagnostic MRI-applications, these distortions may have impact on the delivered radiation dose in MRgRT (Yan *et al* 2018) and are required not to exceed certain thresholds. Distortions in MRI can be measured by employing a stack of regularly arranged grids and by comparing the positions of the grid intersections in the image with their nominal positions (Wang *et al* 2004a, Stanescu *et al* 2010).

In general any regular geometric structure can be used and various commercial phantom solutions exist (for 2D-measurements: the ACR-phantom (American College Of Radiology 2005) and the spatial integrity phantom (Fluke Biomedical, Everett, WA); for 3D-measurements: the MAGPHAN[®] phantom series (The Phantom Laboratory, Greenwich, NY, USA)). Also spherical harmonic analysis (Janke *et al* 2004, Tadic *et al* 2014) has been used to quantify geometric distortions in 3D (Phantom: ModusQA MRI^{3D} (Modus Medical Devices Inc., London, Canada)).

In addition to the measurement of the isocenter alignment by PG also geometric image distortions are performed in this study. For this, a new phantom was developed allowing both measurements to be performed either simultaneously while disregarding distortions near to the isocenter or sequentially, which provides the distortions over the whole phantom volume.

2. Material and methods

2.1. Experimental setup

For this study a special QA phantom was developed, to investigate a 0.35 T MR-Linac (MRIdian, ViewRay, Inc., Oakwood Village, OH, USA) (Klüter 2019) in terms of (i) isocentricity of the irradiation, (ii) alignment of the irradiation isocenter and imaging isocenter to each other, and (iii) geometric image distortions using the clinically applied MR sequences.

2.1.1. Phantom

The phantom (figure 1) consists of a polymethyl-methacrylate (PMMA) cylinder (height 23.5 cm, diameter 20 cm) containing a mounting for a spherical glass flask (borosilicate glass with outer diameter 8.5 cm, volume 250 ml, wall thickness: 1 mm) at the center, which can be filled with PG. The gel container is surrounded by

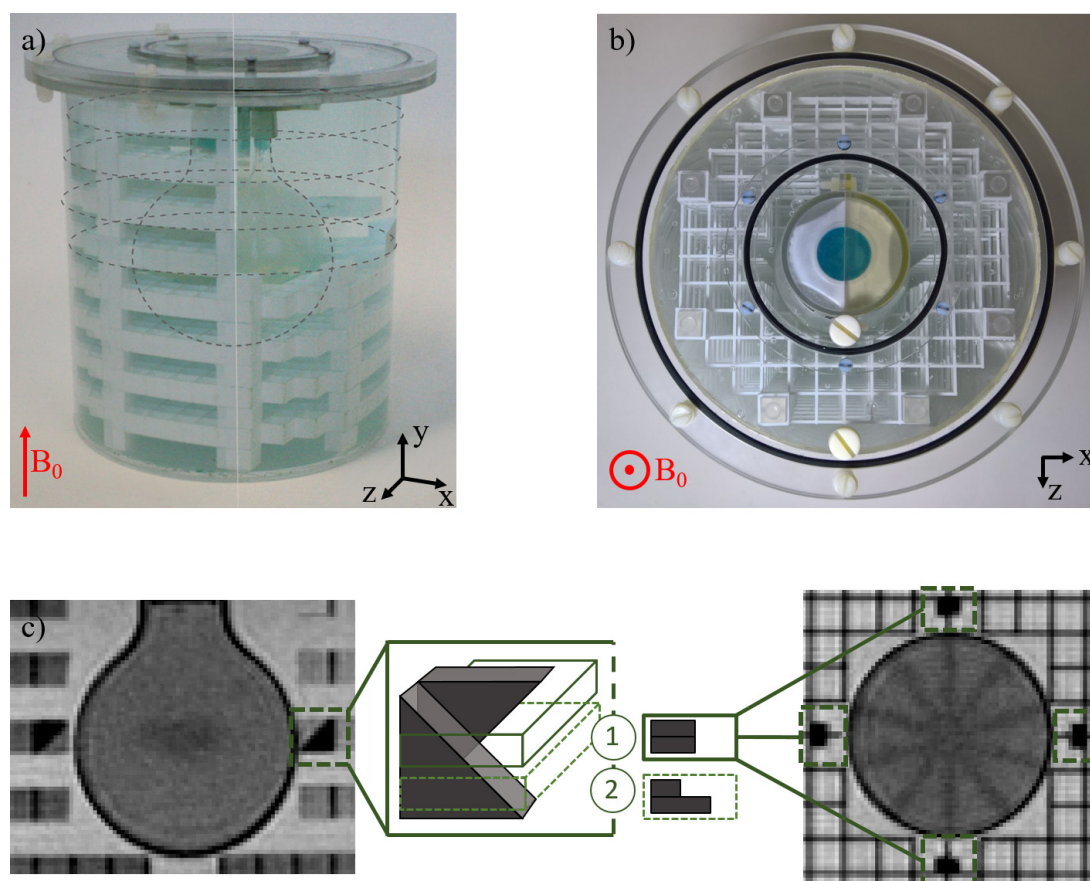


Figure 1. (a) Side view of the in-house developed phantom with the inserted gel container (overlay of images of the complete phantom and the phantom where 4 of the 8 grids were removed). (b) Top view showing the upper grid. (c) Corresponding MR-images of the container together with the wedge-shaped fiducials in coronal (left) and transversal (right) planes. (1) For a slice position centered exactly at the intersection of the wedge pair, two equally long dark bars are seen in the image resulting from an extinction of the MR signal by the solid material of the wedges. (2) If the slice position is off-center, the bars will have different lengths.

eight uniformly spaced, regular plastic grids (thickness 12.8 mm), which are used to measure geometric image distortions in the xz -plane. By means of eight rods, the grids are aligned within the phantom as well as with respect to each other. The distance between the grids was maintained by spacers on the rods (height 12.8 mm). In each plane, the grid intersections serve as control points and the distortions are obtained by comparing the control point positions in the image with their nominal positions obtained from a CT scan. In the xz -plane, the spacing of the grid is $14.2\text{ mm} \times 14.2\text{ mm}$ and distance of two neighbouring control points in y -direction is 25.6 mm (coordinate system according to ViewRay & IEC61217 system (International Electrotechnical Commission 2011), see figure 1). In total, the phantom contains 994 control points. According to a recommendation of AAPM Report 100 for MR QA (American Association of Physicists in Medicine 2010), the phantom is filled with a 3.6 g l^{-1} NaCl- and 1.25 g l^{-1} CuSO_4 -solution to enhance the conductivity and reduce the T1-relaxation time constant.

To fine-tune the alignment of the phantom in the MR-Linac, four pairs of wedges marking the center of the spherical flask are placed in the phantom (figure 1). The wedges ($12\text{ mm} \times 12\text{ mm} \times 4\text{ mm}$, 45° slope) are realized by 3D printing (VeroClear™-material and Objet30 pro 3D-printer, StrataSys, Eden Prairie, USA) and are visualized in the MR-image due to their signal extinction in contrast to the surrounding solution. Only if the image slice is centered with respect to the four wedges, the contributing pixels of the fiducials in the image appear with the same length (figure 1(c)). A similar technique is used to measure the slice position accuracy for the standard ACR phantom measurement. In addition, these markers are used to define the nominal irradiation isocenter in the treatment planning system (TPS). With this phantom configuration, isocenter accuracy and image distortions can be measured simultaneously disregarding potential distortions in the isocenter region. By replacing the combination of the gel container and grid by a continuous grid that fills the whole phantom (1330 control points), the distortions can be measured also in the isocenter region. In this case, isocenter accuracy and image distortions have to be measured sequentially.

For additional comparison with our distortion measurements, the commercial 2D spatial integrity phantom (Fluke Biomedical, Everett, WA) was employed. This phantom contains a single PMMA slab with contrast

agent-filled bores. A detailed description of this phantom and the related measurement method can be found elsewhere (Ginn *et al* 2017, Green *et al* 2018).

2.1.2. Polymer gel

For the polymer gel measurements the PAGAT (PolyAcrylamide Gelatin gel fabricated at Atmospheric conditions) polymer gel was used due to its visibility in MRI, low dose rate dependence (De Deene *et al* 2006) and low in-house manufacturing costs. The gel consists of two different monomers (2.5% w/w acrylamide and 2.5% w/w N,N'-methylene-bis-acrylamide) as active components embedded within a gelatin matrix (6% w/w Gelatin, 300 bloom, SIGMA Aldrich). Additionally, 5 mM bis[tetrakis(hydroxymethyl)phosphonium] chloride (THPC) was used as radical scavenger to reduce the influence of dissolved oxygen. In addition, the gel was flushed with nitrogen for 1–2 min directly before adding the antioxidant resulting in a reduced amount of dissolved oxygen (De Deene *et al* 2002). As a next step, the PG was filled in a spherical flask (also previously flushed with nitrogen), sealed with a plug, enwrapped in aluminum foil, and placed in a desiccator. The desiccator was completely flooded with nitrogen to store the flask in a low oxygen atmosphere until irradiation. Additionally, it was stored in a refrigerator at 4 °C for 20–24 h. Four hours before irradiation the desiccator was removed from the refrigerator and stored at room temperature (Vandecasteele and De Deene 2013, Mann *et al* 2017) such that the gel was in a temperature equilibrium with its surrounding at the time of irradiation.

In general, irradiation of the PG leads to polymerization and a change of the R2-relaxation rate of the PG measured quantitatively in MRI by means of a multi-spin-echo sequence (Baldock *et al* 2010). After proper calibration, changes in R2 can be converted into dose (Venning *et al* 2005). As this study investigates only geometrical aspects, a calibration and conversion into dose was not performed. It has been shown that uncalibrated PAGAT polymer gels lead to comparable results in terms of geometric parameters in irradiation isocenter measurements as the gold standard radiochromic film (Dorsch *et al* 2018).

2.2. Measurements

2.2.1. Isocentricity and alignment of irradiation and imaging isocenter

The developed phantom was inserted in an additional PMMA tube at the clinical 0.35 T MR-Linac, allowing the complete enclosure of the phantom with the pair of surface flex coils of the MR-Linac system (12 receiver channels) without moving the phantom by the coil positioning. Then, the phantom was aligned by aligning the crosshairs on the phantom surface to the lasers of the device. The longitudinal axis of the phantom was oriented along the main magnetic field. In a second step, MR-images were acquired, using a TrueFISP sequence (Balanced Steady State Free Precession (bSSFP) (Bieri and Scheffler 2013) used for clinical routine measurements as implemented by the vendor (echo time TE 1.45 ms, repetition time TR 3.35 ms, pixel bandwidth 537 Hz/pixel, FOV 349 mm × 400 mm × 360 mm, resolution 1.5 mm × 1.5 mm, slice thickness 1.5 mm, flip angle 60° and total acquisition time t_a 2 min 53 s). A rigid translational image-based position correction was performed using the wedge-based fiducials to align the phantom exactly at the nominal irradiation isocenter of the device. With this procedure, any additional tilting of the phantom can be detected and corrected easily.

The aligned phantom was irradiated according to a pre-calculated plan generated with the ViewRay treatment planning system (Version 5.2.4, ViewRay, Inc., Oakwood Village, OH, USA). The irradiation was performed with five beams of equiangular distance (0°, 72°, 144°, 216° and 288°), a field size of 4 mm × 12 mm (in-plane and axial direction) and a prescribed dose of 4 Gy per beam at the isocenter.

Directly after irradiation, the phantom was imaged on the MR-Linac. As a standard multi-spin echo sequence was not available on the system, a T2-weighted turbo spin echo⁷ (T2w-TSE) sequence was used. This allowed for a very small slice thickness of only 1 mm, which was necessary to determine the position of the irradiation isocenter in *y*-direction with sufficient accuracy. Only the part of the phantom, where PG polymerization was expected was imaged with a field of view (FOV) of 128 × 128 × 20 mm³ with the following imaging parameters: TR 5460 ms, TE 516 ms, echo train length/turbo factor 15, pixel bandwidth 40 Hz/pixel, phase oversampling 100%, flip angle of 180°, 20 slices with an isotropic image resolution of 1 × 1 × 1 mm³ and number of signal acquisitions (NSA) of 12, 24 and 32 with a total acquisition time of 39 min 18 s, 1 h 18 min 36 s and 1 h 45 min 04 s, respectively. All scans were performed with distortion correction and without intensity correction.

2.2.2. Geometric distortions

To measure image distortions, the phantom was scanned in two configurations: (i) using the combination of gel container and grid inserts (simultaneous measurement of isocenter accuracy and image distortion), and (ii) using the continuous grid (distortion measurement only, including the isocenter region). For this, a clinically applied bSSFP MR imaging-sequence implemented on the MR-Linac was used, as described in section 2.2.1. To validate the implemented distortion correction of the MR-Linac device, each measurement was performed with and

⁷Research sequence not available on the commercial MRIdian.

without the correction. As ground truth, a CT scan of the phantom was performed using a Somatom Definition Flash (Siemens Healthineers, Forchheim, Germany) scanner with the following parameters: voltage 120 kVp, current 600 mAs, slice thickness = 0.6 mm, and a resolution of $1 \times 1 \text{ mm}^2$. Additionally, sequence-related distortions caused by the turbo spin-echo sequence, which was used for PG measurement (see section 2.2.1), were also quantified by measuring the central grid of the phantom but with an increased FOV of $186 \times 186 \text{ mm}^2$ to scan the whole grid structure of the phantom. For comparison, all distortion measurements were repeated with the commercial 2D Phantom. For this, the applied bSSFP sequence as described in section 2.2.1 was slightly modified by employing a larger FOV and slice thickness of 3 mm resulting in a resolution of $1.5 \times 1.5 \times 3.0 \text{ mm}^3$. The 2D phantom was scanned in one central coronal and transversal as well as in five sagittal planes (at -12.5 cm , -7 cm , 0 cm , 7 cm , 12.5 cm distance from the isocenter) with enabled distortion correction. All measurements were performed at a gantry angle of 0° .

NEMA SNR (National Electrical Manufacturers Association 2001) and ACR measurements are regularly performed on the MR-Linac device. To additionally investigate the influence of susceptibility effects induced by the glass a B_0 -mapping (dual-echo method) was performed (Schneider and Glover 1991, Webb and Macovski 1991).

2.3. Evaluation

2.3.1. Isocentricity and alignment with imaging isocenter

The acquired images were transferred to a personal computer and processed by an in-house developed Matlab (The Mathworks Inc., Natick, USA)-based PG evaluation tool (Mann *et al* 2017). To determine the position of the irradiation isocenter in axial direction, the beam profile of each individual beam in y -direction was investigated. To compensate for the low signal-to-noise ratio (SNR) (figure 2(a)), the profiles were averaged over a 15 mm area along the beam axis. The profiles were averaged separately for the beam entry (figure 2(a) red area) and exit (figure 2(a) blue area) side.

This averaged signal profile was then plotted against the corresponding slice number (see figure 4(c)). To determine y -coordinate of the isocenter position, the middle of the full width at half maximum (FWHM) of the averaged profile was determined. The difference of the y -positions on the entry and exit sides of the beams may also be used together with the trigonometric relationship $\alpha = \arctan(d_1/d_2)$ (figure 2(b)) to detect a potential inclination of the beam originating from a gantry tilt.

To determine the irradiation center in the transversal plane, the commercial software Mephisto (Version mcc 1.8, PTW, Freiburg, Germany) was used. This software reconstructs the individual beams in each image slice by performing regression over the maximum positions of the lateral profiles along the pre-estimated beam axis. As a result, the so-called isocircle (IC) is determined, defined as the smallest circle touching or intersecting all of the reconstructed beam axes. The radius of this isocircle (ICr) is a quality indicator of the beam alignment for different beam angles. The center of this isocircle is then defined as the radiation isocenter. Comparing this position with the position of the imaging isocenter, reconstructed by means of the wedge-shaped fiducials in the images, the distance between the irradiation and imaging (ICd) can be calculated for each individual slice. Together with the beam position in axial direction, the distance of imaging and irradiation isocenter can be determined in 3D. In addition, an SNR analysis was performed using the mean and SD of a region of interest (ROI), which is comparable to the SNR_{mult}-method described elsewhere (Dietrich *et al* 2007).

2.3.2. Geometric distortions

The automatic detection of the control points was performed using the trainable Weka segmentation (Version 3.3.92, University of Waikato, Hamilton, New Zealand) for Image J (Version 1.52h National Institute of Health, Bethesda, USA). First, a classifier with two different classes (figure 3(a)) was created by manually selecting both, control points of the grid and characteristic points of the phantom (e.g. the phantom wall or the fixation rods). After this step, the classifier was able to perform a full segmentation of all control points on the selected images. This was controlled by eye and falsely detected control points were removed manually. To derive the coordinates (given as floating point numbers) of each control point, which include between 1 and 9 pixels, a center of mass analysis was performed. Both MR and CT images were evaluated this way. The images of the commercial 2D phantom were evaluated by an automated software provided by ViewRay.

3. Results

3.1. Irradiation isocenter accuracy and alignment of irradiation and imaging isocenter

The results of the beam position in axial direction for NSA = 12, 24 or 32 are displayed in table 1 and figure 4. Although no significant differences were found between the measurements with different averages, a lower number of acquisition numbers resulted in larger uncertainties. The nominal radiation isocenter position in axial direction was located at the interface between slice #10 and #11. The mean distance between the irradiation

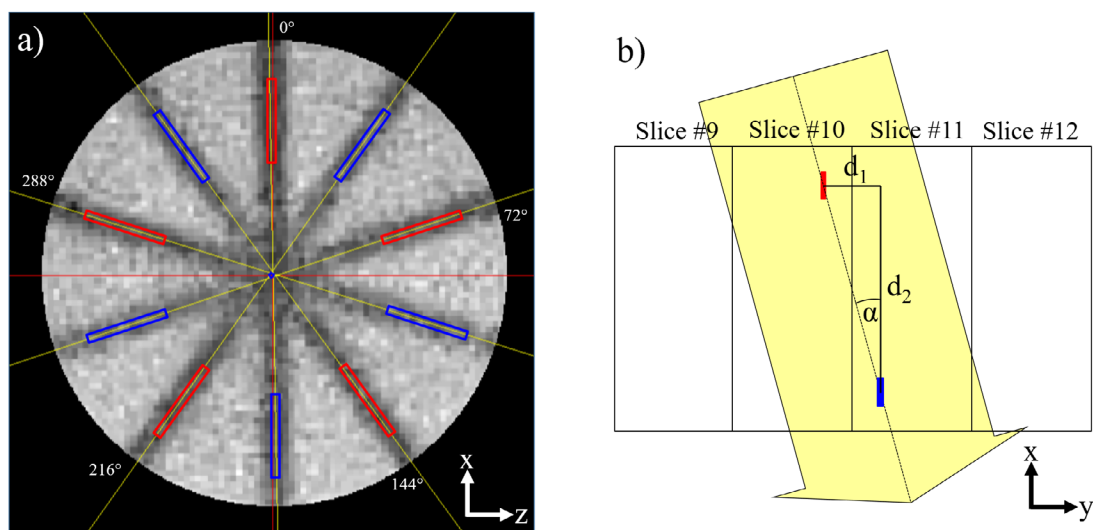


Figure 2. (a) Transversal slice (#10) of the measurements with 32 signal averages with the visible star shot in the PG and the reconstructed beam axes (yellow lines) by the Mephisto tool. The profiles for the entering and exiting beams are averaged over the red and blue areas, respectively. (b) Schematic representation of a sagittal slice including 4 axial slices (#9-#12). The axial position difference of entry and exit area, d_1 and d_2 and the inclination angle α can be determined.

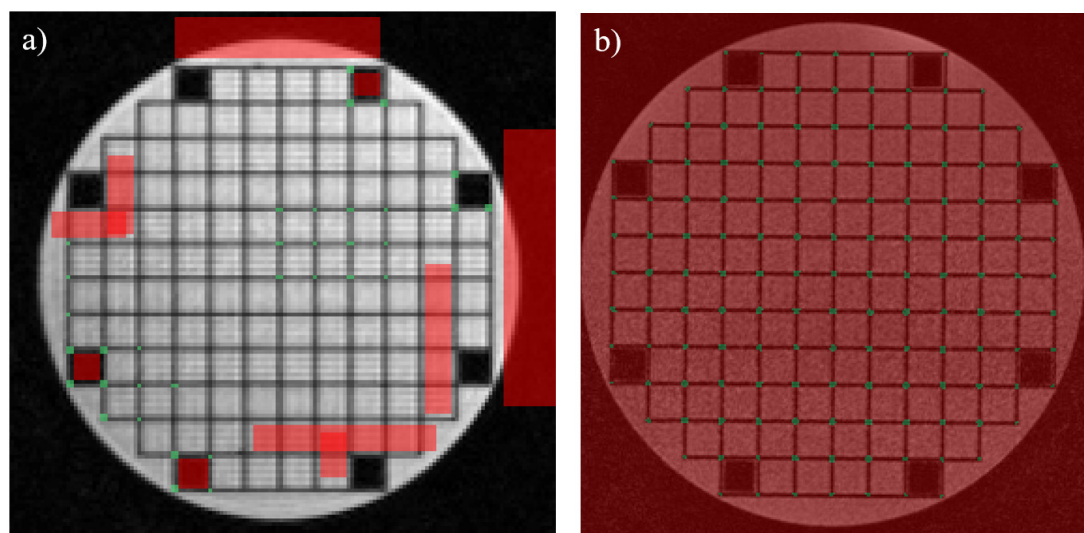


Figure 3. (a) The two different Weka Segmentation classes are indicated in green (control point) and red (no control point) to train the classifier. (b) Fully segmented image of one representative slice with all grid intersections detected (green). Within the green areas, a center of mass-analysis is performed to determine the final control point position.

Table 1. 1D Distance (mean \pm SEM) of the beam center for each beam in axial direction averaged over the profiles ($n = 15$) in the areas shown in figure 2(a) (for NSA of 12, 24 and 32) relative to the position of the imaging isocenter. Additionally, the average distance over all beams and both areas (entry and exit) \pm the total uncertainty (statistical error plus positioning uncertainty) is displayed.

	$n = 15$	0° [mm]	72° [mm]	144° [mm]	216° [mm]	288° [mm]	Mean [mm]
12 averages	Entry	0.3 ± 0.2	0.5 ± 0.2	0.2 ± 0.3	0.4 ± 0.3	0.6 ± 0.3	0.4 ± 0.6
	Exit	0.6 ± 0.2	0.0 ± 0.3	1.1 ± 0.3	-0.4 ± 0.2	0.7 ± 0.3	
24 averages	Entry	0.2 ± 0.1	0.1 ± 0.2	0.9 ± 0.2	0.2 ± 0.2	0.3 ± 0.2	0.3 ± 0.5
	Exit	0.3 ± 0.2	0.7 ± 0.2	0.2 ± 0.3	-0.2 ± 0.2	0.7 ± 0.3	
32 averages	Entry	0.2 ± 0.1	0.1 ± 0.1	0.4 ± 0.1	-0.1 ± 0.2	0.7 ± 0.2	0.3 ± 0.5
	Exit	0.5 ± 0.1	0.2 ± 0.2	0.7 ± 0.2	-0.2 ± 0.2	0.5 ± 0.2	

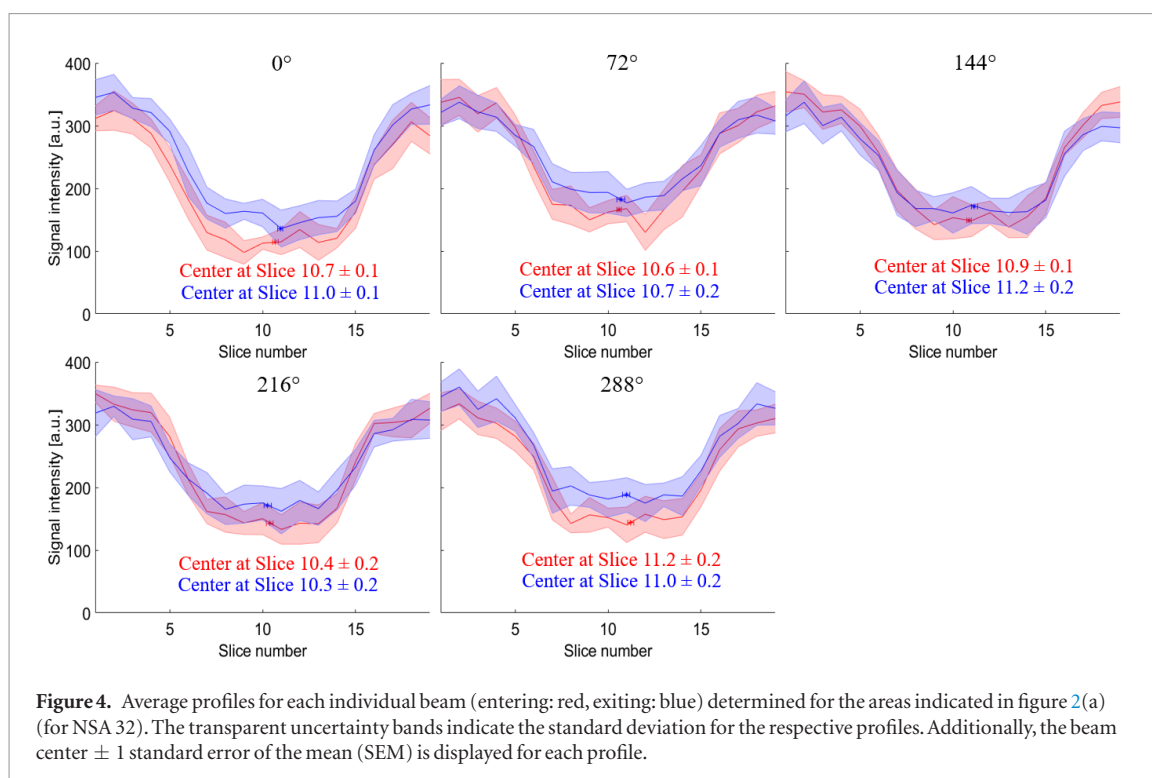


Table 2. 2D distance of isocircle center to the imaging isocenter (IC_d) and isocircle radius (IC_r) for the images close to the axial isocenter position (table 1). Additionally, the average over all slices \pm the total uncertainty (statistical error plus positioning uncertainty) is displayed.

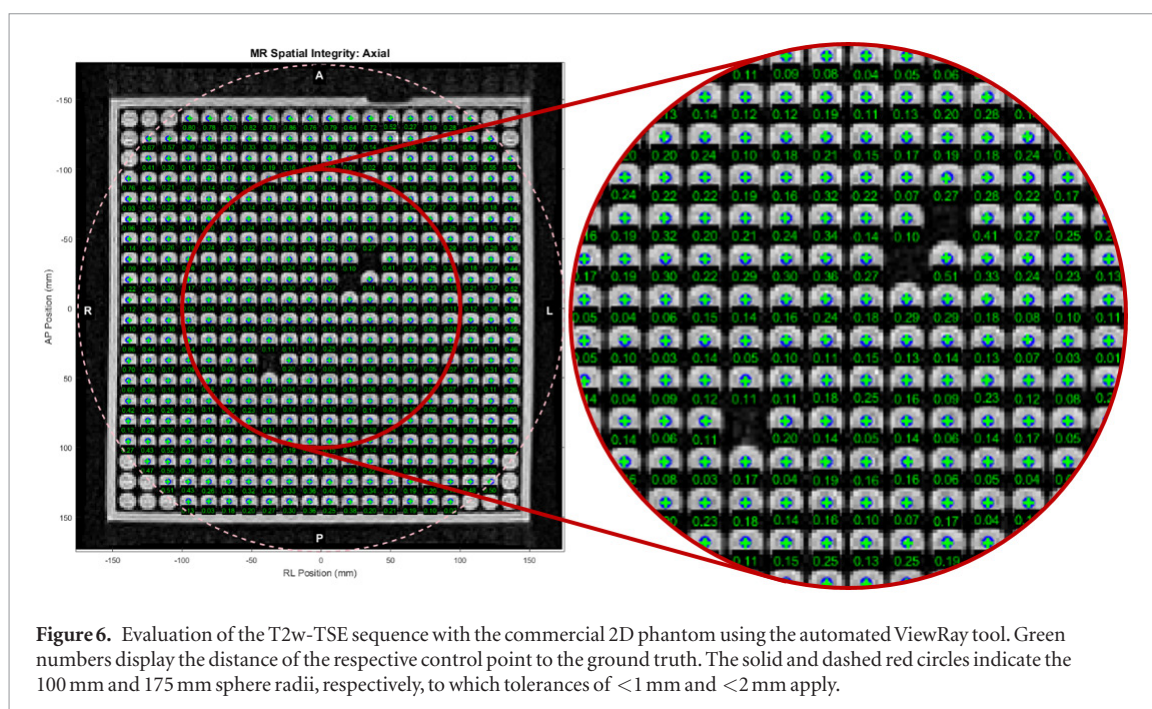
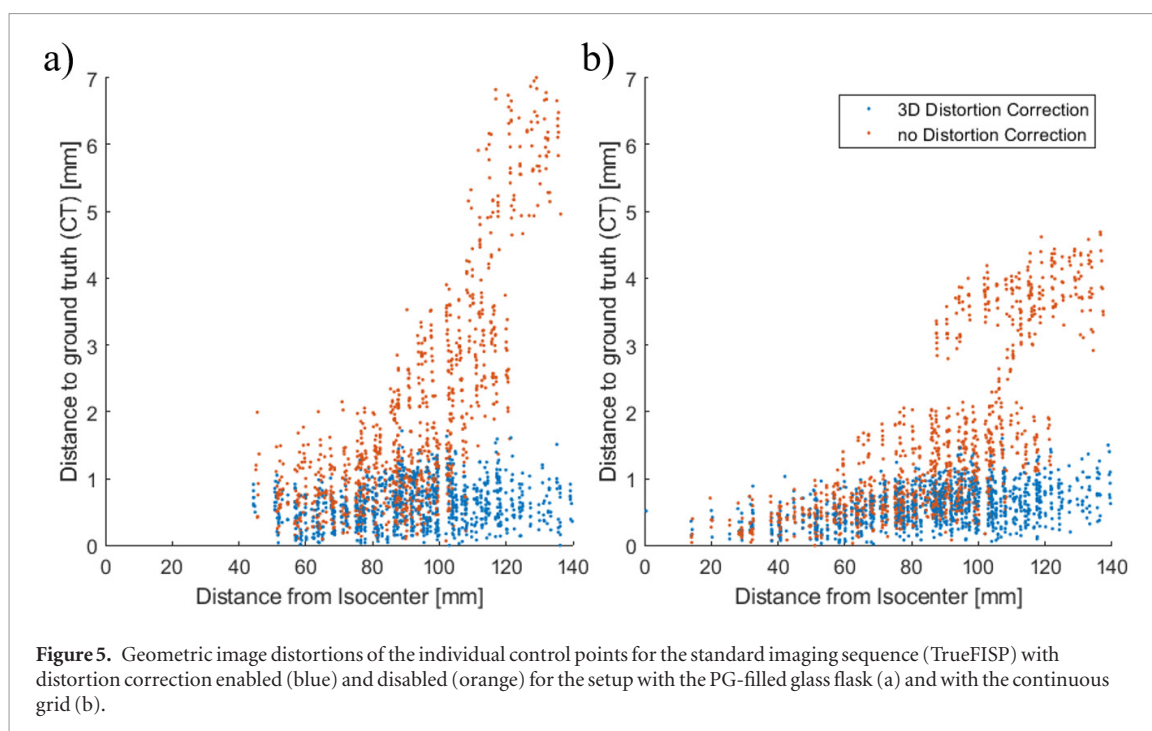
	Averages	Slice 9 [mm]	Slice 10 [mm]	Slice 11 [mm]	Slice 12 [mm]	Mean [mm]
IC_d	12	0.2	0.4	0.3	0.5	0.4 ± 0.6
	24	0.7	1.2	0.9	0.8	0.9 ± 0.4
	32	0.8	0.2	0.9	0.8	0.7 ± 0.4
IC_r	12	0.3	0.4	0.3	0.6	0.4 ± 0.1
	24	0.4	0.6	0.4	0.5	0.5 ± 0.1
	32	0.5	0.4	0.6	0.5	0.5 ± 0.2

and imaging isocenter in axial direction (y -direction) was found to be (0.4 ± 0.3) mm, (0.3 ± 0.2) mm and (0.3 ± 0.2) mm for 12, 24 and 32 NSA, respectively (mean \pm standard error of the mean (SEM)).

The isocenter position in the transversal plane was evaluated for the slices closest to the previously determined axial isocenter position and the average distances from the imaging isocenter, (IC_d), are displayed in table 2. Table 2 additionally shows the isocircle radius, (IC_r). Accounting for a positioning uncertainty of the phantom of ± 0.5 mm (one third of a voxel size) in each direction and applying quadratic error propagation results in a 3D shift between irradiation and imaging isocenter of (0.6 ± 0.9) mm, (0.9 ± 0.9) mm, and (0.8 ± 0.9) mm for 12, 24, and 32 NSA, respectively. The comparison of the axial positions determined for the entry and exit part of the beams using the data for the 32 averages (highest SNR) revealed inclinations of $(-0.24 \pm 0.24)^\circ$, $(-0.12 \pm 0.32)^\circ$, $(-0.37 \pm 0.27)^\circ$, $(0.19 \pm 0.25)^\circ$ and $(-0.24 \pm 0.35)^\circ$ for gantry angles of 0° , 72° , 144° , 216° and 288° , respectively.

3.2. Geometric distortions

The geometric image distortions evaluated for the standard imaging sequence with and without distortion correction for the simultaneous and sequential measurements are shown in figures 5(a) and (b). The tolerances recommended by the manufacturer of <1 mm for all control points within a sphere of 100 mm radius and <2 mm for 90% control points within 175 mm radius around the isocenter, were exceeded by a few points for the setup with the PG-filled glass flask inside of the phantom. With distortion correction, the passing rate was 87.7% for the first criterion and 100% for the second one. The respective overall mean distortion was (0.62 ± 0.32) mm with a maximum distortion of 1.72 mm. Without distortion correction, the passing rates were 59.8% and 68.9%, respectively. The respective overall mean distortion was (1.93 ± 1.61) mm within a 140 mm sphere with a maximum distortion of 7.32 mm.



For the continuously grid inserts with distortion correction the passing rate was 95.0% for the first criterion and 100% for the second one. The respective overall mean distortion was (0.60 ± 0.28) mm with a maximum distortion of 1.6 mm and 99.8% of the control points had distortions below 1.5 mm. Without distortion correction, the passing rates were 69.5% and 77.2%, respectively. The respective overall mean distortion was (1.50 ± 1.56) mm within a 140 mm sphere with a maximum distortion of 4.9 mm.

The measurements with the commercial phantom met both tolerance criteria of the manufacturer (figure 6) for all orientations of the phantom. The overall mean distortion was (0.57 ± 0.25) mm with a maximum distortion of 1.35 mm.

The mean distortions of the T2w-TSE sequence used for PG evaluation within a single plane in the setup with the inserted PG container was (0.59 ± 0.28) mm with maximum distortion of 1.4 mm. 91% and 100% of the control points fulfilled the first and the second tolerance criterion, respectively. The mean distortions of the inner part was determined with the continuous grid structure to (0.55 ± 0.19) mm with maximum distortion of 0.8 mm. Measuring the T2w-TSE sequence with the commercial 2D phantom and evaluation with the ViewRay

software tool revealed mean distortions of (0.32 ± 0.23) mm and pass rates of 100% for both tolerance criteria (figure 6).

4. Discussion

This study demonstrated the feasibility of a polymer gel-based isocenter alignment measurement in 3D at a 0.35 T MR-Linac. According to the manufacturer's recommended workflow, this is currently achieved by the following procedure: first, the laser/radiation isocenter coincidence has to be established by separately checking the isocenter position in the xy - and xz -plane by a film or ionization chamber array measurements. Then, the lasers have to be adjusted to the measured irradiation isocenter as good as possible, and finally an MR scan of a cylindrical phantom positioned exactly by means of the lasers has to be performed. In contrast, the method presented here is not relying on the laser system as the required accurate positioning of the phantom is achieved directly by the MR-images. In principle, accurate positioning of the phantom is not necessarily required for isocenter accuracy measurements, if the actual irradiation isocenter is visualized directly in the MR-image. However, as the star shot was evaluated in the separate Mephisto-Software rather than the MR-console, where the imaging isocenter is known, the nominal isocenter position in the phantom had to be reconstructed by means of the wedge-fiducials. To assure that this point is actually located at the nominal irradiation isocenter of the MR-Linac, accurate positioning is necessary. This type of nominal irradiation isocenter reconstruction is also a standard procedure when using films.

The other commercially available System (Elekta Unity, Elekta AB, Stockholm, Schweden) uses a different solution to check the isocenter accuracy. As this system is additionally equipped with an electronic portal imaging device (EPID), a phantom with seven ZrO_2 spheres, which are visible on the EPID, is used (Hanson *et al* 2019). This method offers a high accuracy, however, due to the lack of an EPID-device, it is not applicable at the MRIdian system.

The gel evaluation was performed with the same device immediately after irradiation employing a T2w-TSE sequence with an isotropic resolution of 1 mm^3 in 3D. In addition, image distortions were measured up to a distance of 140 mm from the isocenter. This can be achieved by a single measurement with a newly developed phantom.

No significant difference for the central position of each of the five individual beams was determined for different NSA (table 1), however the measurement with lower NSA showed a slightly higher uncertainty due to a lower SNR. It is known that the polymerization of the gel continues up to 48 h after irradiation leading to an increased signal. Although this would not improve the SNR itself, an improved contrast-to-noise ratio (CNR) can be expected over this time period. In principle, this offers the possibility to improve the beam center determination. This, however, was not performed in the present study as we aimed to evaluate the measurement directly after the measurement without repositioning the phantom at the MR-Linac.

The accuracy of the irradiation isocenter in the transversal plane (table 2) revealed no significant difference between NSA of 12, 24 and 32 in terms of the radius of the isocircle (IC_r). In addition, the tolerance limit of 0.5 mm for a star-shot measurement as recommended by the report of Task Group 142 (Klein *et al* 2009) was met for the average over all evaluated image slices of all NSA. Exceeding this tolerance limit normally indicates a misalignment or instability of the gantry, however, in presence of a magnetic field, an increase of IC_r is expected as the Lorentz-force systematically deflects the secondary electrons to the same direction with respect to the beam axis. This results in asymmetric beam profiles with a laterally shifted maximum (Raaijmakers *et al* 2008) leading to an increased IC_r -value (van Zijp *et al* 2016, Dorsch *et al* 2018). Without compensating the effect of the magnetic field, e.g. by using high-density materials (van Zijp *et al* 2016), an increased isocircle radius is therefore not solely an indication of machine inaccuracies. However, for equiangular distributed beams, the profile shift of each beam induced by the magnetic field is the same and therefore also the center of the isocircle can be expected to be independent of the magnetic field. Thus, this point can be used to define the actual irradiation isocenter. Its distance to the imaging isocenter (IC_d) is an important alignment parameter and the mean values for IC_d were < 1 mm for all measurements.

Also the 3D-shift between irradiation and imaging isocenter resulting from the combined radial and axial shifts, was < 1 mm for all NSA, however with an increased uncertainty. This increased uncertainty is dominated by the image-based positioning uncertainty of the phantom, which is estimated to be ~ 0.5 mm (a third of a voxel size) in each direction.

To determine potential inclinations of the beams relative to the transversal plane, the beams were separated into entry and exit areas (figure 2(a), red and blue boxes). It was found that these areas differ slightly in their axial beam center position, however, the deviations are still within the experimental uncertainties. No significant tilt of the beams against the transversal plane could be detected.

All values shown here (IC_r , IC_d and inclination angles) could be reproduced in further independent measurements within the uncertainty limits. Furthermore, no significant geometric differences for IC_r and IC_d between

a single contrast T2w-TSE and a quantitative T2 acquisition (Dorsch *et al* 2019) were identified. However, in this study the slice thickness of the single contrast measurement could be reduced from 20 mm to 1 mm, which resulted in a significantly better resolution in the y -direction. Finally, the T2w-TSE used in this work provides seven-fold higher SNR within a comparable acquisition time. However, as the TSE is a research sequence, it is not yet available to the general user of the MRIdian system.

The distortion measurements using the newly developed phantom without distortion correction clearly showed the necessity of the correction. While spatial errors of up to 7.32 mm may occur without correction, they were reduced to values <1.72 mm within 140 mm and <1.7 mm within 100 mm distance from the isocenter when the correction was applied. In contrast to the commercial phantom, where the recommendations of ViewRay were met for all phantom orientations, some points exceeded these tolerances when using the developed phantom. This could originate from the fact that the control points in our phantom contained significantly less pixels leading to a larger variability of the positions. While up to 70 pixels were used in the commercial phantom to determine the center of mass of one control point, the grid intersections of our phantom was segmented by only 1–9 pixel. Therefore falsely segmented pixels have a higher impact on the center of mass position. It has to be noted, however, that we measured the distortions in 3D while the commercial phantom provides only 2D distortions. This may also contribute to the slightly larger distortions measured with our phantom. A further advantage of our phantom is that a single measurement is sufficient to measure the distortions in all three directions while the commercial 2D phantom requires 7 independent measurements with different phantom orientations.

In general, the isocenter accuracy measurement presented in this study may also be affected by image distortions. With the phantom equipped with the combination of gel container and grid, distortions within radial distances between 44.5 mm and 140 mm can be measured, covering the size, e.g. of head and neck treatment areas. This disregards the isocenter region, where distortions are expected to be smaller. To verify this assumption, the phantom was also equipped with a continuous grid covering radial distances of up to 140 mm including the isocenter region. It could be shown that the distortions of 85% of the control points in the region of the PG container were below 0.55 mm confirming the underlying assumption of the simultaneous isocenter accuracy and image distortion measurement.

Nevertheless, the distortion may be significant at the position of the wedges used to setup the phantom. However, as the wedges are located within the main planes of the phantom symmetrically to its center and since the wedges are also aligned to the main planes of the MR-Linac symmetrically to the isocenter, the distortions at opposing wedge locations are likely to point in radial but opposite directions. As a result, the effects of distortions at opposing wedge locations are expected to largely compensate each other leading to a small impact on the determination of the isocenter position. For this study this was confirmed by the distortion map. Also B0-inhomogeneities due to susceptibility jumps in the region of the PG were found to be negligible (average in the order of 10 Hz). Solely in the immediate border of the glass flask shifts of up to 60 Hz were detected. The use of either simultaneous or sequential measurement of isocenter accuracy and image distortions with the new phantom may then be used based on the size and long-term stability of the distortions near the isocenter. For larger anatomical regions (e.g. abdomen or pelvis), it is likely that the anatomical structures relevant for registration purpose in adaptive procedures are still located within the presented distance to the isocenter. If this is not the case, distortions have to be checked with larger phantoms.

5. Conclusion

This study investigated the alignment of irradiation and imaging isocenter of a 0.35 T MRI-Linac as well as the spatial distribution of MR-image distortions in a single measurement using a newly developed phantom. The method was evaluated at the MR-unit of the MR-Linac immediately after irradiation using an isotropic spatial image resolution of 1 mm. Isocenter accuracy was found to be (0.6 ± 0.9) mm, (0.9 ± 0.9) mm and (0.8 ± 0.9) mm for 12, 24 and 32 NSA, respectively. After 3D correction, image distortion was significantly reduced and showed a mean distortion of (0.60 ± 0.28) mm and distortions below 1.5 mm for 99.82% of the evaluated control points with a distance of 140 mm. These geometrical uncertainties have to be considered by additional safety margins.

Acknowledgments

This work has received funding from the EMPIR programme co-financed by the Participating States and from the European Union's Horizon 2020 research and innovation programme. Additionally, the authors would like to thank Professor Dr K Kopka for providing the lab space for the production of the polymer gel. We also like to thank Philipp Hanslovsky for providing valuable input for the automated grid detection procedure. The Department of Radiation Oncology, University Hospital Heidelberg, has a research collaboration agreement with ViewRay Inc.

ORCID iDs

S Dorsch  <https://orcid.org/0000-0002-8185-8644>

P Mann  <https://orcid.org/0000-0002-2857-4861>

A Elter  <https://orcid.org/0000-0002-0295-9931>

References

- Adamovics J and Maryanski M J 2006 Characterisation of PRESAGE™: a new 3D radiochromic solid polymer dosimeter for ionising radiation *Radiat. Prot. Dosimetry* **120** 107–12
- Adamson J, Carroll J, Trager M, Yoon S W, Kodra J, Maynard E, Hilts M, Oldham M and Jirasek A 2019 Delivered dose distribution visualized directly with onboard kV-CBCT: proof of principle *Int. J. Radiat. Oncol.* **103** 1271–9
- American Association of Physicists in Medicine 2010 Acceptance testing and quality assurance procedures for magnetic resonance imaging facilities *AAPM Report* No. 100, American Association of Physicists in Medicine
- American College Of Radiology 2005 *Phantom Test Guidance for the ACR MRI Accreditation Program* (Reston, VA: American College of Radiology)
- Baldock C, De Deene Y, Doran S, Ibbott G, Jirasek A, Lepage M, McAuley K B, Oldham M and Schreiner L J 2010 Polymer gel dosimetry *Phys. Med. Biol.* **55** R1–63
- Baldwin L L N, Wachowicz K, Thomas S D S, Rivest R and Fallone B G 2007 Characterization, prediction, and correction of geometric distortion in 3 T MR images *Med. Phys.* **34** 388
- Bieri O and Scheffler K 2013 Fundamentals of balanced steady state free precession MRI *J. Magn. Reson. Imaging* **38** 2–11
- Brown S, Venning A, De Deene Y, Vial P, Oliver L, Adamovics J and Baldock C 2008 Radiological properties of the PRESAGE and PAGAT polymer dosimeters *Appl. Radiat. Isot.* **66** 1970–4
- Costa F, Doran S J, Hanson I M, Nill S, Billas I, Shipley D, Duane S, Adamovics J and Oelfke U 2018 Investigating the effect of a magnetic field on dose distributions at phantom-air interfaces using PRESAGE® 3D dosimeter and Monte Carlo simulations *Phys. Med. Biol.* **63** 05NT01
- De Deene Y, De Wagter C, Van Duyse B, Derycke S, De Neve W and Achten E 1998 Three-dimensional dosimetry using polymer gel and magnetic resonance imaging applied to the verification of conformal radiation therapy in head-and-neck cancer *Radiother. Oncol.* **48** 283–91
- De Deene Y, Hurley C, Venning A, Vergote K, Mather M, Healy B J and Baldock C 2002 A basic study of some normoxic polymer gel dosimeters *Phys. Med. Biol.* **47** 3441–63
- De Deene Y, Vergote K, Claeys C and De Wagter C 2006 The fundamental radiation properties of normoxic polymer gel dosimeters: a comparison between a methacrylic acid based gel and acrylamide based gels *Phys. Med. Biol.* **51** 653–73
- Dietrich O, Raya J G, Reeder S B, Reiser M F and Schoenberg S O 2007 Measurement of signal-to-noise ratios in MR images: influence of multichannel coils, parallel imaging, and reconstruction filters *J. Magn. Reson. Imaging* **26** 375–85
- Doran S J, Charles-Edwards L, Reinsberg S A and Leach M O 2005 A complete distortion correction for MR images: I. Gradient warp correction *Phys. Med. Biol.* **50** 1343–61
- Dorsch S, Mann P, Elter A, Runz A, Klüter S and Karger C P 2019 Polymer gel-based measurements of the isocenter accuracy in an MR-LINAC *J. Phys.: Conf. Ser.* **1305** 012007
- Dorsch S, Mann P, Lang C, Haering P, Runz A and Karger C P 2018 Feasibility of polymer gel-based measurements of radiation isocenter accuracy in magnetic fields *Phys. Med. Biol.* **63** 11NT02
- Fallone B G, Murray B, Rathee S, Stanescu T, Steciw S, Vidakovic S, Blosser E and Tymofichuk D 2009 First MR images obtained during megavoltage photon irradiation from a prototype integrated linac-MR system *Med. Phys.* **36** 2084–8
- Ginn J S, Agazaryan N, Cao M, Baharom U, Low D A, Yang Y, Gao Y, Hu P, Lee P and Lamb J M 2017 Characterization of spatial distortion in a 0.35 T MRI-guided radiotherapy system *Phys. Med. Biol.* **62** 4525–40
- Green O L et al 2018 First clinical implementation of real-time, real anatomy tracking and radiation beam control *Med. Phys.* **45** 3728–40
- Hanson I M, Nill S, Chick J and Oelke U 2019 Linac commissioning methodology for the Elekta Unity MR Linac (Milano: ESTRO38: PO-1035) Poster presentation ([https://doi.org/10.1016/S0167-8140\(19\)31455-0](https://doi.org/10.1016/S0167-8140(19)31455-0))
- Heerkens H D, Van Vulpen M, Van Den Berg C A T, Tijssen R H N, Crijns S P M, Molenaar I Q, Van Santvoort H C, Reerink O and Meijer G J 2014 MRI-based tumor motion characterization and gating schemes for radiation therapy of pancreatic cancer *Radiother. Oncol.* **111** 252–7
- Hilts M, Audet C, Duzenli C and Jirasek A 2000 Polymer gel dosimetry using x-ray computed tomography: a feasibility study *Phys. Med. Biol.* **45** 2559–71
- International Electrotechnical Commission 2011 *IEC 61217: Radiotherapy equipment—coordinates, movements and scales Document Number IEC 61217 Ed. 2.0* (International Electrotechnical Commission)
- Jaffray D A, Siewerdsen J H, Wong J W and Martinez A A 2002 Flat-panel cone-beam computed tomography for image-guided radiation therapy *Int. J. Radiat. Oncol.* **53** 1337–49
- Janke A, Zhao H, Cowin G J, Galloway G J and Doddrell D M 2004 Use of spherical harmonic deconvolution methods to compensate for nonlinear gradient effects on MRI images *Magn. Reson. Med.* **52** 115–22
- Keall P J, Barton M and Crozier S 2014 The Australian magnetic resonance imaging–linac program *Semin. Radiat. Oncol.* **24** 203–6
- Klein E E et al 2009 Task Group 142 report: Quality assurance of medical accelerators *Med. Phys.* **36** 4197–212
- Klüter S 2019 Technical design and concept of a 0.35 T MR-Linac *Clin. Transl. Radiat. Oncol.* **18** 98–101
- Kontaxis C, Bol G H, Stemkens B, Glitzner M, Prins F M, Kerkmeijer L G W, Legendijk J J W and Raaymakers B W 2017 Towards fast online intrafraction replanning for free-breathing stereotactic body radiation therapy with the MR-linac *Phys. Med. Biol.* **62** 7233–48
- Kubo H D, Hill B C, Med P, Neicu T, Shirato H, Burk L M, Lee Y Z and Matthew J 1996 Respiration gated radiotherapy treatment: a technical study *Phys. Med. Biol.* **41** 83
- Legendijk J J W et al 2008 MRI/linac integration *Radiother. Oncol.* **86** 25–9
- Lee H J, Roed Y, Venkataraman S, Carroll M and Ibbott G S 2017 Investigation of magnetic field effects on the dose–response of 3D dosimeters for magnetic resonance – image guided radiation therapy applications *Radiother. Oncol.* **125** 426–32
- Lutz W, Winston K R and Maleki N 1988 A system for stereotactic radiosurgery with a linear accelerator *Int. J. Radiat. Oncol. Biol. Phys.* **14** 373–81

- Mann P, Witte M, Moser T, Lang C, Runz A, Johnen W, Berger M, Biederer J and Karger C P 2017 3D dosimetric validation of motion compensation concepts in radiotherapy using an anthropomorphic dynamic lung phantom *Phys. Med. Biol.* **62** 573–95
- Martinez A A, Yan D, Lockman D, Brabbins D, Kota K, Sharpe M, Jaffray D A, Vicini F and Wong J 2001 Improvement in dose escalation using the process of adaptive radiotherapy combined with three-dimensional conformal or intensity-modulated beams for prostate cancer *Int. J. Radiat. Oncol.* **50** 1226–34
- Mutic S and Dempsey J F 2014 The ViewRay system: magnetic resonance-guided and controlled radiotherapy *Semin. Radiat. Oncol.* **24** 196–9
- National Electrical Manufacturers Association 2001 Determination of signal-to-noise ratio (SNR) in diagnostic magnetic resonance imaging *NEMA Standards Publication MS 1-2001* NEMA
- Raaijmakers A J E, Raaymakers B W and Lagendijk J J W 2008 Magnetic-field-induced dose effects in MR-guided radiotherapy systems: dependence on the magnetic field strength *Phys. Med. Biol.* **53** 909–23
- Reinsberg S A, Doran S J, Charles-Edwards E M and Leach M O 2005 A complete distortion correction for MR images: II. Rectification of static-field inhomogeneities by similarity-based profile mapping *Phys. Med. Biol.* **50** 2651–61
- Reiser M F, Semmler W and Hricak H 2008 *Magnetic Resonance Tomography* (Berlin: Springer-Verlag)
- Schad L R, Ehrlicke H-H, Wowra B, Layer G, Engenhart R, Kauczor H-U, Zabel H-J, Brix G and Lorenz W J 1992 Correction of spatial distortion in magnetic resonance angiography for radiosurgical treatment planning of cerebral arteriovenous malformations *Magn. Reson. Imaging* **10** 609–21
- Schneider E and Glover G 1991 Rapid *in vivo* proton shimming *Magn. Reson. Med.* **18** 335–47
- Stanescu T, Jans H S, Wachowicz K and Gino Fallone B 2010 Investigation of a 3D system distortion correction method for MR images *J. Appl. Clin. Med. Phys.* **11** 200–16
- Tadic T, Jaffray D A and Stanescu T 2014 Harmonic analysis for the characterization and correction of geometric distortion in MRI *Med. Phys.* **41** 112303
- Thomas A, Niebanck M, Juang T, Wang Z and Oldham M 2013 A comprehensive investigation of the accuracy and reproducibility of a multitarget single isocenter VMAT radiosurgery technique *Med. Phys.* **40** 121725
- Treuer H, Hoevens M, Luyken K, Gierich A, Kocher M, Muller R-P and Sturm V 2000 On isocentre adjustment and quality control in linear accelerator based radiosurgery with circular collimators and room lasers *Phys. Med. Biol.* **45** 2331–42
- van Zijp H M, van Asselen B, Wolthaus J W H, Kok J M G, de Vries J H W, Ishakoglu K, Beld E, Lagendijk J J W and Raaymakers B W 2016 Minimizing the magnetic field effect in MR-linac specific QA-tests: the use of electron dense materials *Phys. Med. Biol.* **61** N50–9
- Vandecasteele J and De Deene Y 2013 On the validity of 3D polymer gel dosimetry: II. Physico-chemical effects *Phys. Med. Biol.* **58** 19–42
- Venning a J, Hill B, Brindha S, Healy B J and Baldock C 2005 Investigation of the PAGAT polymer gel dosimeter using magnetic resonance imaging *Phys. Med. Biol.* **50** 3875–88
- Wang D, Doddrell D M and Cowin G 2004a A novel phantom and method for comprehensive 3-dimensional measurement and correction of geometric distortion in magnetic resonance imaging *Magn. Reson. Imaging* **22** 529–42
- Wang D, Strugnell W, Cowin G, Doddrell D M and Slaughter R 2004b Geometric distortion in clinical MRI systems: Part II: correction using a 3D phantom *Magn. Reson. Imaging* **22** 1223–32
- Webb P and Macovski A 1991 Rapid, fully automatic, arbitrary-volume *in vivo* shimming *Magn. Reson. Med.* **20** 113–22
- Yan Y et al 2018 A methodology to investigate the impact of image distortions on the radiation dose when using magnetic resonance images for planning *Phys. Med. Biol.* **63** 085005

2.5 Publication IV

COMPATIBILITY OF 3D PRINTING MATERIALS AND PRINTING TECHNIQUES WITH PAGAT GEL DOSIMETRY

Authors: Elter A, Dorsch S, Mann P, Runz A, Johnen W and Karger C P

Journal reference: *Physics in Medicine & Biology*, **64** (2019) 04NT02 (7pp)

DOI: 10.1088/1361-6560/aafef0

Copyright notice: Open access, CC BY license which permits reuse for any purposes

Authors' contribution: First author of this work, was our master student Alina Elter. This work investigates the compatibility of several 3D printing materials and methods with the PAGAT PG. Having identified a combination of a 3D printing material and printing technique, which is compatible with the PG, the design of arbitrarily-shaped gel containers became feasible. This is a very important step towards the creation of anthropomorphic phantoms to perform end-to-end tests for new treatment workflows including 3D dose verification. My contributions as second author consisted in the assistance of the experimental execution, covering the preparation of the PG, the irradiation and MR evaluation, the data analysis as well as the interpretation of the results. In addition, I was significantly involved in the preparation of the manuscript and in the revision process.

OPEN ACCESS



NOTE

Compatibility of 3D printing materials and printing techniques with PAGAT gel dosimetry

RECEIVED
8 October 2018REVISED
24 December 2018ACCEPTED FOR PUBLICATION
16 January 2019PUBLISHED
8 February 2019

Original content from this work may be used under the terms of the [Creative Commons Attribution 3.0 licence](https://creativecommons.org/licenses/by/3.0/).

Any further distribution of this work must maintain attribution to the author(s) and the title of the work, journal citation and DOI.

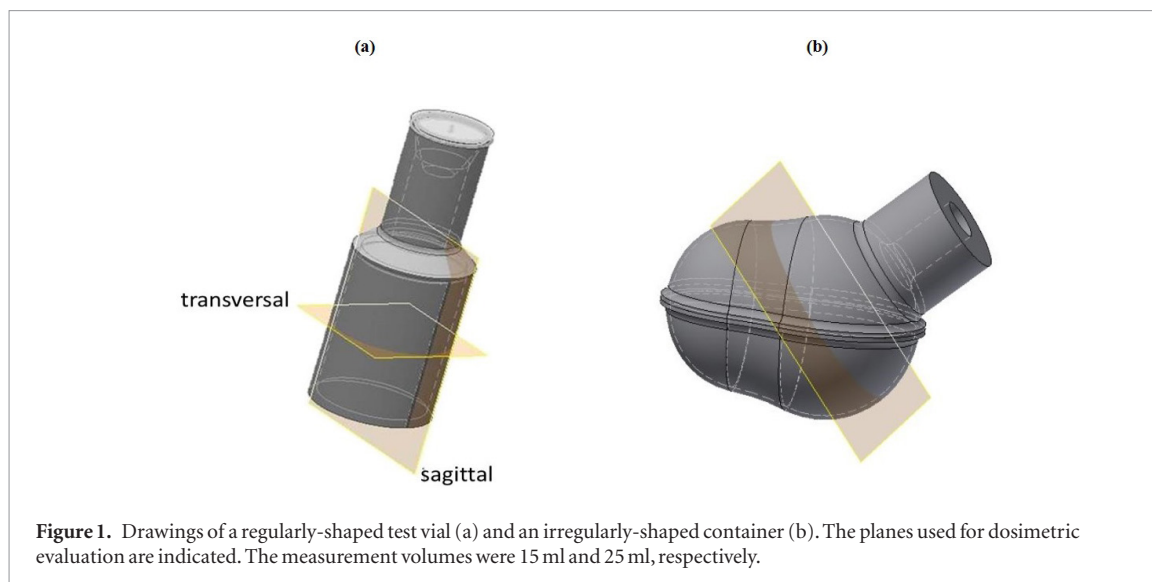
A Elter^{1,2,3}, S Dorsch^{1,2,3}, P Mann^{1,3}, A Runz^{1,3}, W Johnen^{1,3} and C P Karger^{1,3}¹ Department of Medical Physics in Radiation Oncology, German Cancer Research Center (DKFZ), INF 280, 69120 Heidelberg, Germany² Faculty of Physics and Astronomy, University of Heidelberg, Heidelberg, Germany³ National Center for Radiation Research in Oncology (NCRO), Heidelberg Institute for Radiation Oncology (HIRO), Heidelberg, GermanyE-mail: a.elter@dkfz.de**Keywords:** polymer gel dosimetry, 3D dose verification, 3D printed phantom, PAGAT gel**Abstract**

Polymer gel (PG) dosimetry enables three dimensional (3D) measurement of complex dose distributions. However, PGs are strongly reactive with oxygen and other contaminations, limiting their applicability by the need to use specific container materials. We investigate different 3D printing materials and printing techniques for their compatibility with PG. Suitable 3D printing materials may provide the possibility to perform PG dosimetry in complex-shaped phantoms. 3D printed and PG-filled test vials were irradiated homogeneously. The signal response was evaluated with respect to homogeneity and compared to the signal in already validated reference vials. In addition, for the printing material VeroClear™ (StrataSys, Eden Prairie, USA) different methods to remove support material, which was required during the printing process, were investigated. We found that the support material should be used only on the outer side of the container wall with no direct contact to the PG. With the VeroClear™ material a homogeneous signal response was achieved with a mean deviation of $(-1.4 \pm 0.6)\%$ relative to the reference vials. In addition, the homogeneous irradiation of an irregularly-shaped gel container designed with the same printing material and technique also lead to a homogeneous PG response. Furthermore, a small field irradiation of an additional test-vial showed an accurate representation of steep dose gradients with a deviation of the maximum position of $< 1\text{mm}$ relative to the reference vial.

1. Introduction

In patient specific quality assurance (QA) for radiotherapy, it is of high interest to perform three-dimensional (3D) measurements of the dose distribution (Guo *et al* 2006, Doran 2009, Seco *et al* 2014, Low 2015). Besides using electronic dosimeter arrays, polymer gel (PG) dosimetry may be used to measure complex 3D dose distributions (De Deene *et al* 2006, Baldock *et al* 2010, De Deene and Vandecasteele 2013, Vandecasteele and De Deene 2013). PGs use radiation sensitive chemicals, which polymerize after irradiation as a function of absorbed radiation dose (Baldock *et al* 2010). This effect can be evaluated with magnetic resonance imaging (MRI) as the polymerization alters the relaxation rate R_2 of the transversal magnetization. PG dosimetry exhibits a high spatial resolution enabling measurements in steep dose gradients as they occur e.g. in intensity-modulated radiation therapy (IMRT) (Sandilos *et al* 2004, Vergote *et al* 2004). In addition, PG has radiation absorption properties equivalent to soft tissues (Baldock *et al* 2010, Schreiner 2015). However, PG handling is quite challenging as it is strongly reactive with oxygen and other contaminations (De Deene *et al* 2006), which limits its use in combination with common phantom materials. Yet, mostly glass and BAREX™, a thermoformable acrylonitrile-methyl acrylate copolymer with low oxygen permeability (Vergote *et al* 2004), are used as container materials (De Deene and Vandecasteele 2013). However, using these materials, the available container sizes and shapes are limited.

In this study, we investigate 3D printing materials and different printing techniques for their compatibility with PG. Using 3D printing would allow for designing new phantoms and to perform 3D dose measurements in



arbitrary geometries. This may be of great advantage to test new radiotherapy treatment techniques (Schreiner 2015, Kamomae *et al* 2017, Oh *et al* 2017, Yea *et al* 2017).

2. Materials and methods

2.1. Polymer gel

In this study, the PAGAT-(PolyAcrylamide Gelatin gel fabricated at ATmospheric conditions) PG was used as it can be produced in-house at low costs, under atmospheric conditions and has a small dose rate dependence (De Deene *et al* 2006). The gel consists of a gelatin matrix (6% w/w Gelatin, 300 bloom, SIGMA Aldrich), enriched with two different monomers (2, 5% w/w acrylamide and 2, 5% w/w N,N'-methylene-bis-acrylamide) as active components. Due to the high reactivity of the gel with oxygen the gel was flushed with nitrogen for 5 min to reduce the amount of dissolved oxygen in the gel (De Deene *et al* 2002). Directly afterwards, 5 mM bis[tetrakis(hydroxymethyl)phosphonium] chloride (THPC) was added as an antioxidant to further reduce interactions with oxygen. After production, the PG was filled into small vials made of different materials (see section 2.2). Before filling, the vials were flushed with nitrogen, and were sealed with Parafilm 'M' Laboratory film (Bemis, Neenah, USA) afterwards to reduce the influence of penetrating oxygen. Additionally, the vials were enwrapped in aluminum foil to protect the gel from light (Koeva *et al* 2009), placed in a desiccator, which was flushed with nitrogen for 10 min and stored in a refrigerator at 4°C for 20 – 24 h. 4 h prior to irradiation, the vials were removed from the refrigerator to allow for adaption to room temperature.

2.2. 3D printing material and printing techniques

To test the usability of different 3D printing materials, a first set of test vials (figure 1(a)) was designed having a similar size and shape as BAREX™ containers (table 1). BAREX™ (VELOX GmbH, Hamburg, Germany) vials were already verified for compatibility with PAGAT dosimetry (Mann *et al* 2017) and therefore used as reference in this study.

2.2.1. Support material

The PolyJet/MultiJet printing technique requires the use of support material if structures with an overhanging shape shall be printed since the subsequent layer is printed while the previous layer is still liquid. After the printing is completed, this support material has to be removed. For the VeroClear™ material, different removal methods were tested: (i) purely mechanically by means of a water jet or (ii) by applying additionally a 2% sodium hydroxide (NaOH) lye for several hours to degrease the material and to remove material residues (Stratays 2013), (iii) in addition, a printing method was tested that employs the support material on the outside rather than inside of the vials to avoid contact with the PG. In this case, the vials were printed in two separate parts, which were then glued together using the same printing material and by curing the interface of both parts with UV-light for 30 min. In case of the VisiJet M3 Crystal™ material, removal of the support material required heating to 55°C and residual support material was dissolved in a bath of sunflower oil (3DSystems Product 2012). Afterwards the vials were cleaned with a degreasing agent.

Table 1. Applied 3D printing materials and printing techniques.

Material name	Material type	3D printer	Manufacturer	Printing technique	Additional information
VeroClear™ (Stratasys 2008)	Photopolymer	Objet30 Pro™	StrataSys	PolyJet	Printed with and without use of support material (section 2.2.1)
PLA™	Polyactic acid	Ultimaker 3 Extended™	Ultimaker	Fused filament fabrication	—
PVB™	Resin based on polyvinyl butyral	Ultimaker 3 Extended™	Ultimaker	Fused filament fabrication	Treated with ethanol vapor for surface smoothing after printing
Clear™	Photopolymer	Form 2™	Formlabs	Stereolithography	—
High Temp™	Photopolymer	Form 2™	Formlabs	Stereolithography	—
VisiJet M3 Crystal™	Photopolymer	ProJet 3510 HDplus™	3DSystems	MultiJet	Printed externally at 4D Concepts GmbH (Groß-Gerau, Germany) using support material (section 2.2.1)

2.2.2. Irregular shapes

As the BAREX™ vials are available only in a single size and shape the purpose of this study was to find a 3D printing material compatible with PG dosimetry that allows designing gel containers in arbitrary geometries. Based on the previous investigations, the most promising technique for 3D printing and support material handling was selected to design irregularly-shaped gel containers (figure 1(b)).

2.3. Irradiation experiments

The gel-filled test vials were irradiated with a clinical 6 MV linear accelerator (Linac) (Artiste, Siemens Healthineers, Erlangen, Germany) using a dose rate of 3 Gy min⁻¹ measured under reference conditions at 5 cm depth and a source-axis-distance of 100 cm. Dose calculation was performed with the Raystation treatment planning system (RaySearch Laboratories, Stockholm, Sweden) and the dose delivery has an accuracy of about 0.5% for the setup of our experiment. For irradiation, the printed test vials were inserted into a water-filled cylinder phantom (Mann *et al* 2017). The centre of the test vials was positioned to the isocentre marked by the in-room laser system (LAP GmbH Laser Applikationen, Lüneburg, Germany). After irradiation, the vials were wrapped in Aluminum foil and stored at room temperature. As a reference, all irradiations were repeated with a gel-filled BAREX™ container under identical conditions.

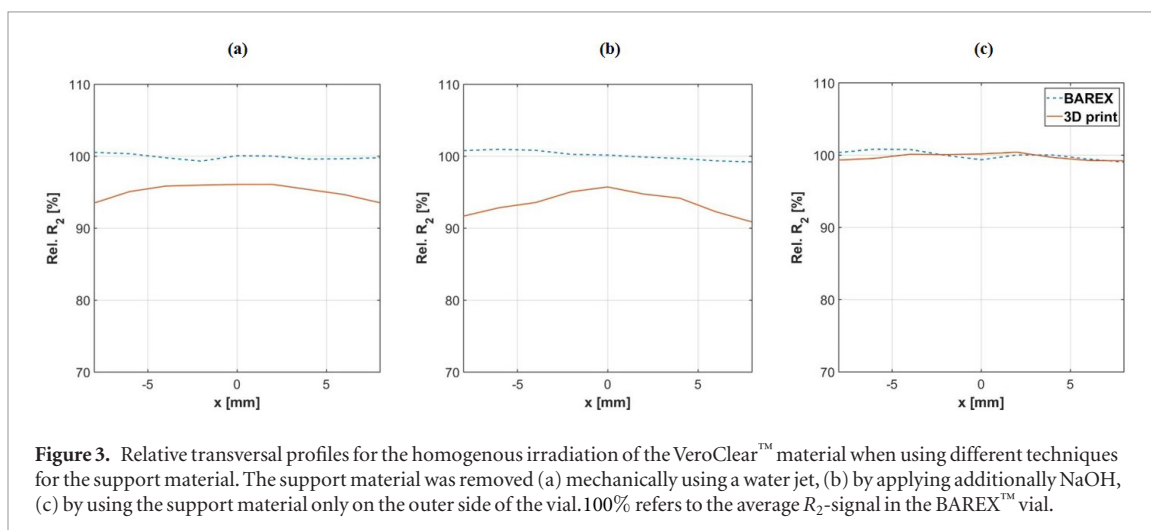
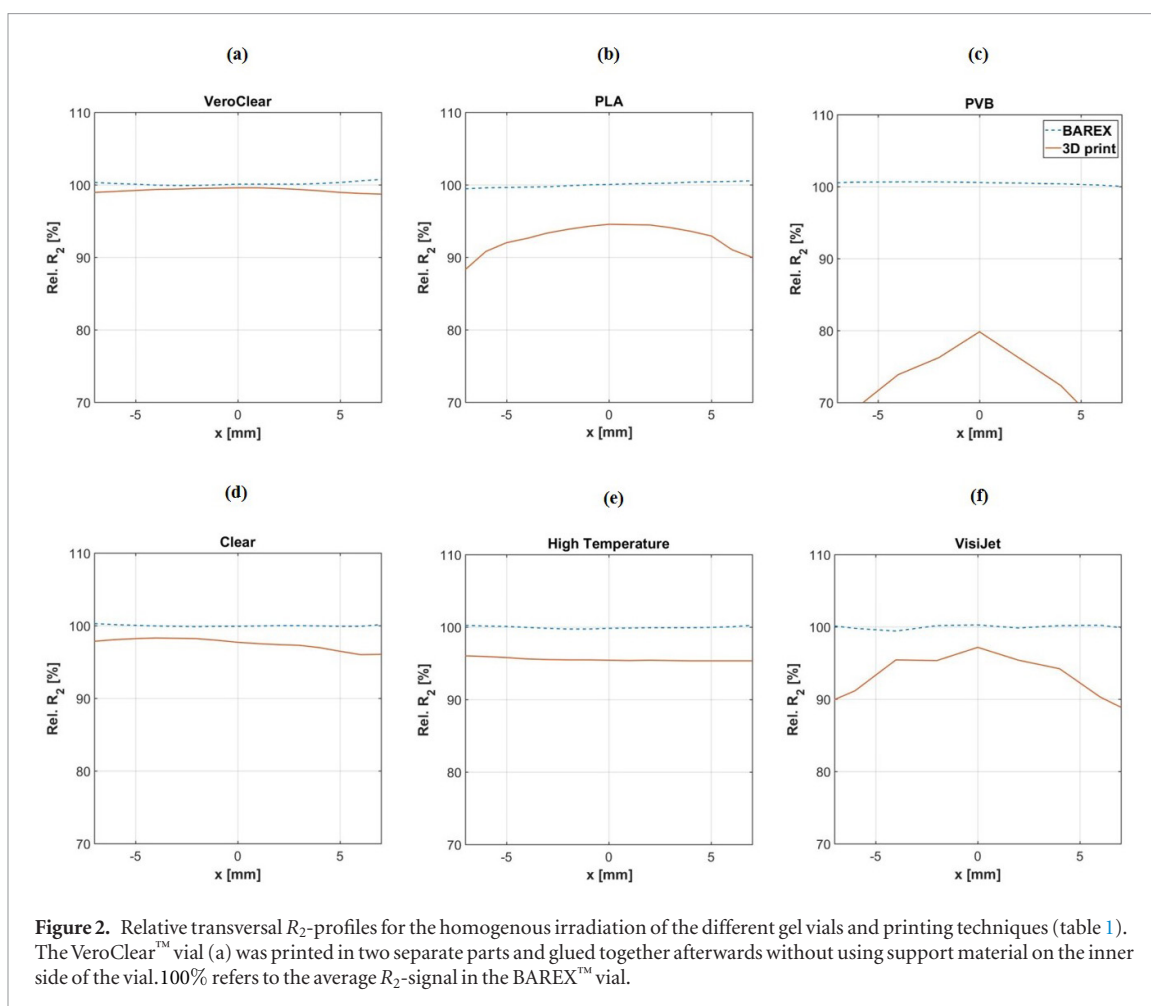
Two different irradiation field geometries were applied:

- Homogenous irradiation. Two opposing and equally-weighted beams (90° and 270°) with a field size of 10.0 × 10.0 cm² were used to prescribe a total dose of 4 Gy to the centre of the container leading to a homogeneous dose distribution over the whole volume of the BAREX™ reference vial. The homogenous irradiation was performed for all vials printed with different materials (table 1) and removal techniques of support material (section 2.2.1). The irregularly-shaped container was irradiated under identical conditions.
- Small-field irradiation. Based on the results in (a), the most promising printing technique and support material handling was further investigated. For this, three equally-spaced beams (0°, 120° and 240°) with a field size of 1.0 × 1.0 cm² were applied, prescribing a maximum dose of 5 Gy to the centre of the PG within the BAREX™ reference vial. The high dose gradients were located within the PG.

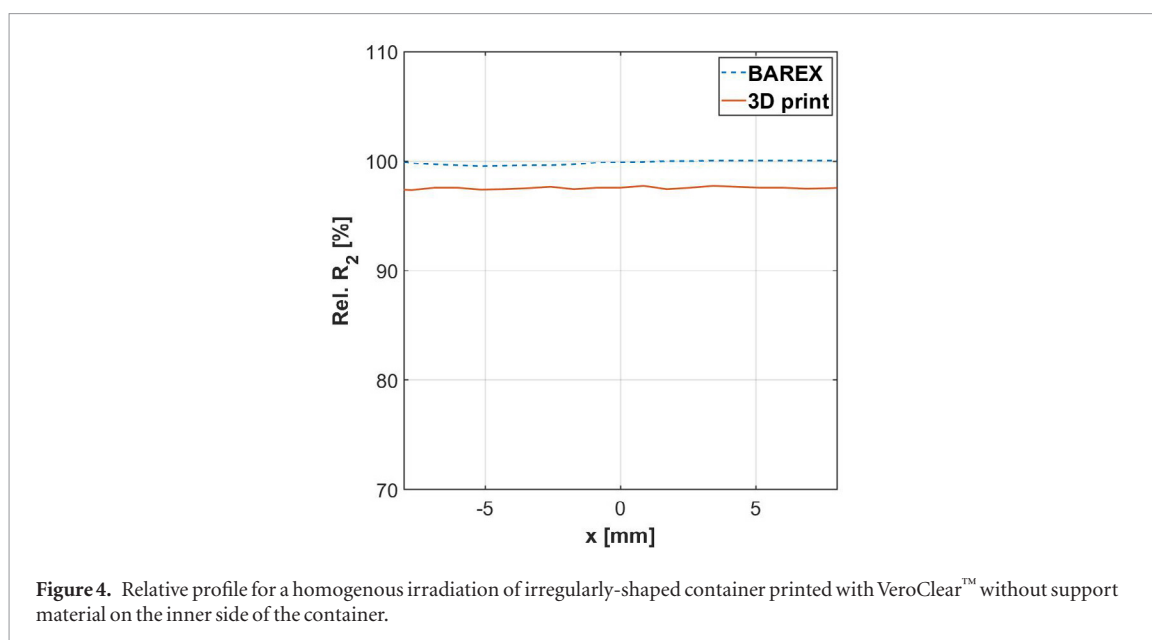
2.4. Evaluation

2.4.1. MR imaging

Approximately 48 h after irradiation, the gel containers were imaged on a 3 T Biograph mMR (Siemens Healthineers, Erlangen, Germany). To avoid influences of temperature differences on quantitative R₂ measurements, the containers were scanned within a water-flow phantom allowing for temperature constancy within ±0.1°C (Mann *et al* 2017). The phantom was placed inside a 16-channel head/neck coil and scanned using a multi spin-echo sequence with 32 equidistant echoes with echo times TE = 27.5 – 880.0 ms and an



echo spacing of 27.5 ms. The signal-to-noise ratio (SNR) was optimized to $\text{SNR} \approx 290$ ($\text{SNR} = \overline{R_2}/\sigma$ with mean R_2 value $\overline{R_2}$ in an exemplary region of interest within the BAREX™ reference and the corresponding standard deviation σ). The scans were performed with a resolution of $1.0 \times 1.0 \times 1.0 \text{ mm}^3$, band width of $\text{BW} = 130 \text{ Hz/pixel}$ and a repetition time $\text{TR} > 4000 \text{ ms}$ to exclude influences of T_1 -relaxation. For comparison of the different MR images, an additional high-resolution ($0.5 \times 0.5 \times 0.5 \text{ mm}^3$) 3D-image of the gel containers was acquired, which was used for registration purposes. For this, a standard true fast imaging sequence with steady state precession (TrueFISP) (Scheffler and Hennig 2003, Chavhan et al 2008) as implemented by the MRI vendor was applied with the following imaging parameters: $\text{TR} = 5.43 \text{ ms}$, $\text{TE} = 2.72 \text{ ms}$, number of averages = 2, and a flip angle of 30° .



2.4.2. Post processing

The MR data was processed on a personal computer using an in-house developed Matlab (The Mathworks Inc., Natick, USA)-based PG evaluation tool (Mann *et al* 2017) to calculate the spin–spin relaxation rate $R_2 = 1/T_2$. To compare the R_2 -profile between the different materials, MR images were co-registered by means of a point-based 3rd order B-Spline interpolation algorithm using three uniquely defined points as indicated by external markers (Beekly Medical, Bristol, USA). This was done with the image processing platform MITK (Nolden *et al* 2013).

3. Results

3.1. Homogenous irradiation

3.1.1. Printing material

The relative R_2 -profiles of the homogenous irradiation are displayed for the tested materials using a representative transversal slice (figure 2). The VeroClear material showed a homogenous profile with a mean deviation of $(-1.2 \pm 0.4) \%$ relative to the BAREX™ reference material ($n = 279$ voxel). The whole evaluated volume (15 slices) within the PG revealed a mean deviation of $(-1.4 \pm 0.6) \%$ ($n = 4072$ voxel). The maximum difference between voxels in the two vials was $< 3\%$. In contrast, the signal for PLA™, PVB™ and VisiJet™ decreased in the regions close to the walls of the vial (figures 2(b), (c) and (f)). In the vials printed with the stereolithographic technique (Clear™ & High Temp™, figures 2(d) and (e)), perforations of the container wall were found in the vial during the filling with PG (see discussion).

3.1.2. Support material

Based on the promising results in section 3.1.1, VeroClear™ was evaluated in more detail. Figure 3 shows a comparison of the transversal profiles for the homogeneously irradiated VeroClear™ material when using different techniques for the removal of the support material. Only the gluing technique without the use of support material on the inner side of the vial showed a good agreement with the BAREX™ reference material, while the other techniques exhibit a lower signal, which decreased further towards the wall of the vials. Based on these results, the VeroClear™ material without the use of support material on the inner side of the vials was investigated in further experiments.

3.1.3. Irregular shape

The homogeneous irradiation of an irregularly-shaped container printed with the VeroClear™ material revealed a homogenous signal response and showed a similar profile as the BAREX™ reference vial (figure 4), whereas the absolute signal was about 3% smaller in the 3D printed container compared to the reference (see discussion).

3.2. Small-field irradiation

Figure 5 shows the transversal and sagittal profiles of the small-field irradiation for the BAREX™ and VeroClear™ material without the use of support material on the inner side of the vial. The profiles are well comparable and the maximum position shows only minor deviations of < 1 mm.

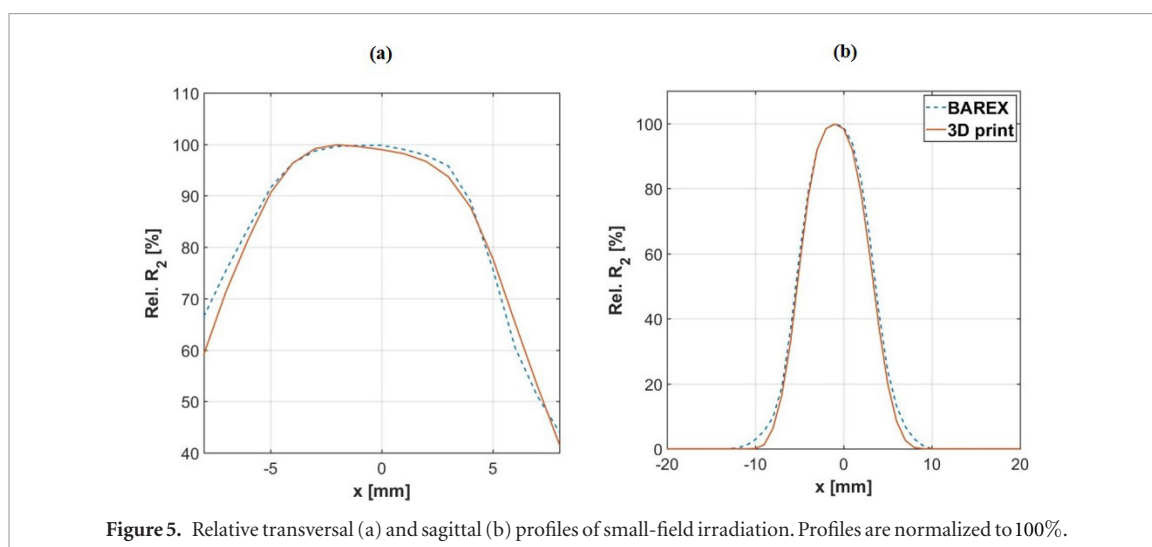


Figure 5. Relative transversal (a) and sagittal (b) profiles of small-field irradiation. Profiles are normalized to 100%.

4. Discussion

In this work, it has been shown that the VeroClear™ material in combination with the Objet30 Pro 3D printer (StrataSys) can be used to produce containers, which are compatible with the PAGAT polymer gel. With this material, a homogenous irradiation lead to a uniform signal response with only small deviations ($< 3\%$, figure 2(a)) relative to the BAREX™ reference vials. All other tested materials showed a signal decrease in the vicinity of the container wall and can therefore considered as incompatible with the use of PG. This ‘wall-effect’ may be explained by an oxygen-permeability of the materials, which leads to a partial inactivation of the PG. In case of the stereolithographic printing technique (Clear™ & High Temp™) tiny holes with a diameter of approx. 1 mm were found in the material. These holes may origin from the mechanical removal of support struts required for the printing process.

Using the VeroClear™ material allows printing of arbitrary gel containers. However, this was only possible, if no support material was used on the inner side of the container wall during the printing process as direct contact of the support material with the gel lead to a change of the signal response (figure 3). Most likely, this change is a result of chemical reaction of the PG with either residual support material or with remaining contaminations of the NaOH lye used for the removal of the support material (Baldock *et al* 2010).

For containers with varying cross section it is necessary to use support material and for PG container production this is still possible as long as the support material is used only on the outer side of the gel containers. This, however, requires printing of the containers in two separate parts, which have to be glued together afterwards (see section 2.2.1). The gluing uses the same printing material and after curing the interface by UV-light, a highly homogenous signal response similar to that of the BAREX™ reference vial was obtained (figure 3). The advantage of 3D printing is the generation of arbitrarily-shaped gel containers as demonstrated by the irregular container (figure 1(b)), for which a homogeneous irradiation still leads to a homogeneous signal response (figure 4).

Compared to the BAREX™ reference vial, the homogenous irradiations of the regularly-shaped test vials revealed a mean signal difference of $(-1.4 \pm 0.6)\%$ (figures 2(a) and 3(c)). In the irregularly-shaped container a slightly larger difference of 3% was found (figure 4). This larger deviation may result from differences in the volume and shape of the containers, leading to a different temperature equalization and as a consequence to a difference in the chemical polymerization rate (Sedaghat *et al* 2009). Especially, the temperature during and after irradiation may influence the polymerization rate (De Deene and Vandecasteele 2013). Depending on the gel container size, a small temperature difference may equalize differently leading to a small offset in the gel response. However, for relative dosimetry performed in this work, an offset in R_2 is of not critical.

In addition, using the VeroClear™ test vials, steep gradients could be measured with high accuracy (figure 5) and the position of the maximum signal agreed well with that in the BAREX™ reference vials with deviations of < 1 mm.

Having identified a combination of a 3D printing technique and a printing material, which is compatible with PG, it is now feasible to design almost arbitrarily-shaped gel containers. This is a very important feature to perform 3D dose verification in various geometric or anthropomorphic phantoms. These phantoms can be used for QA measurements and end-to-end tests, especially when new treatment techniques are introduced. One important example is MR-guided radiotherapy (MRgRT) (Lagendijk *et al* 2008, Fallone *et al* 2009), where it is intended to adapt the treatment plan at each fraction to compensate for changes of the patient anatomy. Validating the adapted treatment plan with PG dosimetry in a clinically relevant setting could be an important application of the proposed method.

5. Conclusion

In this study, the compatibility of 3D printing materials and printing techniques with PAGAT gel dosimetry was investigated. The VeroClear™ material has been identified as a suitable material, when the support material is used only on the outer side of the container during the printing process. For this, the container has to be printed in two parts and glued together afterwards. Relative PG measurements in homogeneous irradiation fields revealed an agreement of the gel response of < 3% when compared to measurements in the BAREX™ reference container, if similarly shaped test vials are used. Using this method, also steep dose gradients can be measured accurately.

Acknowledgments

This project has received funding from the EMPIR programme co-financed by the Participating States and from the European Union's Horizon 2020 research and innovation programme. Additionally, we would like to thank Professor Dr K Kopka for providing the lab space for the production of the polymer gel.

Conflict of Interest

One of the authors, Dr Mann is shareholder of the company HQ-Imaging.

ORCID iDs

A Elter  <https://orcid.org/0000-0002-0295-4861>

S Dorsch  <https://orcid.org/0000-0002-8185-8644>

P Mann  <https://orcid.org/0000-0002-2857-4861>

References

- 3DSystems Product 2012 *Post Processing Operation Guide and Best Practices for Parts Built on the ProJet™ 3500 and 5000 Professional 3D Printers* (Rock Hill, SC: 3DSystems Product) pp 1–9 (<http://stmichaelshospitalresearch.ca/wp-content/uploads/2016/05/Post-Processing-Guide.pdf>)
- Baldock C et al 2010 Polymer gel dosimetry *Phys. Med. Biol.* **55** R1–63
- Chavhan G B et al 2008 Steady-state MR imaging sequences: physics, classification, and clinical applications *RadioGraphics* **28** 1147–60
- De Deene Y et al 2002 A basic study of some normoxic polymer gel dosimeters *Phys. Med. Biol.* **47** 3441–63
- De Deene Y and Vandecasteele J 2013 On the reliability of 3D gel dosimetry *J. Phys.: Conf. Ser.* **444** 012015
- De Deene Y, Vergote K, Claeys C and De Wagter C 2006 The fundamental radiation properties of normoxic polymer gel dosimeters: a comparison between a methacrylic acid based gel and acrylamide based gels *Phys. Med. Biol.* **51** 653–73
- Doran S J 2009 The history and principles of chemical dosimetry for 3D radiation fields: gels, polymers and plastics *Appl. Radiat. Isot.* **67** 393–98
- Fallone B G et al 2009 First MR images obtained during megavoltage photon irradiation from a prototype integrated linac-MR system *Med. Phys.* **36** 2084–8
- Guo P, Adamovics J and Oldham M 2006 A practical three-dimensional dosimetry system for radiation therapy *Med. Phys.* **33** 3962–72
- Kamomae T et al 2017 Three-dimensional printer-generated patient-specific phantom for artificial *in vivo* dosimetry in radiotherapy quality assurance *Phys. Med.* **44** 205–11
- Koeva V I et al 2009 Preliminary investigation of the NMR, optical and x-ray CT dose–response of polymer gel dosimeters incorporating cosolvents to improve dose sensitivity *Phys. Med. Biol.* **54** 2779–90
- Lagendijk J J W et al 2008 MRI/linac integration *Radiother. Oncol.* **86** 25–9
- Low D 2015 The importance of 3D dosimetry *J. Phys.: Conf. Ser.* **573** 012009
- Mann P et al 2017 3D dosimetric validation of motion compensation concepts in radiotherapy using an anthropomorphic dynamic lung phantom *Phys. Med. Biol.* **62** 573–95
- Nolden M et al 2013 The medical imaging interaction toolkit: challenges and advances *Int. J. Comput. Assist. Radiol. Surg.* **8** 607–20
- Oh D et al 2017 Development of patient-specific phantoms for verification of stereotactic body radiation therapy planning in patients with metallic screw fixation *Sci. Rep.* **7** 40922
- Sandilos P et al 2004 Dose verification in clinical IMRT prostate incidents *Int. J. Radiat. Oncol. Biol. Phys.* **59** 1540–7
- Scheffler K and Hennig J 2003 Is TrueFISP a gradient-echo or a spin-echo sequence? *Magn. Reson. Med.* **49** 395–97
- Schreiner L J 2015 True 3D chemical dosimetry (gels, plastics): development and clinical role *J. Phys.: Conf. Ser.* **573** 012003
- Seco J, Clasié B and Partridge M 2014 Review on the characteristics of radiation detectors for dosimetry and imaging *Phys. Med. Biol.* **59** R303–47
- Sedaghat M et al 2009 Volume-dependent internal temperature increase within polymer gel dosimeters during irradiation *J. Phys.: Conf. Ser.* **164** 012009
- Stratasys 2013 *Guide to Basic Post Process Applications—Objet Line of 3D Printers* (Eden Prairie, MN: Stratasys) http://cui.unige.ch/printer3D/lib/exe/fetch.php?media=application_booklet_a4_print.pdf
- Stratasys 2008 VeroClear–Rigid Transparent PolyJet Material (Eden Prairie, MN: Stratasys) (http://www.stratasys.com/-/media/files/material-spec-sheets/mss_pj_veroclear_0318a.pdf)
- Vandecasteele J and De Deene Y 2013 On the validity of 3D polymer gel dosimetry: I. Reproducibility study *Phys. Med. Biol.* **58** 19–42
- Vergote K et al 2004 Validation and application of polymer gel dosimetry for the dose verification of an intensity-modulated arc therapy (IMAT) treatment *Phys. Med. Biol.* **49** 287–305
- Yea J W et al 2017 Feasibility of a 3D-printed anthropomorphic patient-specific head phantom for patient-specific quality assurance of intensity-modulated radiotherapy *PLoS One* **12** e0181560

3 Discussion

MRgRT has the potential to significantly reduce margins and thereby radiation exposure of normal tissue while maximizing the dose to the tumor. However, this results in the need for a high geometric accuracy of both the irradiation and the imaging system, which has to be checked on a regular basis. As new challenges arise by adding a magnetic field to radiation therapy devices, also the QA-methodology needs to be adapted. Machine-QA has to be modified and new methods and phantoms have to be developed. Due to the high complexity of the adaptive MRgRT processes, also workflow-specific QA methods become increasingly important. A suitable workflow verification phantom requires anthropomorphic image contrasts and must be reproducibly deformable. In addition, the target volume should be irregularly shaped and accessible for dosimetric validation, preferably in 3D.

In this thesis new methods for QA-procedures in MRgRT were developed. In particular, machine-related QA (publications I-III), such as checking the alignment of irradiation and imaging isocenter (publications II, III) and the contribution of MRI-related uncertainties like geometric distortions (publication III) were key elements of the development. A novel approach of irradiation isocenter measurements based on polymer dosimetry gel was investigated with respect to feasibility and comparability to film measurements, which present the current gold standard on conventional treatment machines (publication I). Using an electromagnet, a magnetic field ranging from 0 T to 1 T was generated to perform preliminary examination of the behavior of films and dosimetry gels in magnetic fields. In addition, the procedure was tested on a clinical MR-Linac to optimize and adapt the available imaging sequences (publications II, III). Finally, a dedicated phantom was developed to combine the radiation isocenter measurement (for the first time in 3D) with measurements of the imaging isocenter position to quantify the coincidence of both reference points and additionally perform measurements of geometric image distortions in 3D (publication III). All developments were applied and validated on a clinical 0.35 T MR-Linac.

In addition, preparatory experiments for the development of an end-to-end workflow-verification phantom were carried out (publication IV). For this, several 3D printing materials were tested for compatibility with the dosimetric PG. This is the first important step towards the development of complex shaped phantoms, which allow for dosimetric measurements in 3D.

3.1 Machine-related geometric accuracy

3.1.1 *Irradiation-related accuracy*

In publication I. the suitability of PAGAT PG for measuring the in-plane irradiation isocenter was compared to the gold standard film in terms of geometric accuracy on a conventional Linac. Although the spatial resolution of the MR image is significantly lower than the resolution of the film, the evaluation of the two dosimeters revealed comparable results with similar geometric accuracy when using the same commercial evaluation tool. Due to the described evaluation routine (publication I), an accuracy significantly better than the pixel size could be achieved. Also the time point

of the PG evaluation was investigated as the PG still polymerizes for up to 48 hours after irradiation [90]. Although the absolute T_2 -values of the PG in the intersection area of the beams decrease from 460 ms (after 1 h) to 420 ms (after 2 d), the resulting geometric parameters (IC_r and IC_d) changed only negligibly. Furthermore, the tolerance level for a star shot measurement of 0.5 mm for the isocircle radius (IC_r), as recommended by the Task Group 142 report [122] was always met. Chemical effects of polymerization within 48 h post-irradiation are therefore not important for the determination of geometric parameters such as IC_r and IC_d . This is a very important finding as it allows the evaluation of PG without any delay, directly after irradiation. This is especially interesting for MR-Linac devices as the phantom can be evaluated in the same device without being moved.

The first isocenter measurements within the electro magnet revealed slightly increased IC_r for both, film and PG (publication I). This is due to the fact, that the beam profiles are influenced by the magnetic field (as described in 1.3.1) leading to an increased IC_r . Furthermore, it has to be noted that the complex experimental realization may introduce additional uncertainties that further increase the IC_r . However, for a low magnetic field (0.35 T, as in the case for the MR-Linac used in this work), IC_r still does not exceed the recommended tolerance levels. For higher fields (e.g. such as for the Elekta Unity system with 1.5 T), the IC_r may reach values up to 2.35 ± 0.35 mm. Recently, van Zijp et al. proposed a method to compensate for this effect [99]. The authors used a copper ring being directly attached to radiochromic films to reduce the range of the secondary electrons. By this reduction of the free path length, the influence of the magnetic field is reduced to a minimum and the IC_r was reduced from 2.35 ± 0.35 mm to 0.22 ± 0.03 mm. However, this method can only be applied in 2D and is not suitable for an isocenter determination with PGs due to possible chemical reactions.

The measurements of the distance of the isocircle center to the laser-marked reference position (publication I) or imaging isocenter (publication III)) (IC_d) was independent of the magnetic field, if the employed beams were equally spaced around the phantom. However, as the experimental setup in publication I did not allow for a full gantry rotation and thus only the upper hemisphere could be irradiated, the phantoms with the detectors had to be rotated by 180° after irradiation of the first three beams to imitate a full gantry rotation. This may have introduced additional uncertainties that will not be present at a clinical MR-Linac device. For this reason, the measurement described in publication I was recently repeated on a conventional Linac, placing the electro-magnet directly on the treatment table, which allowed for a full gantry rotation. In this setup, a star shot irradiation was performed both with and without magnetic field and in accordance with publication I, no dependence of the IC_d on the magnetic field was determined for fields as low as 0.35 T.

Publication I demonstrates that evaluation of the PG directly after irradiation is feasible, if only geometrical parameters are of interest. This allows using PGs for star shot measurements to evaluate the radiation isocenter accuracy immediately after irradiation with comparable accuracy as with radiochromic films. As the IC_d is found to be independent of the magnetic field, the center of the IC is also independent of the magnetic field and can be used to determine the position of the isocenter.

3.1.2 *Imaging-related uncertainties*

Machine-related inhomogeneities of the static magnetic field, gradient non-linearities and eddy currents may lead to geometric image distortions and subsequently to inaccurate representation of the patient's anatomy. While this is less critical for purely diagnostic MRI-applications, these distortions can have an high impact on the delivered radiation dose in MRgRT [109,114]. Especially the bSSFP sequence (see section 1.1.2), used as fast imaging sequence at the MRIdian MR-Linac, is prone to magnetic field inhomogeneities. In publication III, a dedicated phantom and a method to measure distortions in 3D are presented and applied on a 0.35 T clinical MR-Linac.

A significant benefit compared to the manufacturer's recommended workflow is the measurement in 3D providing full distortion information of each of the 1330 control points. In contrast, the commercial phantom has to be scanned in several different orientations and provides only the 2D information within the respective slice. Additionally, this requires substantial measurement and working time, as each orientation has to be individually scanned and afterwards the phantom has to be repositioned manually.

It has to be noted, that the distortions measured in 3D with the developed phantom only had a passing rate of 95% for the first tolerance criterion of the manufacturer (<1 mm distortion for 100% of control points within a 100 mm sphere around the isocenter), while the recommendations were met for the commercial phantom. This could originate from the fact that the control points in our phantom contained significantly less pixels leading to a larger variability of the reconstructed positions. While up to 70 pixels were evaluated in the commercial phantom to determine the center of mass of one control point, the grid intersections of our phantom were marked by only 1–9 pixel. Therefore, falsely segmented pixels have higher impact on the center of mass position. For future applications, it may therefore be of advantage to substitute the grid structures by thicker grids or planes with holes [115,116,123], leaving the total number of control points unchanged. Increasing the size of the control points relative to the grid intersections would then increase the evaluated part of each control point, which in turn would increase the number of evaluated pixel and thus the geometric precision.

An additional imaging-related uncertainty may be induced by the movement of the gantry. As described in 1.3.2 the MRI isocenter is defined by the fixed geometry of the gradient coils and is therefore expected to be fixed in space. However, it was recently shown that the MRI isocenter may be shifted by up to 1.3 mm for different gantry positions [124] while the previous version of the ViewRay 0.35 T MR-Linac, which was equipped with three equally spaced ^{60}Co -heads [51], was not reported to have such effects. The asymmetrical Linac placement on the gantry-ring (Figure 5) of the current MR-Linac could induce eddy currents, leading to a resonance frequency shift, which could be responsible for the isocenter shift. As the eddy current calibration during commissioning of the machine is usually performed at 0° gantry angle, deviation at other gantry angles remained undiscovered.

3.1.3 Irradiation & Imaging alignment

The alignment of imaging and irradiation isocenter is of great relevance for all image-guided radiotherapy devices and is not restricted to MR-guided devices only. As described in section 1.3.2 the manufacturer's recommended workflow for the device used in this work uses laser-aligned film dosimeters in a very cumbersome workflow. First, the irradiation isocenter position in transversal and longitudinal direction as defined by the lasers has to be measured, and the lasers have to be readjusted, if necessary. Finally the coincidence of laser and imaging isocenter is measured with an additional phantom. As MRgRT aims at image-based positioning independent from a laser system, the other commercially available MR-Linac type (Elekta Unity) is not even equipped with a laser. In contrast to the MRIdian system, the Elekta Unity system is additionally equipped with an electronic portal imaging device (EPID), which is located on the opposite side of the Linac. The EPID can be used to measure the x-ray intensity transmitted through a patient during a treatment session. For isocenter accuracy measurements, a phantom with seven ZrO_2 spheres, that are visible on the portal image, and other structures visible in the MR-image can then be used to check the irradiation and imaging isocenter alignment [105]. This method offers high accuracy, however, due to the lack of an EPID-device, it is not applicable at the MRIdian system used in this work. Therefore a simplified procedure, independent of the laser system and not relying on an EPID, preferably with just a single phantom setup, is highly desirable.

Measurement of the isocenter alignment in MRgRT-devices with one single dedicated phantom includes several requirements regarding the phantom design as well as the evaluation procedure: (i) as the positioning of the patient in clinical practice is image- rather than laser- based, at least part of the phantom has to be visible in the MR-images. (ii) To visualize the irradiation isocenter, either several differently oriented 2D or a single 3D radiation detectors are required. (iii) To evaluate the isocenter alignment, the position of the imaging isocenter has to be either transferred to the detector (each individual film in case of 2D or to the images of the polymer dosimetry gel in 3 D) or the measured position of the irradiation isocenter has to be transferred to the MR-image. Water-based PGs are a well-suited detector as they are (i) visible in MRI, (ii) provide geometric information in 3D and (iii) the polymerized part of the irradiated gel, leading to the reconstruction of the irradiation isocenter, can be seen in the images. Further, the geometric accuracy is comparable to that of films and the evaluation of the PG may be performed immediately after irradiation (publication I), which is important to keep the phantom's residence time in the MR-Linac as low as possible.

Multi contrast measurements

In addition to the phantom requirements (i)-(iii), the sequences used for evaluation of the PG have to meet specific requirements:

Signal intensity: The signal-to-noise ratio (SNR) of MR images depends on various parameter, such as the magnetic field B_0 , the pixel size $(\Delta x, \Delta y)$, slice thickness (Δz) , the number of averages (NSA) and the receiver bandwidth (BW) [125]:

$$\text{SNR} \propto B_0(\Delta x)(\Delta y)(\Delta z) \sqrt{\text{NSA}/\text{BW}} \quad (3.1)$$

Isotropic resolution: To reach a geometric accuracy comparable to film measurements, the MRI measurement of the PGs in publication I had a high in-plane resolution of $0.5 \times 0.5 \text{ mm}^2$. However, as no 3D evaluation was performed for the direct comparison of PG and film to obtain a good SNR, a slice thickness of 5 mm has been used. For a real 3D evaluation of the irradiation isocenter position, it was necessary to reduce the slice thickness to the in-plane pixel size to obtain an isotropic resolution.

Measurement time: The measurement at the MR-Linac time should be within an acceptable range. Together with the requirements for SNR and spatial resolution, this imposes several challenges: According to equation (3.1), the SNR is expected to decrease by a factor of 8.6 for the transition from a 3 T MRI to a 0.35 T MR-Linac, and by an additional factor of 10 for the reduction of the slice thickness. Using additional k-space acquisitions (NSA) the SNR can be improved. The increase in the acquisition time is proportional to the NSA, whereas the increase in SNR is only proportional to $\sqrt{\text{NSA}}$.

While the MRI images in publication I were acquired with an MSE sequence, there was no such sequence available at the MR-Linac shortly after commissioning. Therefore, first measurements at the 0.35 T MR-Linac, presented in publication II, were performed using two consecutively double spin-echo sequences using different echo times to acquire multiple contrasts for the generation of T_2 -maps. Compared to publication I, the correlation coefficient R^2 of the fit were significantly lower for the 0.35 T measurements with 4 echoes ($R^2=0.90-0.94$) as compared to the 3 T measurement with 32 echoes ($R^2>0.98$). Due to the low SNR, also the reduction of slice thickness was limited for this measurement, which made a full 3D isocenter alignment analysis impossible. Finally, the in-plane pixel size of 0.5 mm was found to be too small with respect to SNR for measurements at the 0.35 T MR-Linac.

Increasing the in-plane resolution to $1.0 \times 1.0 \text{ mm}^2$ improved the image quality sufficiently to evaluate the star shot measurement. By this, the irradiation and imaging isocenter alignment could be evaluated in 2D and the results were confirmed by separate measurements on a high field (3 T) MRI. A limitation of this method was, however, that an isotropic resolution could not be achieved.

Single contrast measurements

In contrast to the publications I & II, where multi-contrast MRI measurements have been performed to generate quantitative T_2 -Maps, publication III employed a single measurement using a turbo spin-echo sequence, which was available in the research mode of the MR-Linac only after a service update. This sequence acquires one single T_2 -weighted image rather than several images of different contrast, so a T_2 -map could not be generated. In spite of this limitation, it was possible to reduce the slice thickness and to obtain an isotropic spatial resolution of 1 mm for the irradiation isocenter measurement. Furthermore, the acquisition time could be reduced to 3 min 16 s for a single image acquisition due to the acquisition of multiple phase-encoding steps (lines of k-space) within a given repetition time (see 1.1.2). To improve the SNR, the number of signals averaged (NSA) was increased (12, 24 and 32 acquisitions). Although the evaluation shown in publication III did not show a significant differences in terms of isocenter position for different NSA, the measurement with lower NSA showed a slightly higher uncertainty due to a

lower SNR. As the total acquisition time of 32 NSA (1 h 45 min) is comparable to the acquisition time of the multi-contrast measurement in publication II (1 h 27 min), it is recommended to use the higher number of signal averages, if there are no other specific requirements for a shorter measurement time. Finally, the T₂w-TSE provides seven-fold higher SNR within a comparable acquisition time as compared to the dual spin-echo presented in publication II (scaled to a slice thickness of 1mm). In principle, a PG-based measurement of the isocenter accuracy could be performed with any other T2-weighted sequence.

Regarding the employed turbo-spin sequence, the fact that this sequence is currently not generally available on all MRIdian devices may pose a limitation for other users of the MRIdian MR-Linac, however, the manufacturer has already announced upgrades of the system with this respect in the near future [126].

3.1.4 *Clinical validation at MR-Linac*

With the developed phantom and measurement techniques, the first ever PG-based isocenter alignment measurement in 3D was performed and the accuracy of the alignment was found to be (0.8 ± 0.9) mm. No significant tilt of the beams against the transversal plane could be detected. Additionally the spatial image distortions after machine specific correction were investigated with the same phantom. As a result, the mean distortion within a 140 mm sphere around the isocenter was (0.60 ± 0.28) mm and 99.82% of the evaluated control points had distortions below 1.5 mm. These remaining geometrical uncertainties have to be considered by additional safety margins in MRgRT treatments.

As all measurements have been performed at gantry angle 0°, however, further uncertainties may arise for MR measurements at different gantry angles as the imaging isocenter may be shifted due to eddy current effects [124]. This may further increase the size of the safety margins.

Using dosimetry gels for isocenter accuracy measurements has several benefits and limitations. As measurements of geometric parameters lead to comparable results as film measurements, PG-based isocenter measurements may offer a good alternative, providing several advantages. As the gel is MR-visible, the evaluation of PGs within an MR-Linac can be performed immediately after irradiation at the MR-Linac without moving the phantom and thereby introducing further uncertainties. In addition, PGs offer the possibility to determine the irradiation isocenter in 3D with an accuracy of <1 mm. The potential of PG-based isocenter tests has recently been recognized also by other investigations [127]. As the irradiation of PGs leads to local changes in mass density, they may in principle also be evaluated in CT [87]. Recently, Adamson et al. [127] have investigated whether the delivered dose can be visualized directly after irradiation using on-board kV-CBCT to quantify the alignment of radiation and imaging isocenter at a conventional Linac.

A further benefit of the 3D evaluation with PGs is the possibility to determine potential inclinations of the beams relative to the transversal plane. For this the entry and exit areas of the beams are compared. However, the accuracy of the inclination determination is strongly dependent on SNR and spatial resolution, which are significantly higher at higher magnetic fields.

A limitation of PG dosimetry is the handling of PGs, which is quite challenging as they are strongly reactive with oxygen and the production requires a dedicated lab space as well as time. However, if this is granted, the established production workflow (see appendix) reveals very promising results. It is further important to note that the accuracy of the isocenter alignment measurement is significantly influenced by the available MR sequences, which have a major impact on SNR, slice thickness and resolution, acquisition time, image artifacts and contrast.

3.2 Development of phantoms for workflow validation

Besides machine-related geometric accuracy measurements also patient-specific quality assurance is of high interest in MRgRT. This especially includes end-to-end tests including imaging for treatment planning and positioning, the treatment plan adaption or beam gating process as well as the dose delivery. With these tests the feasibility of the treatment process as well as the overall uncertainty are evaluated [117]. As described in 1.3.4, especially the validation of treatments in presence of interfractional motion is important and requires dedicated anthropomorphic phantoms. Such phantoms should allow for reproducible organ deformations, anthropomorphic image contrast and have to be MR-compatible. As 3D dose measurements with conventional detectors are usually limited with respect to spatial resolution, gel dosimetry gains increasing interest. As the high geometric accuracy of PGs in the presence of magnetic fields has been shown before (publication I-III), they offer great potential to be used for dosimetric validation in such phantoms.

PGs, however, are strongly reactive with oxygen and other potential contaminations (De Deene et al 2006) and therefore, the requirements for the gel container material are very restricting. Established container materials are BAREXTM, a chemically inert acrylate copolymer, or glass [83,128]. Both have a negligible oxygen permeability and high chemical resistance. However, these materials offer no possibility to form complex-shaped volumes. This problem could be solved by 3D printing, which offers the possibility to produce a large variety of different container shapes and which is becoming increasingly important for the design of new phantoms also in other radiotherapy fields [129–131]. Up to now, however, printing materials have not been used in combination with dosimetry gels.

As a starting point for future projects in this direction, various 3D printing materials and printing techniques were tested for their compatibility with the PAGAT PG (publication IV). The integration of 3D dose measurements into 3D printed phantoms is an important step towards the development of phantoms for end-to-end tests in the presence of interfractional anatomical changes.

In publication IV, it has been shown that the printing material VeroClearTM [132] can be used in combination with the PAGAT PG, if the support material is used only on the outer side of the container during the printing process. For this, an inverted printing method was established. This method required printing the containers in two parts, which are then glued together using the same printing material. For a homogeneous irradiation of the irregularly shaped containers with 4 Gy, a mean signal difference relative to the BAREXTM-reference container of <3% was found. Also steep dose gradients could be measured very accurately with printed containers.

Meanwhile, the results of publication IV have been used in another project to develop a phantom with i) adjustable irregular structures, ii) anthropomorphic imaging contrasts in MR and CT and iii) 3D dose measurements in organ-like structures. This phantom was used to perform an end-to-end test of an online adaptive treatment procedure at the 0.35 T MR-Linac by simulating the complete workflow including the validation of image registration, treatment plan adaption and dose delivery. The results of these measurements have been recently published [133]. The 3D dosimetry gel measurements confirmed that the adapted treatment plan resulted in dose distributions in the tumor and the OAR that were well-comparable to a static case, where no adaption of the treatment plan was necessary.

4 Conclusion

In this thesis, new methods for measuring the isocenter alignment and image distortion accuracy have been developed and a dedicated phantom has been designed and tested. This development included the use of polymer dosimetry gel and the optimization of sequences for dosimetric evaluation in 3D. In addition, a 3D printing material and a printing technique compatible with gel dosimetry was identified, establishing the foundations for the future design of anthropomorphic phantoms for end-to-end-tests in adaptive MR-guided radiotherapy.

As a first step, the polymer gel was compared with radiochromic films used as gold standard for many applications in clinical practice. No significant geometric differences as compared to film measurements were found, independent of the time point of the gel evaluation. Also, no significant differences were found in the presence of magnetic fields. Thus geometric aspects of radiation fields can be measured by polymer gels and evaluated by MRI immediately after irradiation.

In the next step, a dedicated phantom was developed allowing for simultaneous isocenter alignment and image distortion measurements. Using a CT of the phantom as ground truth, evaluation of 1330 control points revealed mean spatial image distortion of (0.60 ± 0.28) mm. Within a radial distance of 140 mm, 99.82% of the evaluated control points exhibited distortions of less than 1.5 mm. This accuracy fulfils the requirements of MR-guided radiotherapy

The same phantom was used to investigate the irradiation and isocenter alignment of an MR-Linac. For this, different MRI sequences and evaluation methods were investigated and optimized with respect to acquisition time, signal to noise ratio, image resolution and contrast. As a result, a single-contrast turbo spin-echo sequence was used at a 0.35 T clinical MR-Linac to acquire a 3D images with a 1 mm isotropic voxel size. With this sequence, phantom measurements resulted in an irradiation and imaging isocenter alignment accuracy of (0.8 ± 0.9) mm. This value is comparable to the alignment accuracy at conventional Linacs.

Finally, different 3D printing materials and printing techniques were investigated for their compatibility with the polymer dosimetry gel and as a result one suitable material together with a special printing technique has been identified. This allows designing anthropomorphic phantoms with the capability to perform 3D dosimetry in anatomical structures, which may be used in the future to perform end-to-end tests of online adaptive treatment procedure in presence of interfractional anatomical changes.

Appendix

A.1. Fabrication instructions for the PAGAT dosimetry gel

The following workflow of gel fabrication, -irradiation and -evaluation is adapted from Mann [134] and showed to be a suitable workflow to (i) minimize the influence of penetrating oxygen, (ii) to assure chemical stability after fabrication and (iii) irradiation:

Equipment, reagents and glassware needed for 1 kg of PAGAT

- Deionized water (890 g)
- Gelatine, 300 bloom (60 g)
- Acrylamide (25 g)
- Bis-Acrylamide (25 g)
- THPC (5 mMol)
- Chemical fume hood
- 2 x Temperature controlled magnetic hot-plate stirrers
- 2 x (analog) expansion thermometer
- 4 x Stir bars (length = 4 cm)
- 2 x Water bath container as heat reservoir (1.5 l)
- 2 x Beakers, (2 l)
- Scale (1 g – 100 g)
- Syringe (50 ml)
- Single-channel Pipette (100 µl – 1000 µl)
- Spatula / Spoon
- Respirator
- Safety glasses
- Protection gloves
- Gel flasks (Glass- or BAREX™-flask or a printed gel container as described in publication IV)
- Compressed nitrogen gas
- Tygon tubing and a large cannula
- Aluminum foil
- Desiccator

General protocol for making the dosimeter

The production of the gel is based on a protocol described elsewhere [91]. The entire gel production process can be divided into three general steps: (i) preparation of gelatine and monomer solution, (ii) mixing- and (iii) filling procedure. A schematic sketch of the production procedure is displayed in Figure 7.

Preparation of gelatine and monomer solution:

Monomer and gelatine solution are both prepared in separate beakers using one temperature controlled magnetic hot-plate stirrer, each. For preparation, the water reservoir is filled with hot water and heated up under constant stirring to a temperature of 42 °C. The preparation of gelatine and monomer solution needs to be prepared simultaneously.

Monomer Production:

Due to the low solubility of the bis-acrylamide monomer in water, 534 ml (60%) of the deionized water is used to prepare the monomer solution. For that, the deionized water is placed within the water bath and heated to 42 °C using the digital thermometer placed within the beaker. To ensure a homogeneous distribution of the chemical components, a stirrer is used with a maximum speed between level 1 and 1.5. When the maximum temperature is reached, 25 g acrylamide is poured into the water followed by 25 g of bis-acrylamide. The acrylamide will be dissolved within 1 minute followed by a temperature drop of approx. 1 - 2 °C. The bis-acrylamide, however, will take up to 30 minutes to be completely dissolved.

Gelatine production:

60 g gelatine is mixed with the remaining 356 ml deionized water. It is important to insert the magnetic stirrer prior to inserting the gelatine. After a 12 min swelling process, the solution is placed inside the water bath and heated up to 42 °C using the digital thermometer. A stirrer is used to ensure homogeneous mixing with a maximum speed between level 1 and 1.5

Once both, gelatine and monomers are completely dissolved, the solution is cooled down to a temperature of 32 °C. This is realized by adding cold water or ice cubes to the water bath. It is very important at this point to avoid temperatures lower than 30 °C as the gelatine will then start to thicken, therefore each water bath's temperature is controlled by a expansion thermometer.

Mixing procedure:

Once the final temperature is reached, the monomer solution is *carefully* poured into the gelatine beaker to obtain the final dosimetry gel. It should be ensured that the water level of the water bath matches the level of the dosimetry gel. To reduce the amount of dissolved oxygen [82], nitrogen is flushed for approx. 1 minutes (for larger containers lower flushing times are recommended to avoid formation of nitrogen bubbles during the storage/cooling process) with a pressure of 1.5 bar into the dosimetry gel using the tygon tubing and a large cannula. To finalize the gel production, the THPC is then added to the PG under constant stirring. It should be noted that the equipment for the filling process should be well prepared as the dosimetry gel starts to thicken once the THPC is added.

Filling procedure:

After approx. 1 minutes, the THPC is homogeneously distributed and can then be filled into the gel flasks that have been previously flushed with nitrogen. For that, use a 50 ml syringe and *carefully* pour the dosimetry into the gel container avoiding any air inclusions inside the container. To further guarantee a clear and bubble-free dosimetry gel probe, existing bubbles on the tip of

the syringe need to be removed prior to filling dosimetry gel into the flasks. As the influence of light is known to cause polymerization, the flasks were covered with aluminum foil during storage. As the creation of small bubbles inside the gel flask can still occur after production it is recommended to prepare some back-up gel flasks. At the end of the filling process, the gel flasks are stored within a nitrogen flushed desiccator inside a refrigerator at a temperature of 4 °C.

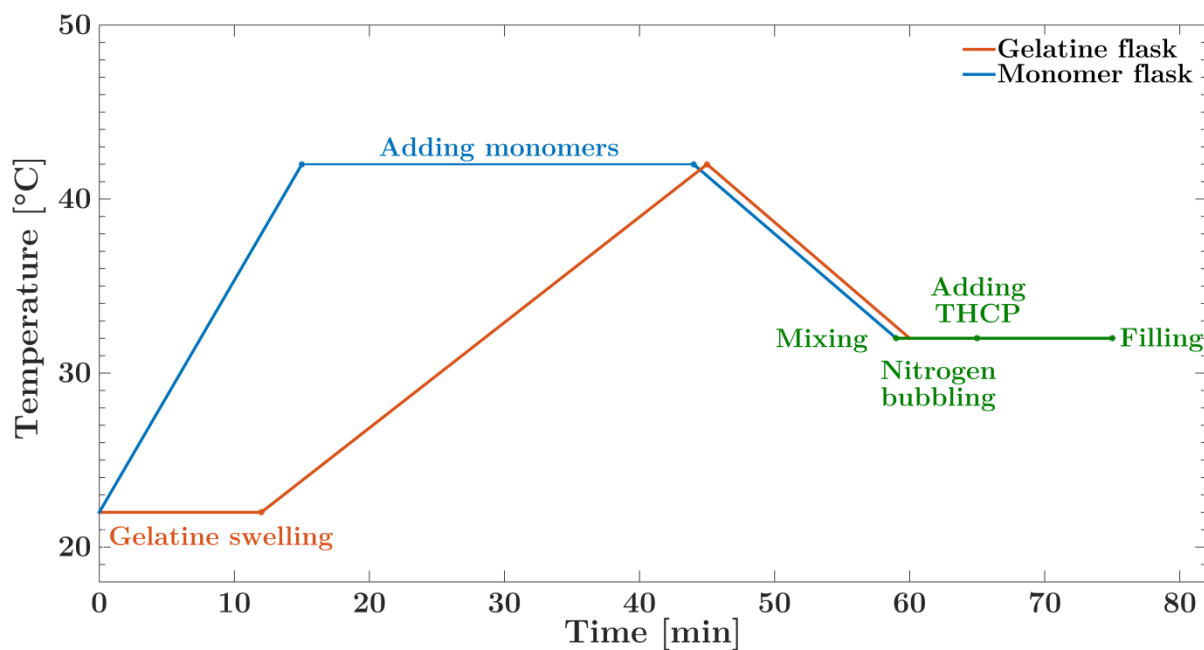


Figure 7. Schematic overview of the PAGAT fabrication workflow (from Mann et al. [134])

List of Figures

Figure 1. Dose-response curves.....	2
Figure 2. Characteristic signal profile of T_1 and T_2 relaxation	6
Figure 3. Pulse sequence of a spin-echo sequence/ Contrast behavior SE.....	7
Figure 4. Pulse sequence of a gradient-echo sequence/ Contrast behavior GRE.	8
Figure 5. Schematic drawing of the ViewRay MR-Linac System	9
Figure 6. Thematic overview of the four publications (I-IV).....	16
Figure 7. Schematic overview of the PAGAT fabrication workflow.....	75

Bibliography

- [1] Bray F, Ferlay J, Soerjomataram I, Siegel RL, Torre LA, Jemal A. Global cancer statistics 2018: GLOBOCAN estimates of incidence and mortality worldwide for 36 cancers in 185 countries. *CA Cancer J Clin* 2018;68:394–424. <https://doi.org/10.3322/caac.21492>.
- [2] Ferlay J, Soerjomataram I, Dikshit R, Eser S, Mathers C, Rebelo M, et al. Cancer incidence and mortality worldwide: Sources, methods and major patterns in GLOBOCAN 2012. *Int J Cancer* 2015;136:E359–86. <https://doi.org/10.1002/ijc.29210>.
- [3] Statistisches Bundesamt. Todesursachenstatistik 2017. <https://www-genesis.destatis.de/genesis/online?sequenz=tabelleErgebnis&selectionname=23211-0002> (accessed November 25, 2019).
- [4] Baumann M, Krause M, Overgaard J, Debus J, Bentzen SM, Daartz J, et al. Radiation oncology in the era of precision medicine. *Nat Rev Cancer* 2016;16:234–49. <https://doi.org/10.1038/nrc.2016.18>.
- [5] Paganetti H. Range uncertainties in proton therapy and the role of Monte Carlo simulations. *Phys Med Biol* 2012;57. <https://doi.org/10.1088/0031-9155/57/11/R99>.
- [6] Newhauser WD, Zhang R. The physics of proton therapy. *Phys Med Biol* 2015;60:R155–209. <https://doi.org/10.1088/0031-9155/60/8/R155>.
- [7] Knopf AC, Lomax A. In vivo proton range verification: A review. *Phys Med Biol* 2013;58:131–60. <https://doi.org/10.1088/0031-9155/58/15/R131>.
- [8] Weissbluth M, Karzmark CJ, Steele RE, Selby AH. The Stanford Medical Linear Accelerator. *Radiology* 1959;72:242–65. <https://doi.org/10.1148/72.2.242>.
- [9] Khan FM. *Physics of Radiation Therapy Third Edition*. *J Am Med Assoc* 2003;1138. <https://doi.org/10.1001/jama.1953.02940340098036>.
- [10] Lomax ME, Folkes LK, O'Neill P. Biological consequences of radiation-induced DNA damage: Relevance to radiotherapy. *Clin Oncol* 2013;25:578–85. <https://doi.org/10.1016/j.clon.2013.06.007>.
- [11] Joiner M, van der Kogel A. *Basic Clinical Radiobiology*. 4th ed. London: Hodder Education; 2009.
- [12] Schlegel W, Karger C, Jäkel O. *Medizinische Physik*. vol. 146. Berlin, Heidelberg: Springer Berlin Heidelberg; 2018. <https://doi.org/10.1007/978-3-662-54801-1>.
- [13] Emami B. Tolerance of Normal Tissue to Irradiation. *Int J Radiat Oncol Biol Phys* 1991;21:109–22.

Bibliography

- [14] Olsson CE, Jackson A, Deasy JO, Thor M. A Systematic Post-QUANTEC Review of Tolerance Doses for Late Toxicity After Prostate Cancer Radiation Therapy. *Int J Radiat Oncol Biol Phys* 2018;102:1514–32. <https://doi.org/10.1016/j.ijrobp.2018.08.015>.
- [15] Bentzen SM, Constine LS, Deasy JO, Eisbruch A, Jackson A, Marks LB, et al. Quantitative Analyses of Normal Tissue Effects in the Clinic (QUANTEC): An Introduction to the Scientific Issues. *Int J Radiat Oncol Biol Phys* 2010;76:3–9. <https://doi.org/10.1016/j.ijrobp.2009.09.040>.
- [16] Bortfeld T, Boyer AL, Schlegel W, Kahler DL, Waldron TJ. Realization and verification of three-dimensional conformal radiotherapy with modulated fields. *Int J Radiat Oncol Biol Phys* 1994;30:899–908. [https://doi.org/10.1016/0360-3016\(94\)90366-2](https://doi.org/10.1016/0360-3016(94)90366-2).
- [17] Bortfeld T. IMRT: A review and preview. *Phys Med Biol* 2006;51:363–79. <https://doi.org/10.1088/0031-9155/51/13/R21>.
- [18] Lomax AJ, Boehringer T, Coray A, Egger E, Goitein G, Grossmann M, et al. Intensity modulated proton therapy: A clinical example. *Med Phys* 2001;28:317–24. <https://doi.org/10.1118/1.1350587>.
- [19] Group IMRTCW. Intensity-modulated radiotherapy: current status and issues of interest. *Int J Radiat Oncol* 2001;51:880–914. [https://doi.org/10.1016/S0360-3016\(01\)01749-7](https://doi.org/10.1016/S0360-3016(01)01749-7).
- [20] ICRU Report No 50. Prescribing, recording and reporting photon beam therapy. Washington, D.C., USA: 1993.
- [21] Verellen D, Ridder M De, Linthout N, Tournel K, Soete G, Storme G. Innovations in image-guided radiotherapy. *Nat Rev Cancer* 2007;7:949–60. <https://doi.org/10.1038/nrc2288>.
- [22] Brady LW, Heilmann H-P, Molls HM. *New Technologies in Radiation Oncology*. 2006.
- [23] Kubo HD, Hill BC, Med P, Neicu T, Shirato H, Burk LM, et al. Respiration gated radiotherapy treatment : a technical study 1996;41:83.
- [24] Heerkens HD, Van Vulpen M, Van Den Berg CAT, Tijssen RHN, Crijns SPM, Molenaar IQ, et al. MRI-based tumor motion characterization and gating schemes for radiation therapy of pancreatic cancer. *Radiother Oncol* 2014;111:252–7. <https://doi.org/10.1016/j.radonc.2014.03.002>.
- [25] Kontaxis C, Bol GH, Lagendijk JJW, Raaymakers BW. A new methodology for inter- and intrafraction plan adaptation for the MR-linac. *Phys Med Biol* 2015;60:7485–97. <https://doi.org/10.1088/0031-9155/60/19/7485>.
- [26] Hounsfield GN. Computerized transverse axial scanning (tomography): Part 1. Description of system. *Br J Radiol* 1973;46:1016–22. <https://doi.org/10.1259/0007-1285-46-552-1016>.
- [27] Managing patient dose in multi-detector computed tomography (MDCT). *Int Comm Radiol Prot* 2007.
- [28] Smith-Bindman R. Radiation Dose Associated With Common Computed Tomography Examinations and the Associated Lifetime Attributable Risk of Cancer. *Arch Intern Med* 2009;169:2078. <https://doi.org/10.1001/archinternmed.2009.427>.

-
- [29] Pouliot J, Bani-Hashemi A, Josephine Chen, Svatos M, Ghelmansarai F, Mitschke M, et al. Low-dose megavoltage cone-beam CT for radiation therapy. *Int J Radiat Oncol Biol Phys* 2005;61:552–60. <https://doi.org/10.1016/j.ijrobp.2004.10.011>.
- [30] Mosleh-Shirazi MA, Evans PM, Swindell W, Webb S, Partridge M. A cone-beam megavoltage CT scanner for treatment verification in conformal radiotherapy. *Radiother Oncol* 1998;48:319–28. [https://doi.org/10.1016/S0167-8140\(98\)00042-5](https://doi.org/10.1016/S0167-8140(98)00042-5).
- [31] Jaffray DA, Siewerdsen JH, Wong JW, Martinez AA. Flat-panel cone-beam computed tomography for image-guided radiation therapy. *Int J Radiat Oncol* 2002;53:1337–49. [https://doi.org/10.1016/S0360-3016\(02\)02884-5](https://doi.org/10.1016/S0360-3016(02)02884-5).
- [32] Reiser MF, Semmler W, Hricak H. *Magnetic Resonance Tomography*. 2008. <https://doi.org/10.1007/b135693>.
- [33] Fuchs VR, Sox HC. Physicians' Views Of The Relative Importance Of Thirty Medical Innovations. *Health Aff* 2001;20:30–42. <https://doi.org/10.1377/hlthaff.20.5.30>.
- [34] Ramsey NF. Early history of Magnetic Resonance. Cambridge: *Bulletin of Magnetic Resonance*; 1985.
- [35] Brown RW, Cheng YN, Haacke EM, Thompson MR, Venkatesan R. *Magnetic Resonance Imaging: Second Edition*. 2nd ed. Hoboken, New Jersey: John Wiley & Sons; 2014.
- [36] Jordan E, Balmain K. *Electromagnetic Waves and Radiating Systems*. Englewood Cliffs, N. J.: Prentice-Hall; 1968.
- [37] Pauly J, Nishimura D, Macovski A. A k-space analysis of small-tip-angle excitation. 1989. *J Magn Reson* 2011;213:544–57. <https://doi.org/10.1016/j.jmr.2011.09.023>.
- [38] Hahn EL. Spin Echoes. *Phys Rev* 1950;80:580–94. <https://doi.org/10.1103/PhysRev.80.580>.
- [39] Carr HY, Purcell EM. Effects of diffusion on free precession in nuclear magnetic resonance experiments. *Phys Rev* 1954;94:630–8. <https://doi.org/10.1103/PhysRev.94.630>.
- [40] Meiboom S, Gill D. Modified spin-echo method for measuring nuclear relaxation times. *Rev Sci Instrum* 1958;29:688–91. <https://doi.org/10.1063/1.1716296>.
- [41] Hennig J, Nauerth A, Friedburg H. RARE imaging: A fast imaging method for clinical MR. *Magn Reson Med* 1986;3:823–33. <https://doi.org/10.1002/mrm.1910030602>.
- [42] Oppelt A, Graumann R, Barfuß H, Fischer H, Hartl W, Schajor W. FISP - a new fast MRI sequence. *Electromedica* 1986;54:15.
- [43] Scheffler K, Hennig J. Is TrueFISP a gradient-echo or a spin-echo sequence? *Magn Reson Med* 2003;49:395–7. <https://doi.org/10.1002/mrm.10351>.
- [44] Bieri O, Scheffler K. Fundamentals of balanced steady state free precession MRI. *J Magn Reson Imaging* 2013;38:2–11. <https://doi.org/10.1002/jmri.24163>.
- [45] Bostel T, Pfaffenberger A, Delorme S, Dreher C, Echner G, Haering P, et al. Prospective feasibility analysis of a novel off-line approach for MR-guided radiotherapy. *Strahlentherapie Und Onkol* 2018;194:425–34. <https://doi.org/10.1007/s00066-017-1258-y>.

Bibliography

- [46] Karlsson M, Karlsson MG, Nyholm T, Amies C, Zackrisson B. Dedicated Magnetic Resonance Imaging in the Radiotherapy Clinic. *Int J Radiat Oncol Biol Phys* 2009;74:644–51. <https://doi.org/10.1016/j.ijrobp.2009.01.065>.
- [47] Jaffray DA, Carlone MC, Milosevic MF, Breen SL, Stanescu T, Rink A, et al. A Facility for Magnetic Resonance-Guided Radiation Therapy. *Semin Radiat Oncol* 2014;24:193–5. <https://doi.org/10.1016/j.semradonc.2014.02.012>.
- [48] Fallone BG, Murray B, Rathee S, Stanescu T, Steciw S, Vidakovic S, et al. First MR images obtained during megavoltage photon irradiation from a prototype integrated linac-MR system. *Med Phys* 2009;36:2084–8. <https://doi.org/10.1118/1.3125662>.
- [49] Keall PJ, Barton M, Crozier S. The Australian Magnetic Resonance Imaging–Linac Program. *Semin Radiat Oncol* 2014;24:203–6. <https://doi.org/10.1016/j.semradonc.2014.02.015>.
- [50] Lagendijk JJW, Raaymakers BW, Raaijmakers AJE, Overweg J, Brown KJ, Kerkhof EM, et al. MRI/linac integration. *Radiother Oncol* 2008;86:25–9. <https://doi.org/10.1016/j.radonc.2007.10.034>.
- [51] Mutic S, Dempsey JF. The ViewRay System: Magnetic Resonance-Guided and Controlled Radiotherapy. *Semin Radiat Oncol* 2014;24:196–9. <https://doi.org/10.1016/j.semradonc.2014.02.008>.
- [52] Klüter S. Technical design and concept of a 0.35 T MR-Linac. *Clin Transl Radiat Oncol* 2019;18:98–101. <https://doi.org/10.1016/j.ctro.2019.04.007>.
- [53] Reiffel L, Li a, Chu J, Wheatley RW, Naqvi S, Pillsbury R, et al. Control of photon beam dose profiles by localized transverse magnetic fields. *Phys Med Biol* 2000;45:N177–82. <https://doi.org/10.1088/0031-9155/45/12/401>.
- [54] Raaymakers BW, Raaijmakers a JE, Lagendijk JJW. Integrating a MRI scanner with a 6 MV radiotherapy accelerator: dose deposition in a transverse magnetic field. *Phys Med Biol* 2004;50:1363–76. <https://doi.org/10.1088/0031-9155/50/7/002>.
- [55] Raaijmakers a JE, Raaymakers BW, Lagendijk JJW. Integrating aMRI scanner with a 6MV radiotherapy accelerator: impact of the surface orientation on the entrance and exit dose due to the transverse magnetic field. *Phys Med Biol* 2007;50:1363–76. <https://doi.org/10.1088/0031-9155/50/7/002>.
- [56] Raaijmakers a JE, Raaymakers BW, Lagendijk JJW. Experimental verification of magnetic field dose effects for the MRI-accelerator. *Phys Med Biol* 2007;52:4283–91. <https://doi.org/10.1088/0031-9155/52/14/017>.
- [57] Kirkby C, Stanescu T, Rathee S, Carlone M, Murray B, Fallone BG. Patient dosimetry for hybrid MRI-radiotherapy systems. *Med Phys* 2008;35:1019–27. <https://doi.org/10.1118/1.2839104>.
- [58] Oborn BM, Metcalfe PE, Butson MJ, Rosenfeld AB. High resolution entry and exit Monte Carlo dose calculations from a linear accelerator 6 MV beam under the influence of transverse magnetic fields. *Med Phys* 2009;36:3549–59. <https://doi.org/10.1118/1.3157203>.

-
- [59] Kirkby C, Murray B, Rathee S, Fallone BG. Lung dosimetry in a linac-MRI radiotherapy unit with a longitudinal magnetic field. *Med Phys* 2010;37:4722–32. <https://doi.org/10.1118/1.3475942>.
- [60] Oborn BM, Metcalfe PE, Butson MJ, Rosenfeld AB, Keall PJ. Electron contamination modeling and skin dose in 6 MV longitudinal field MRIgRT: Impact of the MRI and MRI fringe field. *Med Phys* 2012;39:874–90. <https://doi.org/10.1118/1.3676181>.
- [61] Raaijmakers a JE, Raaymakers BW, Lagendijk JJW. Integrating a MRI scanner with a 6 MV radiotherapy accelerator: dose increase at tissue-air interfaces in a lateral magnetic field due to returning electrons. *Phys Med Biol* 2005;50:1363–76. <https://doi.org/10.1088/0031-9155/50/7/002>.
- [62] Raaijmakers a JE, Raaymakers BW, Lagendijk JJW. Magnetic-field-induced dose effects in MR-guided radiotherapy systems: dependence on the magnetic field strength. *Phys Med Biol* 2008;53:909–23. <https://doi.org/10.1088/0031-9155/53/4/006>.
- [63] van der Meer S. Integrating a MRI scanner with a 6 MV radiotherapy accelerator: Impact of the surface orientation on the dose deposition at interfaces. *Phys Med Biol* 2006;52:929–39. <https://doi.org/10.1088/0031-9155/52/4/005>.
- [64] Seco J, Clasié B, Partridge M. Review on the characteristics of radiation detectors for dosimetry and imaging. *Phys Med Biol* 2014;59:R303–47. <https://doi.org/10.1088/0031-9155/59/20/R303>.
- [65] Seuntjens J, Duane S. Photon absorbed dose standards. *Metrologia* 2009;46. <https://doi.org/10.1088/0026-1394/46/2/S04>.
- [66] Seco J, Clasié B, Partridge M. Review on the characteristics of radiation detectors for dosimetry and imaging. *Phys Med Biol* 2014;59:R303–47. <https://doi.org/10.1088/0031-9155/59/20/R303>.
- [67] Reynolds M, Fallone BG, Rathee S. Dose response of selected ion chambers in applied homogeneous transverse and longitudinal magnetic fields. *Med Phys* 2013;40:042102. <https://doi.org/10.1118/1.4794496>.
- [68] Meijsing I, Raaymakers BW, Raaijmakers a JE, Kok JGM, Hogeweg L, Liu B, et al. Dosimetry for the MRI accelerator: the impact of a magnetic field on the response of a Farmer NE2571 ionization chamber. *Phys Med Biol* 2009;54:2993–3002. <https://doi.org/10.1088/0031-9155/54/10/002>.
- [69] Smit K, van Asselen B, Kok JGM, Aalbers a HL, Lagendijk JJW, Raaymakers BW. Towards reference dosimetry for the MR-linac: magnetic field correction of the ionization chamber reading. *Phys Med Biol* 2013;58:5945–57. <https://doi.org/10.1088/0031-9155/58/17/5945>.
- [70] Spindeldreier CK, Schrenk O, Bakenecker K, Kawrakow I, Burigo L, Karger CP, et al. Radiation dosimetry in magnetic fields with Farmer-type ionization chambers: Determination of magnetic field correction factors for different magnetic field strengths and field orientations. *Phys Med Biol* 2017;417:257–69. <https://doi.org/10.1042/BJ20081146>.

Bibliography

- [71] EURAMET. Traceable dosimetry for small fields in MR-guided radiotherapy. EMPIR Call 2019 – Energy, Environ Norm Res Potential Sel Res Top Number SRT-N13 2019:2–3. https://msu.euramet.org/current_calls/pre_norm_2019/documents/SRT-n13.pdf (accessed November 25, 2019).
- [72] Butson MJ, Yu PKN, Cheung T, Metcalfe P. Radiochromic film for medical radiation dosimetry. *Mater Sci Eng R Reports* 2003;41:61–120. [https://doi.org/10.1016/S0927-796X\(03\)00034-2](https://doi.org/10.1016/S0927-796X(03)00034-2).
- [73] Reinhardt S, Hillbrand M, Wilkens JJ, Assmann W. Comparison of Gafchromic EBT2 and EBT3 films for clinical photon and proton beams. *Med Phys* 2012;39:5257–62. <https://doi.org/10.1118/1.4737890>.
- [74] León Marroquin EY, Herrera González JA, Camacho López MA, Villarreal Barajas JE, García-Garduño OA. Evaluation of the uncertainty in an EBT3 film dosimetry system utilizing net optical density. *J Appl Clin Med Phys* 2016;17:466–81. <https://doi.org/10.1120/jacmp.v17i5.6262>.
- [75] Reynoso F, Curcuru A, Green O, Mutic S, Das I, Santanam L. Technical Note: Magnetic field effects on Gafchromic-film response in MR-IGRT. *Med Phys* 2016;43:6552–6. <https://doi.org/10.1118/1.4958149>.
- [76] Adamovics J, Maryanski MJ. Characterisation of PRESAGE™: A new 3-D radiochromic solid polymer dosimeter for ionising radiation. *Radiat Prot Dosimetry* 2006;120:107–12. <https://doi.org/10.1093/rpd/nci555>.
- [77] Brown S, Venning A, De Deene Y, Vial P, Oliver L, Adamovics J, et al. Radiological properties of the PRESAGE and PAGAT polymer dosimeters. *Appl Radiat Isot* 2008;66:1970–4. <https://doi.org/10.1016/j.apradiso.2008.06.005>.
- [78] Thomas A, Niebanck M, Juang T, Wang Z, Oldham M. A comprehensive investigation of the accuracy and reproducibility of a multitarget single isocenter VMAT radiosurgery technique. *Med Phys* 2013;40. <https://doi.org/10.1118/1.4829518>.
- [79] Oldham M, Siewerdsen JH, Shetty A, Jaffray DA. High resolution gel-dosimetry by optical-CT and MR scanning. *Med Phys* 2001;28:1436–45. <https://doi.org/10.1118/1.1380430>.
- [80] Baldock C, De Deene Y, Doran S, Ibbott G, Jirasek A, Lepage M, et al. Polymer gel dosimetry. *Phys Med Biol* 2010;55:R1–63. <https://doi.org/10.1088/0031-9155/55/5/R01>.
- [81] De Deene Y, Jirasek A. Uncertainty in 3D gel dosimetry. *J Phys Conf Ser* 2015;573:12008. <https://doi.org/10.1088/1742-6596/573/1/012008>.
- [82] De Deene Y, Hurley C, Venning A, Vergote K, Mather M, Healy BJ, et al. A basic study of some normoxic polymer gel dosimeters. *Phys Med Biol* 2002;47:3441–63. <https://doi.org/10.1088/0031-9155/47/19/301>.
- [83] Vandecasteele J, De Deene Y. On the validity of 3D polymer gel dosimetry: I. reproducibility study. *Phys Med Biol* 2013;58:19–42. <https://doi.org/10.1088/0031-9155/58/1/19>.

-
- [84] Vandecasteele J, De Deene Y. On the validity of 3D polymer gel dosimetry: II. Physico-chemical effects. *Phys Med Biol* 2013;58:19–42. <https://doi.org/10.1088/0031-9155/58/1/19>.
- [85] Vandecasteele J, De Deene Y. On the validity of 3D polymer gel dosimetry: III. MRI-related error sources. *Phys Med Biol* 2013;58:19–42. <https://doi.org/10.1088/0031-9155/58/1/19>.
- [86] Schreiner LJ. True 3D chemical dosimetry (gels, plastics): Development and clinical role. *J Phys Conf Ser* 2015;573:012003. <https://doi.org/10.1088/1742-6596/573/1/012003>.
- [87] Hilts M, Audet C, Duzenli C, Jirasek A. Polymer gel dosimetry using x-ray computed tomography: a feasibility study 4. *Phys Med Biol* 2000;45:2559–71. <https://doi.org/10.1088/0031-9155/45/9/309>.
- [88] Jirasek A, Hilts M, Shaw C, Baxter P. Investigation of tetrakis hydroxymethyl phosphonium chloride as an antioxidant for use in x-ray computed tomography polyacrylamide gel dosimetry. *Phys Med Biol* 2006;51:1891–906. <https://doi.org/10.1088/0031-9155/51/7/018>.
- [89] Venning a J, Hill B, Brindha S, Healy BJ, Baldock C. Investigation of the PAGAT polymer gel dosimeter using magnetic resonance imaging. *Phys Med Biol* 2005;50:3875–88. <https://doi.org/10.1088/0031-9155/50/16/015>.
- [90] Mann P, Witte M, Moser T, Lang C, Runz A, Johnen W, et al. 3D dosimetric validation of motion compensation concepts in radiotherapy using an anthropomorphic dynamic lung phantom. *Phys Med Biol* 2017;62:573–95. <https://doi.org/10.1088/1361-6560/aa51b1>.
- [91] De Deene Y, Vergote K, Claeys C, De Wagter C. The fundamental radiation properties of normoxic polymer gel dosimeters: a comparison between a methacrylic acid based gel and acrylamide based gels. *Phys Med Biol* 2006;51:653–73. <https://doi.org/10.1088/0031-9155/51/3/012>.
- [92] Roed Y, Ding Y, Wen Z, Wang J, Pinsky L, Ibbott G. The potential of polymer gel dosimeters for 3D MR-IGRT quality assurance. *J Phys Conf Ser* 2017;847:012059. <https://doi.org/10.1088/1742-6596/847/1/012059>.
- [93] National Electrical Manufacturers Association. NEMA Standards Publication MS 1-2001: Determination of Signal-to-Noise Ratio (SNR) in Diagnostic Magnetic Resonance Imaging. 2001.
- [94] American College Of Radiology. Phantom Test Guidance for the ACR MRI Accreditation Program. 2005.
- [95] Treuer H, Hoevels M, Luyken K, Gierich a, Kocher M, Muller R-P, et al. On isocentre adjustment and quality control in linear accelerator based radiosurgery with circular collimators and room lasers. *Phys Med Biol* 2000;45:2331–42. <https://doi.org/10.1088/0031-9155/45/8/318>.
- [96] International Electrotechnical Commission. IEC 61217: Radiotherapy equipment – Coordinates, movements and scales. 2011.

Bibliography

- [97] Lutz W, Winston KR, Maleki N. A system for stereotactic radiosurgery with a linear accelerator. *Int J Radiat Oncol Biol Phys* 1988;14:373–81. [https://doi.org/10.1016/0360-3016\(88\)90446-4](https://doi.org/10.1016/0360-3016(88)90446-4).
- [98] Depuydt T, Penne R, Verellen D, Hrbacek J, Lang S, Leysen K, et al. Computer-aided analysis of star shot films for high-accuracy radiation therapy treatment units. *Phys Med Biol* 2012;57:2997–3011. <https://doi.org/10.1088/0031-9155/57/10/2997>.
- [99] van Zijp HM, van Asselen B, Wolthaus JWH, Kok JMG, de Vries JHW, Ishakoglu K, et al. Minimizing the magnetic field effect in MR-linac specific QA-tests: the use of electron dense materials. *Phys Med Biol* 2016;61:N50–9. <https://doi.org/10.1088/0031-9155/61/3/N50>.
- [100] Mackie TR, Holmes T, Swerdloff S, Reckwerdt P, Deasy JO, Yang J, et al. Tomotherapy: A new concept for the delivery of dynamic conformal radiotherapy. *Med Phys* 1993;20:1709–19. <https://doi.org/10.1118/1.596958>.
- [101] Fenwick JD, Tomé WA, Jaradat HA, Hui SK, James JA, Balog JP, et al. Quality assurance of a helical tomotherapy machine. *Phys Med Biol* 2004;49:2933–53. <https://doi.org/10.1088/0031-9155/49/13/012>.
- [102] ViewRay. Operator’s Manual for the MRIdian System 4.5 2016. https://viewray.com/wp-content/uploads/2018/06/L_0009_OpMan4_5.pdf (accessed November 25, 2019).
- [103] De Neve W, Van den Heuvel F, De Beukeleer M, Coghe M, Thon L, De Roover P, et al. Routine clinical on-line portal imaging followed by immediate field adjustment using a tele-controlled patient couch. *Radiother Oncol* 1992;24:45–54. [https://doi.org/10.1016/0167-8140\(92\)90353-V](https://doi.org/10.1016/0167-8140(92)90353-V).
- [104] Ezz A, Munro P, Porter AT, Battista J, Jaffray DA, Fenster A, et al. Daily monitoring and correction of radiation field placement using a video-based portal imaging system: A pilot study. *Int J Radiat Oncol Biol Phys* 1992;22:159–65. [https://doi.org/10.1016/0360-3016\(92\)90995-T](https://doi.org/10.1016/0360-3016(92)90995-T).
- [105] Hanson IM, Nill S, Chick J, Oelke U. Linac commissioning methodology for the Elekta Unity MR Linac, Milano: ESTRO38: PO-1035; 2019. <https://doi.org/10.3252/pso.eu.ESTRO38.2019>.
- [106] Wang D, Doddrell D. Geometric Distortion in Structural Magnetic Resonance Imaging. *Curr Med Imaging Rev* 2005;1:49–60. <https://doi.org/10.2174/1573405052953029>.
- [107] Jezzard P, Balaban RS. Correction for geometric distortion in echo planar images from B0 field variations. *Magn Reson Med* 1995;34:65–73. <https://doi.org/10.1002/mrm.1910340111>.
- [108] Moerlandt MA, Beersmat R, Bhagwandient R, Wijrdemant HK, Bakker CJG. Analysis and correction of geometric distortions in 1.5 T magnetic resonance images for use in radiotherapy treatment planning. *Phys Med Biol Phys Med Biol* 1995;40:1651–64. <https://doi.org/10.1088/0031-9155/40/10/007>.
- [109] Baldwin LN, Wachowicz K, Fallone BG. A two-step scheme for distortion rectification of magnetic resonance images. *Med Phys* 2009;36:3917–26. <https://doi.org/10.1118/1.3180107>.

- [110] Wang D, Strugnell W, Cowin G, Doddrell DM, Slaughter R. Geometric distortion in clinical MRI systems Part I: evaluation using a 3D phantom. *Magn Reson Imaging* 2004;22:1223–32. <https://doi.org/10.1016/j.mri.2004.08.014>.
- [111] Wang D, Strugnell W, Cowin G, Doddrell DM, Slaughter R. Geometric distortion in clinical MRI systems: Part II: Correction using a 3D phantom. *Magn Reson Imaging* 2004;22:1223–32. <https://doi.org/10.1016/j.mri.2004.08.014>.
- [112] Doran SJ, Charles-Edwards L, Reinsberg SA, Leach MO. A complete distortion correction for MR images: I. Gradient warp correction. *Phys Med Biol* 2005;50:1343–61. <https://doi.org/10.1088/0031-9155/50/7/001>.
- [113] Reinsberg SA, Doran SJ, Charles-Edwards EM, Leach MO. A complete distortion correction for MR images: II. Rectification of static-field inhomogeneities by similarity-based profile mapping. *Phys Med Biol* 2005;50:2651–61. <https://doi.org/10.1088/0031-9155/50/11/014>.
- [114] Yan Y, Yang J, Beddar S, Ibbott G, Wen Z, Court LE, et al. A methodology to investigate the impact of image distortions on the radiation dose when using magnetic resonance images for planning. *Phys Med Biol* 2018;63. <https://doi.org/10.1088/1361-6560/aab5c3>.
- [115] Ginn JS, Agazaryan N, Cao M, Baharom U, Low DA, Yang Y, et al. Characterization of spatial distortion in a 0.35 T MRI-guided radiotherapy system. *Phys Med Biol* 2017;62:4525–40. <https://doi.org/10.1088/1361-6560/aa6e1a>.
- [116] Green OL, Rankine LJ, Cai B, Curcuru A, Kashani R, Rodriguez V, et al. First clinical implementation of real-time, real anatomy tracking and radiation beam control. *Med Phys* 2018;45:3728–40. <https://doi.org/10.1002/mp.13002>.
- [117] Zakjevskii V V., Knill CS, Rakowski JT, Snyder MG. Development and evaluation of an end-to-end test for head and neck IMRT with a novel multiple-dosimetric modality phantom. *J Appl Clin Med Phys* 2016;17:497–510. <https://doi.org/10.1120/jacmp.v17i2.5705>.
- [118] Sarkar V, Huang L, Huang Y, Szegedi M, Rassiah-Szegedi P, Zhao H, et al. SU-E-T-38: A Head to Head Comparison of Two Commercial Phantoms Used for SRS QA. *Med Phys* 2015;42:3339–3339. <https://doi.org/10.1118/1.4924399>.
- [119] Costa F, Menten MJ, Doran S, Adamovics J, Hanson IM, Nill S, et al. Dose verification of dynamic MLC-tracked radiotherapy using small PRESAGE® 3D dosimeters and a motion phantom. *J Phys Conf Ser* 2019;1305:012068. <https://doi.org/10.1088/1742-6596/1305/1/012068>.
- [120] Glitzner M, Woodhead PL, Borman PTS, Lagendijk JJW, Raaymakers BW. Technical note: MLC-tracking performance on the Elekta unity MRI-linac. *Phys Med Biol* 2019;64:15NT02. <https://doi.org/10.1088/1361-6560/ab2667>.
- [121] ModusQA. MRI-safe 4D Adaptive MRgRT QA 2019:2. https://modusqa.com/images/resources/MMDI_QUASAR_MRI4D_PDS.pdf (accessed November 10, 2019).

Bibliography

- [122] Klein EE, Hanley J, Bayouth J, Yin F-F, Simon W, Dresser S, et al. Task Group 142 report: Quality assurance of medical accelerators. *Med Phys* 2009;36:4197–212. <https://doi.org/10.1118/1.3190392>.
- [123] Breeuwer MM, Holden M, Zylka W. Detection and correction of geometric distortion in 3D MR images. *Med Imaging* 2001 2001;4322:1110–20. <https://doi.org/10.1117/12.430986>.
- [124] Latifi K, Moros EG, Zhang G, Harrison L, Feygelman V. A Method to Determine the Coincidence of MRI-Guided Linac Radiation and Magnetic Isocenters. *Technol Cancer Res Treat* 2019;18:153303381987798. <https://doi.org/10.1177/1533033819877986>.
- [125] Reeder SB, Herzka DA, McVeigh ER. Signal-to-noise ratio behavior of steady-state free precession. *Magn Reson Med* 2004;52:123–30. <https://doi.org/10.1002/mrm.20126>.
- [126] ViewRay. FDA 510 (k) Clearance for Advancements in MRI and Functional Imaging Technologies for MRIdian MRI-Guided Radiation Therapy System 2019;510. <https://investors.viewray.com/news-releases/news-release-details/viewray-announces-fda-510k-clearance-advancements-mri-and> (accessed November 25, 2019).
- [127] Adamson J, Carroll J, Trager M, Yoon SW, Kodra J, Maynard E, et al. Delivered Dose Distribution Visualized Directly With Onboard kV-CBCT: Proof of Principle. *Int J Radiat Oncol* 2019;103:1271–9. <https://doi.org/10.1016/j.ijrobp.2018.12.023>.
- [128] Vergote K, De Deene Y, Duthoy W, De Gerssem W, De Neve W, Achten E, et al. Validation and application of polymer gel dosimetry for the dose verification of an intensity-modulated arc therapy (IMAT) treatment. *Phys Med Biol* 2004;49:287–305.
- [129] Kamomae T, Shimizu H, Nakaya T, Okudaira K, Aoyama T, Oguchi H, et al. Three-dimensional printer-generated patient-specific phantom for artificial in vivo dosimetry in radiotherapy quality assurance. *Phys Med* 2017;44:205–11. <https://doi.org/10.1016/j.ejmp.2017.10.005>.
- [130] Oh D, Hong C-S, Ju SG, Kim M, Koo BY, Choi S, et al. Development of patient-specific phantoms for verification of stereotactic body radiation therapy planning in patients with metallic screw fixation. *Sci Rep* 2017;7:40922.
- [131] Yea JW, Park JW, Kim SK, Kim DY, Kim JG, Seo CY, et al. Feasibility of a 3D-printed anthropomorphic patient-specific head phantom for patient-specific quality assurance of intensity-modulated radiotherapy. *PLoS One* 2017;12. <https://doi.org/10.1371/journal.pone.0181560>.
- [132] Stratasys. VeroClear–Rigid Transparent PolyJet Material (Eden Prairie, MN: Stratasys) 2008. http://www.stratasys.com/-/media/files/material-spec-sheets/mss_pj_veroclear_0318a.pdf (accessed November 25, 2019).
- [133] Elter A, Dorsch S, Mann P, Runz A, Johnen W, Spindeldreier CK, et al. End-to-end test of an online adaptive treatment procedure in MR-guided radiotherapy using a phantom with anthropomorphic structures. *Phys Med Biol* 2019;64:225003. <https://doi.org/10.1088/1361-6560/ab4d8e>.

- [134] Mann P. Developement and implemenation of 3D-dosimetric end-to-end tests in adaptive radiation therapy of moving tumors. PhD-Thesis, 2017.

List of publications

Journal articles

- Dorsch S**, Mann P, Lang C, Haering P, Runz A and Karger C P 2018 Feasibility of polymer gel-based measurements of radiation isocenter accuracy in magnetic fields *Phys. Med. Biol.* **63** 11NT02
- Elter A, **Dorsch S**, Mann P, Runz A, Johnen W, Karger C P 2019 Compatibility of 3D printing materials and printing techniques with PAGAT gel dosimetry *Phys. Med. Biol.* **64** 04NT02
- Dorsch, S**, Mann, P, Elter, A, Runz, A, Spindeldreier C K, Klüter, S and Karger, C P 2019 Polymer gel-based measurements of the isocenter accuracy in an MR-LINAC *J. Phys. Conf. Ser.* **1305** 012007
- Dorsch S**, Mann P, Elter A, Runz A, Klüter S, Karger C P 2019 Measurement of isocenter alignment accuracy and image distortion of a 0.35 T MR-Linac System *Phys. Med. Biol.* **64** 205011
- Elter A, **Dorsch S**, Mann P, Runz A, Johnen W, Spindeldreier K, Klüter S and Karger C P 2019 End-to-end test of an online adaptive treatment procedure in MR-guided radiotherapy using a phantom with anthropomorphic structures *Phys. Med. Biol.* **64** 225003

Conference contributions

- Dorsch S**, Mann P, Häring P, Lang C, Runz A, Karger C P – Talk: Polymer gel-based machine QA tests for a MR-Linac-System. In: *Dreiländertagung der Medizinischen Physik, Dresden, Germany* (2017)
- Dorsch S**, Mann P, Elter A, Runz A, Klüter S, Karger C P – Talk: Polymer gel-based measurements of the isocenter accuracy in an MR-LINAC. In: *10th International Conference: 3D and Advanced Dosimetry (IC3DDose), Shanghai, China* (2018)
- Elter A, **Dorsch S**, Mann P, Häring P, Lang C, Runz A, Karger C P – Talk: 3D Polymer Gel Dosimetrie: Eignung von Druckmaterialien und Druckverfahren für den Bau neuer Phantome. In: *49. Jahrestagung der Deutschen Gesellschaft für Medizinische Physik (DGMP), Nürnberg, Germany* (2018)
- Elter A, **Dorsch S**, Mann P, Häring P, Lang C, Runz A, Karger C P – Talk: Validierung adaptiver Bestrahlungsprozeduren für die MR-geführte Strahlentherapie mittels eines neuartigen deformierbaren Phantoms. In: *50. Jahrestagung der Deutschen Gesellschaft für Medizinische Physik (DGMP), Stuttgart, Germany* (2019)
- Elter A, **Dorsch S**, Mann P, Johnen W, Runz A, Klüter S and Karger C P – Talk: Development of a deformable phantom for validation of adaptive irradiation methods in MRgRT. In: *38th annual conference of the European Society for Radiotherapy & Oncology (ESTRO), Milano, Italy* (2019)
- Elter A, **Dorsch S**, Mann P, Klüter S and Karger C P – Talk: Validation of adaptive irradiation procedures for MR-guided radiotherapy using a novel deformable phantom. *24th International Conference on Medical Physics, Santiago de Chile, Chile* (2019)
- Dorsch S**, Mann P, Häring P, Lang C, Runz A, Klüter S, Karger C P – Poster: Polymer gel-based measurements of radiation isocenter accuracy in magnetic fields. In: *6th MR in RT Symposium, Utrecht, the Netherlands* (2018)
- Dorsch S**, Mann P, Häring P, Lang C, Runz A, Karger C P – E-Poster: Feasibility study for polymer gel-based radiation isocenter accuracy test of MRgRT devices. In: *37th annual conference of the European Society for Radiotherapy & Oncology (ESTRO), Barcelona, Spain* (2018)
- Dorsch S**, Mann P, Häring P, Lang C, Runz A, Karger C P – E-Poster: Feasibility study for polymer gel-based radiation isocenter accuracy test of MRgRT devices. In: *38th annual conference of the European Society for Radiotherapy & Oncology (ESTRO), Milano, Italy* (2019)

Acknowledgments

Prof. Dr. Joao Seco and Prof. Dr. Christian Karger, I am very grateful for kindly accepting to be my first and second referee for my dissertation.

I would also like to express my special thanks to Prof. Dr. Christian Karger for the long and fruitful discussions for all the publications and the general support during the work.

Special thank also to Dr. Philipp Mann for many helpful discussions and the introduction to gel dosimetry and MRI.

I would also like to thank Prof. Dr. Christian Karger, Prof. Dr. Joao Seco and Dr. Bernhard Rhein for their guidance as members of my 'Thesis Advisory Comitee'.

I would like to thank Armin Runz for his support in the design and manufacture of all the components of all 3D-printing parts.

I am grateful to all my office, working group and department colleagues for the pleasant working atmosphere.

I would like to thank all of those who supported me during my project.

Last but not least I would like to express my deepest gratitude to my family who supported me in every phase of my life.

Explanation

I hereby assure that I composed this work by myself and did not use any other than the listed resources.

Heidelberg, 25.11.2019

.....